12-2022

Erosion and Resuspension of Cohesive Sediments in Coastal Louisiana

Laith Qasem Shamaileh
University of New Orleans, lalshama@uno.edu

Erosion and Resuspension of Cohesive Sediments in Coastal Louisiana

A Dissertation

Submitted to the Graduate Faculty
of the University of New Orleans
in partial fulfillment of the
requirements for the degree of

Doctor of Philosophy
in
Engineering and Applied Science

by

Laith Shamaileh P.E.

BSE., University of New Orleans, 2014
MSE., University of New Orleans, 2017

December, 2022

ACKNOWLEDGEMENTS

First and foremost, I would like to thank God, without whom without nothing is possible. I came to the University of New Orleans in 2010 from Amman, Jordan. I planned to earn a Bachelor's in civil engineering and then return to Jordan. However, during my time at the University of New Orleans, I developed a love for the engineering profession and the state of Louisiana and its citizens, which led me to today. My affinity with this field resulted from the privilege of interacting and receiving quality education and guidance from my teachers and advisors, Dr. Alex McCorquodale, Dr. Malay Hajara, Dr. Satish Bastola, Dr. Ioannis Georgiou, Dr. Donald Barbe, and Dr. Mark Kulp.

I also want to specially thank Dr. Alex McCorquodale, His graduate classes and advice throughout this research has developed my understanding of this topic and made this research possible. I must also thank Dr. Bastola for all important comments and guidance while writing this manuscript. Thanks also go to thank Dr. Georgiou for all the fruitful discussions and classes challenging me to grow. I want to thank Mr. George Ammari – may he rest in peace – his wife Magdalene, and their sons Zaid, Richy and Marviani. They provided me with invaluable support during my tender years in New Orleans. I also extend sincere thanks to Dr. Mattie, whose guidance was influential during my freshman year at UNO. Finally, thank you to Mr. Byron Landry for all his help during my time inside the labs.

Last but not least, to my Mother Laila, and Father Dr. Qasem, you are the reason behind any success I have today, and you will remain the reason behind any success I shall have in the future.

TABLE OF CONTENTS

LIST OF FIGURES

ABSTRACT

The research presented in this study is motivated by the need to improve the predictions of cohesive sediment erosion and subsequent transport. In addition, the knowledge of the geotechnical engineering soil properties related to the erosion of sediments in coastal Louisiana has broad implications as these properties are used in transport models guiding the current restoration efforts. The erosion measuring device used in the study is the Cheng-Han Tasi and Wilbert Lick Shaker. Previous studies have been conducted before using the Shaker, but challenges with the calibration of the shear stress hampered the resuspension results produced by the Shaker. Therefore, this study aims to examine the flow conditions inside the Shaker using the computational fluid dynamics (CFD) software Ansys. This allowed for a calibration curve based on 2-D flow conditions inside the Shaker rather than other erosion experiments. The soil sample tested using the Shaker are mainly from the southeast Louisiana coastline, which is significantly impacted by erosion. Moreover, the current study estimates the critical shear stress Pa of erosion for both mass and surface erosion, along with erosion parameters (m).

Furthermore, this study further develops a simple sediment resuspension and distribution model. This model aims to improve the efficiency of data analysis in the current Louisiana Integrated Compartment Model (ICM) sediment distribution subroutine, which uses other languages for some sediment transport simulations. Moreover, The ICM is much larger and captures a wide range of processes making it computationally demanding to answer research questions. Therefore, the new model will be simpler and only capture some processes. Furthermore, this change will allow research questions to be answered more economically than using larger integrated models.

Keywords: Geotechnical Engineering, Coastal land Loss, Coastal Restoration, Computational Fluid Dynamics, Resuspension, Coastal Louisiana, Critical Shear Stress

Chapter 1 Introduction

1.1 Coastal erosion and deposition problem

Coastal erosion of coastlines is a global phenomenon threatening almost 40% of the global population living near seas, oceans, and rivers. This has resulted in global land loss worldwide of over 10,000 square miles in the last 32 years (Mentaschi et al., 2018). Locally, where the present study is conducted, Louisiana's coastline has lost more than 18,000 square miles of wetlands since 1932 (CPRA 2017). These wetlands are the first line of defense, providing important protection against ever-increasing hurricanes and storms. Similar wetlands provide an approximately a 20% reduction in wave energy for both regular and irregular waves (Möller et al., 2014). The annual value of coastal wetlands for storm protection is approximately USD $1,700 per hectare (Costanza et al., 2008). It is important to know that if all the wetland losses recorded for Louisiana were accounted for and converted to a present value, this would yield $28 billion in lost storm protection. Moreover, hurricanes cause significant damage to coastlines. For example, Hurricane Katrina was responsible for over 1,800 fatalities and $125 billion in monetary damages. Similarly, Hurricane Sandy and Typhon Haiyan caused damages of $77 billion, and 6288 humans perished (CDC, 2013). More recently, the damage costs of Hurricane Ida in 2021 will exceed $31 billion (RMS, 2022). In summary, erosion, subsidence, and relative sea level rise negatively affect the Louisiana coastline.

Sediment deposition in waterways also pose a significant issue for navigation and require frequent dredging. Thus, dredging has become a critical part of the local and global economies as mega-ships are entering increasingly shallower waterways. For example, in Louisiana alone, the cost of maintenance dredging for waterways has risen since 1970. The US Army Corps of Engineers, funded by the federal government, has spent $105,894,803 from 2014-2019, and this was for 40,040,000 cubic yards of sediment. These dredging activities have environmental impacts such as spreading contaminants and pollutant habitat degradation and turbidity increases. In addition, rising sea levels and dam construction and leveeing of rivers have deprived adjacent land masses of much-needed land-building sediment, which enables the erosional forces to wreak havoc on these sediment-deficient wetlands.

An approach to addressing the coastal erosion problem includes creating coastal restoration plans, which are created by public and private sector partnerships. For example, the Coastal Master

Plan of Louisiana is a multi-discipline effort to "develop, implement, and enforce a comprehensive coastal protection and restoration master plan" (CPRA, 2007, p. 11). These Coastal restoration plans are updated every few years because the coastal environments they deal with are changing and responding to natural processes such as relative sea level rise. Both soft and hard engineering approaches are used to manage and combat coastal degradation. Hard infrastructure includes groins, sea walls, revetments, and offshore breakwaters. On the other hand, soft engineering solutions include beach nourishment, managed strategic retreat, and dune stabilization. The various professionals working on these issues have turned to computer models to aid the decision-making processes with regard to location selection and sustainability evaluations of these critical infrastructures. The models have become essential tools in studying coastal erosion and evaluating the impact of management/engineering practices on coastal habitat restoration. Several numerical transport models (e.g., Delft3D-FLOW; Delft3D-MOR; Delft3D-MOR; Stevens Institute, ECOMSED, 1996), are increasingly used for studying coastal zone processes. These models vary in structure, complexity, and input requirements and use multiple parameters and inputs to model sediment transport. However, it is challenging to obtain these parameters experimentally, and this is particularly true for the ones controlling the cohesive sediment transport mechanism as cohesive sediment behavior depends on physiochemical interaction and flows field interaction which adds complexity to this problem.

The coastal erosion problem can be assessed by visual observation. For instance, NASA has taken numerous satellite images highlighting areas experiencing land loss. However, determining the factors affecting erosion and finding a sustainable solution requires a comprehensive study of the coastal zone and associated processes. These approaches control wave and littoral sediment transport (Kawata., 1989). Further, Narayan et al. (2016), based on a synthesis of data from 69 field measurements in global coastal habitats, focused on the effectiveness, cost, and coastal protection benefits of natural and natural-based defenses. It was shown that projects using nature-based defenses are cost-effective and effectively reduce storm damage.

Studying cohesive sediments is more complicated than non-cohesive sediments due to interparticle forces. A clay fraction of more than 10% is sufficient for sediments to behave cohesively (Rijn, 1993). Numerical models have been a valuable tool for studying complex systems. For example, in studying cohesive sediment, calibrated numerical models have been widely used. The reliability of such a model relies on its ability to reproduce observation. However,

the fate of fine-grained sediment is only secondarily considered in the modeling effort (Roberts et al., 2015). The fate of these cohesive sediments plays a crucial role in building and sustaining marshlands. There is a need to experimentally obtain erosion parameters for numerical simulation of cohesive sediment transport and accumulation.

1.2 Problem definition

The success of structural and nonstructural approaches in controlling coastal and riverine sedimentation/erosion problems relies heavily on our knowledge of the dominant physical processes and our ability to quantify and predict erosion and sedimentation using suitable sediment transport models. Researchers and coastal restoration professionals have recently studied sediment erosion and deposition (e.g., Shu et al., 2020; Gounder Krishnappan et al., 2020; Narayan et al., 2016; Smith, 2010). The transport of most fine-grained soil is modeled in terms of a critical stress value that initiates suspension, along with characteristics parameters of sediment such as median particle size (D_{50}). However, factors affecting erosion, including clay mineralogy, organic content, sediment composition, and electrochemical interactions such as salinity, pH, and sediment stress history also control erosion. Sediment deposition mainly occurs when the sediment weight is greater than buoyant forces. However, for cohesive sediments, the depositional state is either reached by coagulation and flocculation due to electrochemical interactions or a decrease in the flow rate. Either physicochemical interactions and/or a drop in flow velocity causes sediment to fall out of suspension, creating navigational and environmental predicaments.

Sediment transport models vary from simple to more complex with many variables capturing the convoluted sediment transport processes. These models have inputs that govern sediment movements, such as critical shear stress, bed response time, and erosion and excess shear calibration constant m. Unfortunately, the prediction from such transport models is plagued with uncertainties arising from the complexity of the processes and, in some cases, the oversimplification of model assumptions for structures and values of parameters. Most of these models have parameters estimated from erosion tests using similar soils to areas being modeled. However, using the erosion test to derive parameters is not straightforward. Even in early erosion tests, the device or test method sometimes changes the strength measurements by orders of magnitude. For example, a Vermeyen (1995) test showed that erosion rates from rotating cylinder were 6-10 times higher than those estimated in the flume experiment.

1.3 Study objectives

The present study has a range of objectives, and these are to:

- Improve efficiency and uncertainties associated with the Lick Shaker having unknown flow conditions. This objective will be managed using Ansys to model flow conditions inside the Shaker.
- Experimentally investigate the sedimentation processes using the Lick Shaker. This objective will be addressed by conducting Shaker tests on sediments from southeast Louisiana.
- Extend the duration of shaker resuspension tests to mitigate the overpredicting of erosion rates during experiments. This objective will be managed by conducting longer-duration Shaker tests.
- Estimate the critical shear strength of erosion based on settling times and other geotechnical engineering index properties.
- Develop a simple model for sediment resuspension as a function of wind that will be computationally efficient to answer research questions without setting up and running spatially computationally demanding models. This objective will be addressed by further developing a numerical model using python.
- Develop a simplified model for predicting marsh accretion rates under various wind conditions.

1.4 Approach

The current organization of the thesis is summarized in Figure 1-1. The approach has four research components 1) problem identification, 2) identification of the factor's contribution, 3) methods to resolve the problems, and 4) demonstration of the application of the method using data from the Lousiana coastline. Chapter 2 contains the prevalent literature review, which reviews past erosion experiments and their associated uncertainties, It highlights numerical modeling, highlighting strengths and weaknesses. Following this, Chapter 3 deals with current study experiment equipment and procedures. Moreover, it also explains the analytical procedure for analyzing the Shaker-generated data. Chapter 4 presents the initial experimental data and analysis procedure. Chapter 5 presents the reasons behind modeling the Shaker and the 2-D modeling used to analyze the flow conditions inside the Shaker. Chapter 6 discusses the in-depth analysis of the results in highlighting surface and mass erosion parameters.

Chapter 7 deals with the numerical modeling of sediments, the language used, model theory, validation, and application of the model.Chapter 8 includes all the relevant discussions for the current experiments and numerical simulations. Finally, Chapter 9 has the conclusions of the present study, and Chapter 10 has the recommendations for future work.

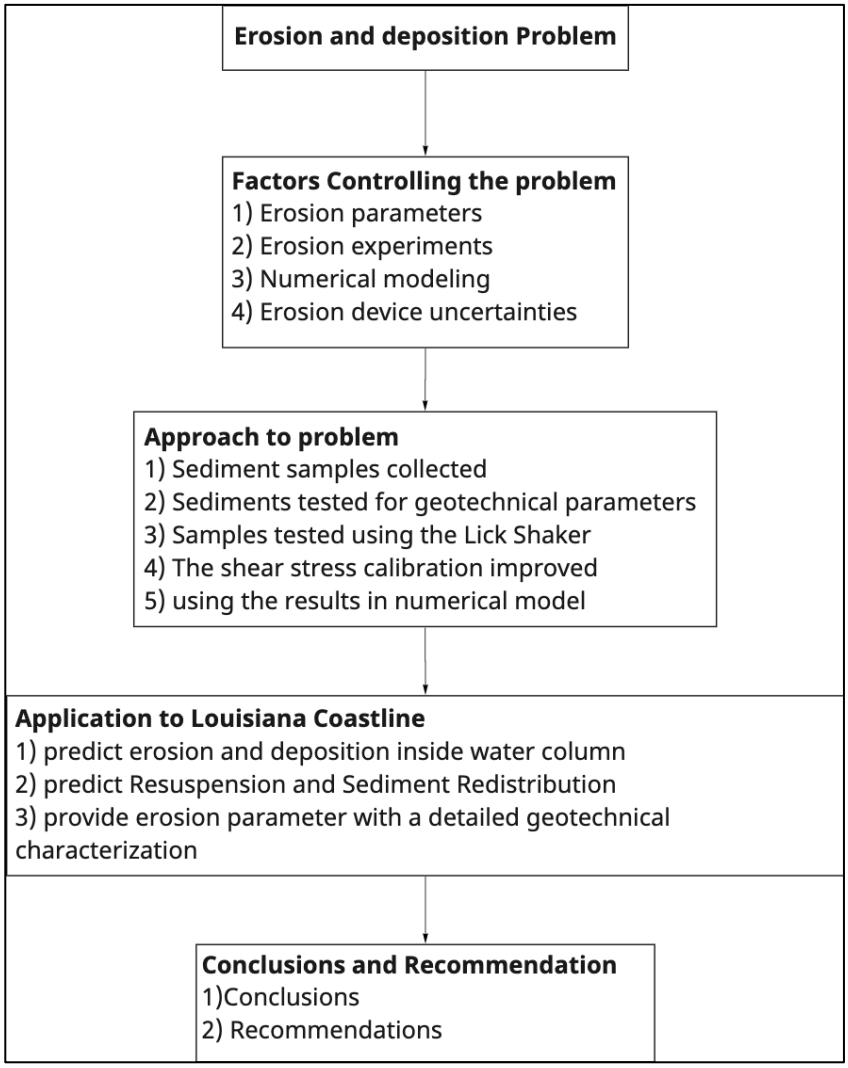

Figure 1-1 Schematic of the study methodology

Chapter 2 Literature Review

This chapter discusses cohesive sediment and associated properties, which plays an important role in cohesive sediment behavior. Laboratory experiments and numerical models are increasingly used to study the transport behavior of cohesive sediments. This chapter reviews past erosion laboratory experiments and numerical models used for studying the sediment transport process.

2.1 Physics and properties of cohesive sediments

In geotechnical engineering, the term cohesive soils refers to a combination of silts and clays. Silts and clays originate from the chemical weathering of rocks caused by oxygen and water—the cycle of erosion, deposition, and resuspension. Furthermore, a soil formation cycle is a long-term process, often unfolding over millions of years, and the final product is reached by physical disintegration and chemical decomposition. Figure 2-1 shows the different soil formation processes. Most of these formation mechanisms rely on microbial and chemical oxidation processes, which mobilize and translocate certain constituents to form different soil types.

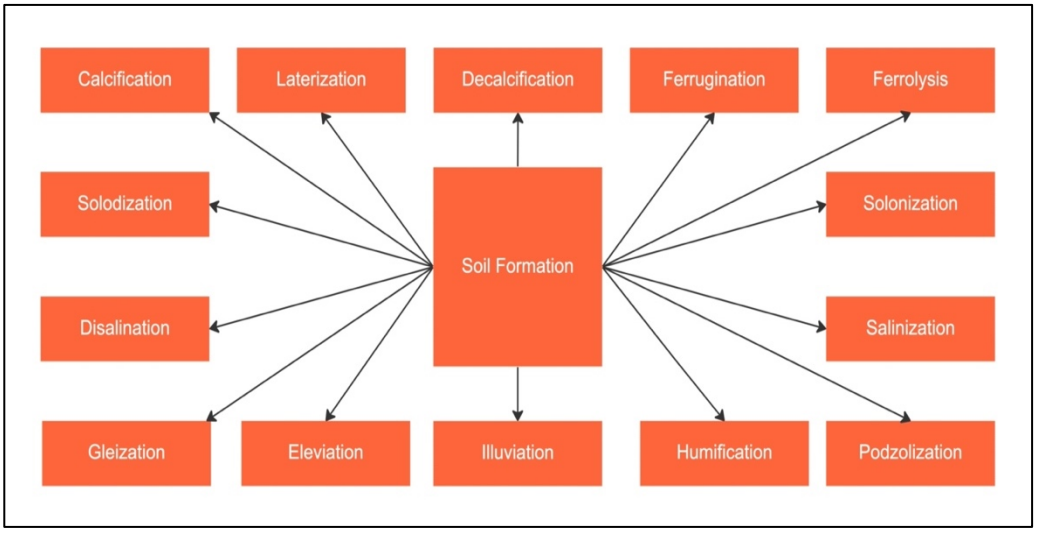

Figure 2-1 Soil Formation Processes modified from (Mitchell, 2005)

Engineers and scientists use many systems for the classification of soils such as the Unified soil classification System (USCS), the American Association of State Highway and Transportation

Officials (AASHTO), and the United States Department of Agriculture (USDA). A grain size less than 0.075mm indicates fine soil using the USCS.

The behavior of cohesive soils is mainly described by plasticity and cohesion. Plasticity, or the plasticity index, refers to the amount of water that fine soils absorb before breaking into 3mm diameter fragments. On the other hand, cohesion is the strength of clay when the deviator stress is equal to zero. The experiment conducted in this study will not directly address cohesion. However, all samples are tested for Atterberg limits which yield the plasticity index.

For the fundamental building block of clay, there is the following arrangement summarized by (Mitchell & Soga, 2005):

1. Silica tetrahedral unit – this structure has four oxygens enclosing a silicon atom that are combined in a silica sheet.
2. Aluminum, Magnesium, or Iron Octahedral unit – these structures contain six oxygens and hydroxyls enclosing an iron, magnesium, or aluminum atom.

In cohesive soils, the forces between particles are electrochemical, and clay particles have a negative charge on their surface. The electric charge can form by preferential adsorption or isomorphous substitution. Isomorphous substitution happens when a cation is replaced by a lower valence, leading to an excess negative charge. Preferential adsorption happens through chemical bonds, hydrogen bonds, and Van der Waals forces. Most of these processes occur at the outer layer of a clay particle known as a double layer. Moreover, fine sediments have a much larger surface area than cohesionless sediments this causes physiochemical force acting on them to be much larger by orders of magnitude than the submerged wights of the individual particles (Mehta, 1973).

For fine-grained sediments erosion the following points are the four modes of erosion adopted from Winterwerp et al. (2004):

- Entrainment – this occurs when the sediment behaves like a fluid and is usually caused by the eroded bed being freshly deposited (e.g., through erosion of beds formed by rapid deposition).
- Floc erosion – this occurs when parts of the bed surface (flocs) are dispersed by water movement near the bed. This phenomenon occurs when the bed shear stresses exceeds the strength of adhesion of surface particles. Note that this erosion mode is continuous, which might contribute considerably to the overall erosion process.

- Surface erosion – this occurs when the bed's top surface liquefies due to hydrodynamic pressures caused by wave action. This mode of erosion can also be called a drained failure process.
- Mass erosion or bulk erosion – this occurs when the applied external stress exceeds the strength of the bed, and large lumps of sediments are eroded. This mode is sometimes referred to as an undrained failure.

2.2 Review of past erosion laboratory experiments

One study of significance was that of Smerdon et al. (1959), who conducted experiments inside a hydraulic flume to establish a relationship between bottom shear stresses and the physical properties of the sediment such as plasticity index, median size diameter D50, percentage of clay, and the tractive shear force. The soils included silty and purely cohesive clay from Missouri, with a plasticity index range from 6-44. The authors used a Darcy pitot tube for velocity measurements and an H-type rate to measure the flow rate. However, it was noted that "mean particle size and the percent clay do not measure cohesion; therefore, the correlation may not be as high when soils with different properties exist."

Partheniades (1962) conducted a more extensive study on the erosion and deposition of cohesive soils in saltwater to design more stable channels with stable slopes in cohesive regimes. His experiments were conducted in an open flume and using ocean water salinities to test silts and clays with some sand and organics. Two beds were used inside the flume – a remolded bed and a depositional bed. The tests were used to determine the erosional and depositional behavior of fine sediments. These experiments showed that erosion is directly proportional to bed shear stresses. However, Partheniades could not find a relationship between low-strength clay erosion and strength. Therefore, he hypothesized that erosion of the bed was independent of the microscopic shear strength of the bed.

In addition, Abdel-Rahman and Naim Mohamed (1963) experimented by constructing a physical model of an open channel to examine the effects of flowing water on erosion. The first series of experiments were tested using the vane shear strength of the soil as constant through the channel and varying hydraulic conditions. The second series was completed by keeping the hydraulic condition constant and varying the shear stress of the channel. The tested soil had a plasticity index of about 22%, silicate content of 91%, and grain size between 0.002mm and

0.05mm. The author derived a relationship to determine the mean eroded depth as a function of the water's tractive stress and the soil's shear strength.

Further work includes Mehta's (1973) study in an annular rotating apparatus focused on the depositional behaviors of cohesive sediment. The depositional behavior significantly influences the net erosion rate since the numerical value of net erosion is minimal compared to the depositional rate. In the study, Mehta noted that erosion rates are directly proportional to bed shear stress after the critical value. The author also suggested that any designated critical shear stress based on observed mass erosion can differ for the same soil based on the human factor involved in determining the visual initiation of suspension. What these experiments revealed is that depending on the value of shear stress, the sediment concentration reaches a steady-state value after a short period of deposition, known as equilibrium concentration. In order to measure erosion at high shear stress at a shallow depth, McNeil et al. (1996) developed the High Shear Stress Flume. This flume was primarily designed to study sediment transport and resuspension at high-stress floods. The rectangular flume is 120 cm long, and the cross-section is 10 cm x 2 cm. Moreover, the flume has a piston jack that raises a soil sample into the flow path, measuring the sample height increase and flow velocity enables a direct erosion rate versus shear stress measurement. However, this device costs around USD 100,000 and the shear stress is calculated based on mean flow velocity and Moody Chart

Important developments included the creation of an erosion function apparatus (EFA) (Briaud, 1999; Briaud et al., 2001). This apparatus was designed for studying scouring phenomena along bridge piers; this was motivated by several bridge pier failures due to small and large shear stresses applied cyclically by turbulent flows. EFA is an open channel with a Shelby tube soil sample placed on a piston and raised incrementally. The configuration and pressure ports before and after the sample calculate the shear stress acting on the sample. Moreover, Larsen (2008) evaluated the EFA and concluded it was a very useful tool for designing bridges. However, it was noted that uncertainty in estimating the roughness require further research to find an effective method to calculate roughness. Trammell (2004) also contributed a significant development in a sediment erosion rate flume. The flume is a rectangle 9ft long with dimensions of 5 x 20 cm. The test begins by placing a sample on a piston in the middle of the flume. The sample is then raised into oncoming water flowing from two pumps down the flume. Moreover, bottom shear stresses can be calculated by simple hydraulic formulations. However, this test is no longer used because it requires a bulky

setup, and the sensors giving sample heights and water elevation are expensive and have extensive downtimes during repairs. In addition, the samples must be in a cylinder so remolded, and disturbed samples cannot be tested

2.3 Review of erosion measurements Devices

The sediment erosion and resuspension behavior under flow-induced stress can be studied using many devices and methods. In this section, I will discuss prevalent erosion measurement devices and their associated uncertainties.

The Cohesive Strength Meter (CSM) is the second generation of in situ erosion testing devices measuring the erosion shear stress of intertidal sediment. Tolhurst et al. (1999) conducted experiments using the CSM, which employs eroding stresses created by a water jet directed at the sediment interface, and the jet pressure is converted to horizontal shear stress using Shield's criterion. The coefficient of determination (R2) value for the calibration curve was below 0.5, with all the approximations involved in obtaining Shield's criterion using the settling velocity, which is approximated using Baba and Komar's (1981) relationship. The relationship, therefore, seems more empirical than mechanistic in describing erosional processes. However, this device could provide a reliable comparison with other erosion experiments (Briaud et al., 2019)

The Sediment Erosion at Depth (SED) flume was designed by McNeil et al. (1996). The purpose of this flume was to determine the critical shear stress of erosion as a function of sediment depth. The main question the authors were attempting to answer was whether containments can be exposed and eroded during large floods on rivers or large storms near lakes. The main components of the flume include a coring tube, a test section, a water storage tank, and a pump. The SED flume is similar to a rectangle or circular flume with an open bottom. This opening enables an ex-situ soil sample to be inserted into the path of flowing water. Next, an operator raises the sample at a pre-determined rate. This enables erosion of the sample at different depths.

The annular flume was developed by Fukuda and Lick (1980) and has a two-meter diameter and a 15 cm ring-shaped structure. Water fills the flume to a depth of 7.6 cm, and a rotating lid induces a shear stress on the sediment bed. The velocity profile is measured in the flume, which enables shear stress to be estimated. In the original design, the authors used a hot film anemometry to take velocity measurements in the flume. However, the flume contained no sediments, while velocity measurements were taken.

Another significant flume development is that of the Raven flume (Raven & Gschwend, 1999). The flume's main objective is to obtain in situ measurements of sediment erodibility. The flume has a 1.0 m long inlet section and a 1.2 m long sediment test section. The authors' critical shear stresses measurements were around 0.10 ± 0.04 pa, and the sediments tested had an average organic content of 3.8% and an average D_{50} of 38 μm.

In the context of the present study, the shaker used was developed by Tasi and Lick (1986). Its primary purpose was to create a portable device to measure resuspension. It contains a horizontal grid oscillating vertically, creating turbulence that causes resuspension. The shaker showed quantitative differences in entrainment behaviors at different sites (Tasi & Lick, 1986). A significant advantage pointed out by the authors was the ability of the shaker to test undisturbed samples. This is almost impossible in laboratory flumes because of the difficulty in obtaining and transporting large quantities of undisturbed samples. Finally, Haralampides (2000) used the Lick shaker to run two resuspension experiments. The shaker used was first replicated by the USGS and brought to the University of New Orleans. These experiments reached 300 revolutions per minute (RPM) or an estimated 0.16 Nm^2 equivalent shear stress. The calibration curve was given to the author by the USGS oceanographer Dr. Richard P. Signell (A. McCorquodale, personal communication, 2021). Jerolleman (2014) used the same shaker to run more resuspension experiments, which were used to obtain a critical shear stress relationship and consolidation time formulated in Hajra and McCorquodale et al. (2014). However, Jerolleman (2014) did not reach higher RPM settings with an average applied shear stress of 0.04 pa and maximum settling time of 2 days

2.4 Erosion Devices Associated uncertainties

The SED flume has the following uncertainties and drawbacks associated with its erosion-measuring framework:

- The channel is initially empty upon start-up, and no shear stress measurements are possible until the flume has been filled. During this filling stage, it is highly likely that the surface erosion critical shear stresses cannot be measured.
- Jepsen (2006) stated that measurements of unconsolidated surface erosion during this infilling stage need improvement. Moreover, The SED flume can only be used on remolded disturbed samples.

- The SED flume is an open system, and a new water source is continuously introduced during a test. This open system does not duplicate a natural system where resuspended material settles simultaneously with resuspension.
- The operator raises the sample into the flume continuously during the test, which could introduce human parallax error.
- The lab setup is very bulky and costs more than $100,000 (Briaud et al., 2019)
- There is difficulty in determining sediment roughness used in shear stress estimations.

The Annular flume has the following uncertainties and drawbacks:

- The shear stress is determined by boundary layer velocity measurements only.
- The annular flume can only test disturbed samples.
- Secondary flow velocities in the flume are generally not small compared with cohesive sediment fall velocities (Booij, 1994).

Then Raven flume also has some following uncertainties and drawbacks as follows:

- The shear stress is determined using internal flow theory. Not direct shear stress measurements or modeling.
- There is a limit to depth erosion measurements due to the internal flow theory becoming invalid and the bottom stress in the flume becoming uncertain (Jaspsen, 2005).
- It is difficult to determine sediment roughness used in shear stress estimations.
- This is an open system, and a new water source is continuously introduced during a test. This open system does not duplicate a natural system where resuspended material could settle simultaneously with resuspension (Jaspsen, 2005).

The Tasi and Lick Shaker has the following uncertainties:

- The shaker calibration curve is heavily dependent on flume conditions, and requires additional investigation (Abdelrhman et al., 1996).
- The sediment concentration in the overlying water does not necessarily replicate a condition in which an increase in water could cause additional sediments to be resuspended.
- The shaker cannot be used to determine the entrainment rate as a function of depth.

- The turbulence field generated by the Shaker differs from that generated by the shear flow (Tasi & Lick, 1986).

2.5 Review of sediment transport numerical modeling

Numerical modeling of sediment transport solves the governing equation to describe the spatial and temporal evolution of a sedimentation and or erosion process. Thus, it can be said that numerical modeling is an effective tool for predicting sediment transport processes. Scores of numerical models have been developed in the Scores of numerical models have been developed in the past (AGNPS, 1987; IQQM, 1995; GUEST, 1997; LISEM, 1999; WEPP, 2001; Delft3d, 2007; ENCOMED, 1996), and these models differ in how varying processes are accounted for. However, it must be acknowledged that there are two main issues with the numerical simulation methods in studying sediment transport. First, the underlying physics must be described in enough detail to capture the main features of the flow. If a complete flow description is possible, the solution for the system of equations would be so complex that it could not be solved in a reasonable execution time. Moreover, a complete description is impossible because terms such as turbulent shear and bed stresses are not sufficiently well understood and are usually modeled empirically (Mingham, 2003).

The second problem with numerical simulation relates to the mathematics underlying numerical models not always respecting the governing physics. The solvers sometimes fail to conserve mass or momentum, which leads to solution errors. Mingham (2003) noted that models with high levels of numerical diffusion obscure some flow features, which hinders the simulation's accuracy of the simulation. Some solvers fail on problems involving transcritical flow and abrupt changes in bathymetry (Yang et al., 2006).

Models reflective of different dimensions are utilized in this process. For instance, one-Dimensional (1D) models are used to solve cross-sectionally averaged flow equations and mass balance of suspended sediments without solving the cross-section details. These models are more effective at capturing sediment transport in long river reaches where lateral variations are negligible. Using such models improves solution stability and computational efficiency, and only a small number of in situ measurements are needed for simplified calibration and verification (Yang, 2006). However, these models do not have the capacity to capture three-dimensional phenomena such as turbulence

Two-dimensional models (2D) are better suited than 1D to modeling systems with a larger fetch. These models can be either two-dimensional horizontally averaged (2DH) or two-dimensional vertically averaged (2DV). These numerical simulations use the depth-averaged Navier-Stokes equations and sediment mass balance coupled with finite element, finite difference, or finite volume. These 2D models require detailed in situ sampling and extensive calibration. However, they can capture many more processes, such as the Coriolis effect, frictional interactions, and the transverse components of the flow.

Three-dimensional models (3D) is also used to model transport and can, for example, model turbulence more realistically. Flow near bridge piers for scour studies and flow near hydraulic structures are all examples of when a 3D model that respects the underlying physics is required. Most 3D models solve the Reynolds average Navier-Stokes (RANS) and the continuity equations, along with finite difference, finite volume, and finite element methods. However, Van Rijn (1993) noted that if the vertical grids are not defined accurately, and realistic initial boundary conditions are not met, the 3D model becomes the most sensitive and least accurate out of the other two models.

Chapter 3 Experimental Equipment and Procedure

3.1 Soil samples locations

The current study area is focused on southeast Louisiana (Figure 3-2) shows soil samples tested in this study. This area was formed by natural cycles of depositing by the Mississippi river into the Gulf of Mexico (GOM). Glacial deposits began during the Late Cretaceous period (Blum & Roberts, 2012). Since then, the Mississippi River changed course in response to sea-level rise, creating barrier islands, bays, and other geomorphic features that can be seen today. More recently, channelization and straightening of the lower Mississippi River began in the 1930s in response to catastrophic flooding events, e.g., the Great Flood of 1927. However, the levees and flood control structures that protect the human population from flooding also reduce the much-needed sediment supply wetlands need.

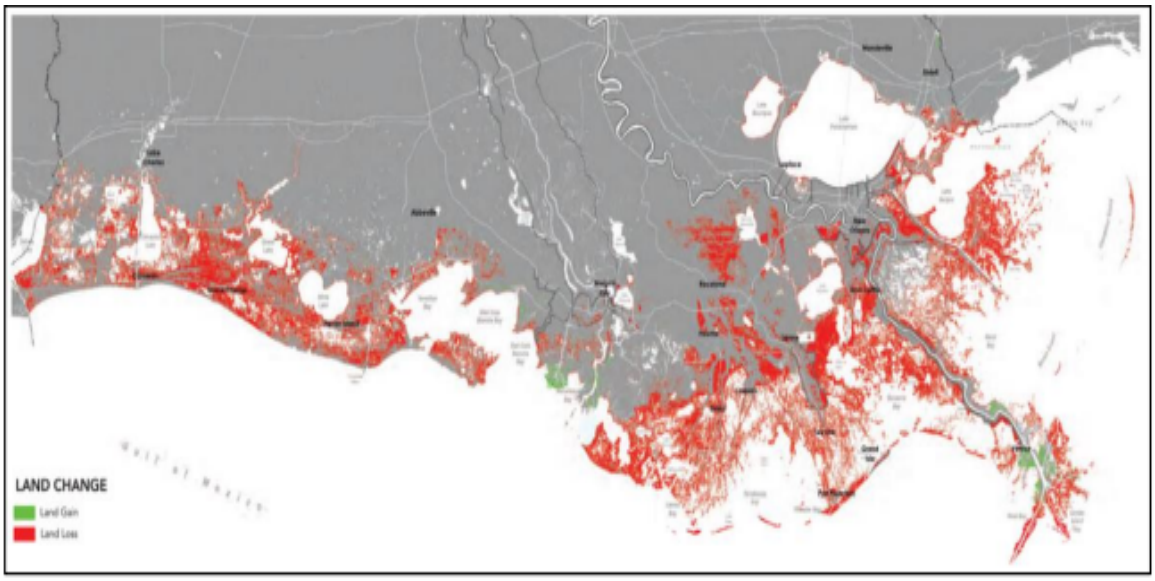

Figure 3-1 Shows one potential land change scenario over the next 50 years. The red color is land loss the green color is land gain (CPRA, 2012).

The reduction in sediment supply is primarily responsible for land loss which started accelerating around the 1930s. As the population increased in the lower Mississippi river basin, it became necessary to engage in fortification of the cities with dams and levees started to protect humans from spring flooding. These flow restrictions deprive the wetlands of their sediment load. Currently global sea-level rise and relative sea-level rise affecting the subsiding fluvial sediments is leading the coastline into decline. Since the 1930s, estimates suggest that 2,000 square miles of

wetlands have been lost (CPRA, 2012). In the last 20 years, coastal Louisiana has seen an increase in land loss at the rate of approximately 32 square miles per year as estimated by the USGS (2016). This problem will continue degrading the coastline if no action is taken to combat this land loss problem (CPRA, 2012). Figure 3-1 indicates one potential land change scenario over the next 50 years, suggesting that the areas marked in red could be lost to open water. Moreover, Louisiana's barrier islands are eroding and or receding at a rate of up to 20 meters per year (Williams, 1995).

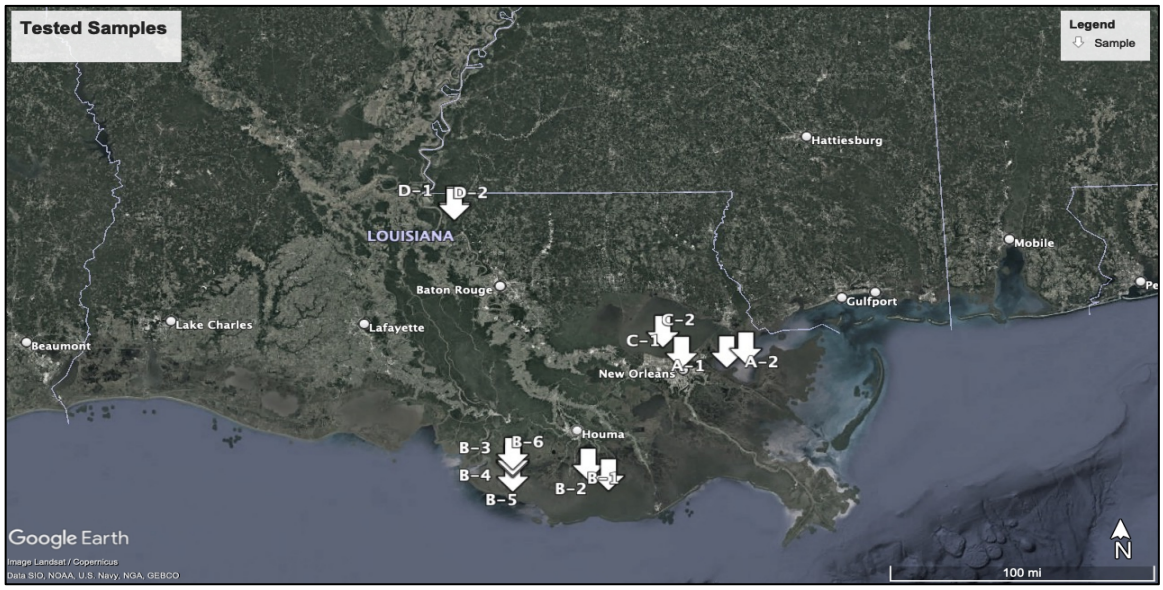

Figure 3-2 The white arrows show the geographical location of soil samples tested in the current study

According to recent USGS estimates, several barrier islands will disappear by the end of the century. Natural processes alone are not responsible for the degradation and loss of wetlands in the Mississippi river delta plain. The seasonal flooding that previously provided sediments critical to the growth of wetlands has been eliminated by the construction of levees and other flood control structures that channel the river and prevent sediment supply from reaching the wetlands. This sediment is now carried by the river and often discharged into deep water off the coastline (Williams, 1995). In addition, throughout the wetlands, an extensive system of dredged canals and gas pipeline networks and their accessory structures constructed to facilitate hydrocarbon exploration and production has also contributed to the problem. In relation to this, Baumann and Turner (1990) quantified the impact of hydrocarbon exploration at 25.6% of the total wetland loss. Finally, some commercial and recreational boat traffic creates wakes that erode the banks of these wetlands. These impacts enable saltwater from the Gulf of Mexico to intrude into brackish and

freshwater, leading to additional sediment deposition. Moreover, saltwater intrusion will negatively impact the fauna and flora of the region as they are unaccustomed to these higher salinities. Most sampling is conducted in southeast Louisiana, which is responsible for 80% of the total historic land loss (CWPPRA, 2012)

3.2 Field sampling

Soil samples are taken by petite Ponar Grab Sampler, a plastic tube similar to Shelby tubes with a 76.2mm soil core, and shovel grab samples (see Figure 3-3). The Ponar sample was suitable for a maximum of 10ft water depth. A rope is attached to the top of the sampler, and once the sampler hits the bed, it automatically closes and grabs around three pounds of sediments. The sediment was then stored in a labeled plastic bucket, site water was collected, and GPS location was recorded. Site water collection and GPS location marking was completed for all samples. These samples were then brought to the University of New Orleans Geotechnical Engineering Laboratory for testing.

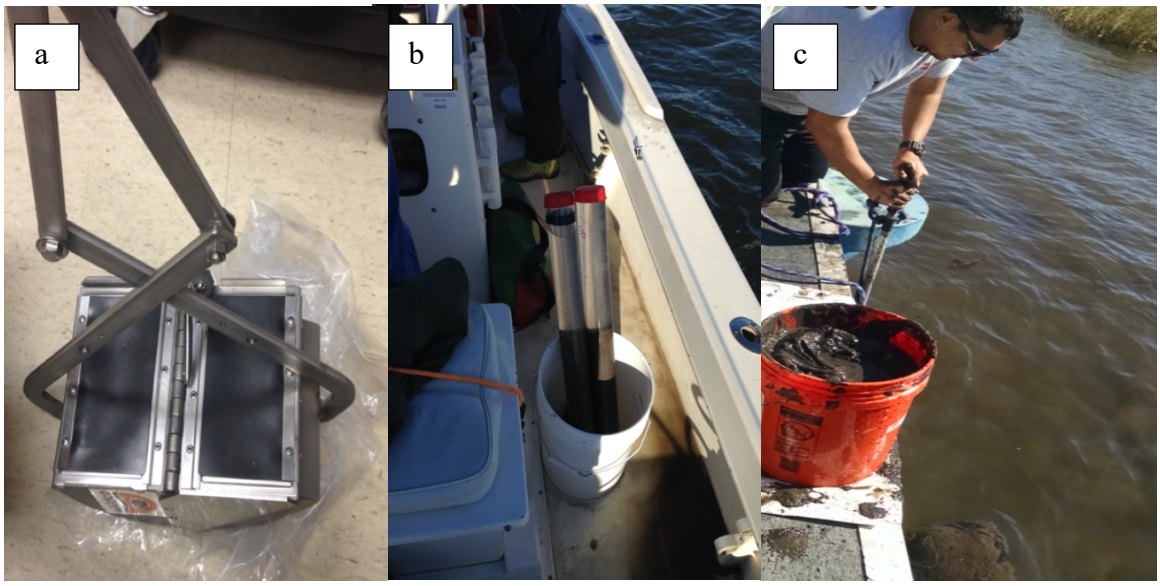

Figure 3-3 a) Ponar Grab Sampler, b) Plastic Shelby Tubes, and c) Shovel sampling

For The plastic tubes samples, the tubes are pushed by hand into the bed material where the depth is shallow enough to push these tubes approximately 2ft into the bed. For the shovel samples collection shown in Figure 3-2(c), this was also performed in areas where the water depth did not exceed five feet. For sample labeling, labels such as A-1 or D-2 are used if a sample shares the

first letter. This letter refers to samples near each other. Note these samples were collected with the help of several current and former graduate students at the University of New Orleans ((Mattson, 2014) Mebust, (2015); Roberts, (2022)).

3.3 Sample storage and sample preparations

The samples are stored in sealed plastic buckets in the geotechnical laboratory, where the temperature is controlled at 72 Fahrenheit. These samples are tested for their geotechnical index properties, e.g., Atterberg limits. There are also other tests inside the geotechnical laboratory, such as the column setting test, which is separate from the current experiments. For the Current study, the samples are removed from the sealed plastic bucket and placed into the plastic column. They are mixed for ten minutes inside the column and then allowed to settle before being tested using the shaker. (Figure 3.4) Shows the complete sample preparation process. First, the sediments are placed inside the Shaker plastic column.

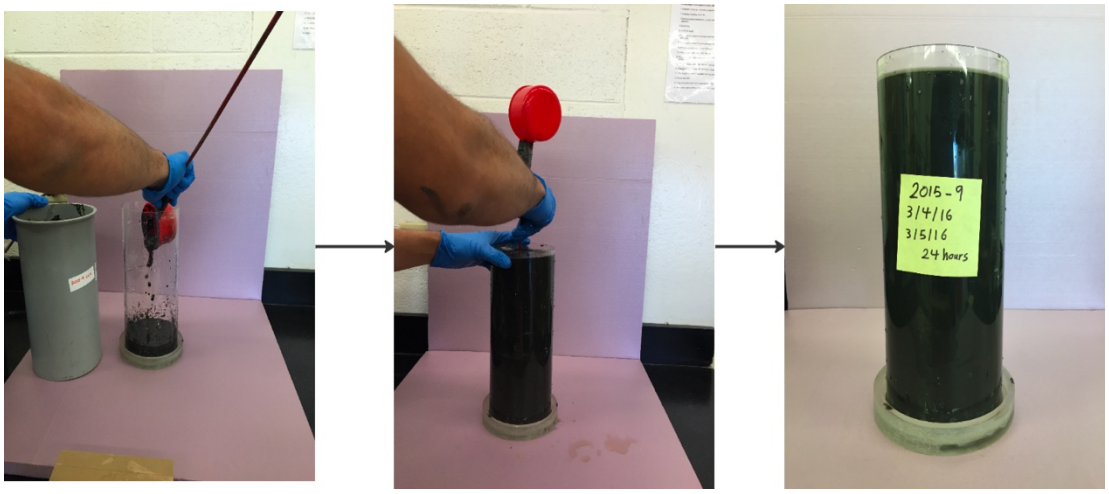

Figure 3-4 Sample preparation for Shaker testing. On the left is the sample placed in the plastic column for mixing. In the middle the soil is mixed inside the column.

The concertation found best suited for the Shaker size is between 90 mg/l and 100 mg/l. However, in some trials, the concentration exceeding 100 mg/l could not be tested using the Shaker due to the column size needing to accommodate the sample while maintaining a 2-inch distance between the grid and the sample

3.4 Laboratory testing

Cheng-Han Tsai and Wilbert Lick designed the shaker in 1986 at the University of California Santa Barbara. This shaker is also known as the Particle Entrainment Simulator (PES) and consists of a plastic cylinder with a grid inside oscillating with an amplitude of one inch. The vertical grid oscillations create a turbulence which penetrates the sediments layer place at the bottom of the water bath (Figure 3.5). This shaker was intended to measure sediment resuspension rapidly on-board vessels or in laboratories. The PES uses a 12V, 3-amp power supply which powers a motor that rotates the driving desk, which causes the vertical rod to move vertically inside the water column.

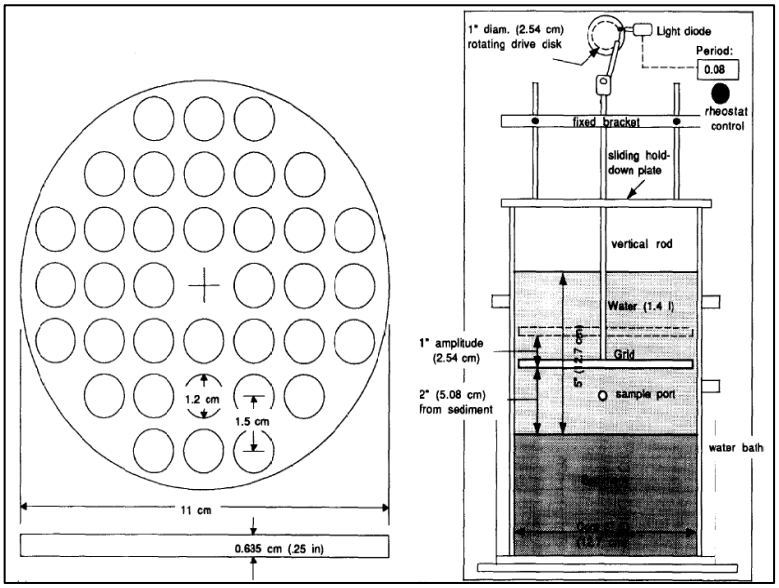

Figure 3-5 Original blueprints of the Shaker. On the left side is the oscillating grid, and on the right side are the Shaker components inside the water bath (Abdelrhman et al., 1996).

The stress generated by the shaker differs from that generated by currents and waves. However, because the shaker was calibrated with flume experiments, the results from the shaker could be an accurate estimate of sediment resuspension (Cheng-Han Tasi & Wilbert Lick, 1986). However, the current study uses the calibration curve as a sanity check on the newly Ansys-modeled shear stresses inside the shaker. This allows different sediments to be tested using the shaker without the need for simultaneous flume experiments.

For the current Lick Shaker tests, all samples undergo self-weight settling for 1, 3, 6, and 12 days. These varied settling times represent an improvement to previous tests conducted by Haralmpides (2000) and Jerolleman (2014), who both used the shaker in their studies. Increasing the settling time allows for a more in-depth characterization of the resuspension and or critical shear stress for erosion vs. settling time relationship. Before the testing procedure begins, a background sample of 60ml is withdrawn from the water column. An improvement to previous tests conducted using the shaker is adding 60 ml of site water (as opposed to tap water) after a sample is collected. Adding site water back into the sample ensures that the water chemical composition is not changed, thus not hindering deposition and resuspension during the test. Once the Shaker starts, the motor's lowest setting was approximately 140 rpm. This initial speed is maintained for 10 minutes. Next, a sample is taken from the top of the water column using a syringe. This is done slowly with minimal interference with the grid to ensure the grid oscillations are not changed. The volume of the sample withdrawn at each interval is replaced with site water, and the RPM is increased by 10%. The new speed influences the bed for 10 minutes before another sample is taken. The same procedure is repeated until the highest setting of the motor is reached, approximately 950 RPM. The duration of each Shaker test is approximately 90 minutes. Total suspended solids (TSS) measurements were conducted. These tests were performed on all samples collected from the Shaker. The TSS analyses equipment shown in (Figure 3.6). These tests are performed in general accordance with Environmental Protection Agency (EPA) Environmental Sciences Section (ESS) Method 340.2. The test included pouring a sample through a 0.47-micron pore size filter and weighing the dried solids on the. A vacuum pump was used to extract the water through the filter, and distilled water was used to rinse the sample. The sample is prelabeled, and once collected, it is stored for no longer than 48hours for turbidity and TSS measurements.

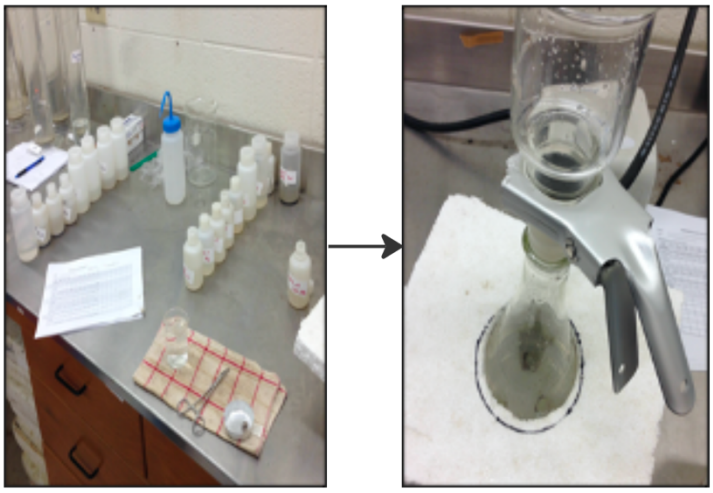

Figure 3-6 Water samples on the left are organized by run number to be passed through filtration apparatus on the right

TSS was calculated using the following equation (Eqn.1):

$$TSS = \frac{W_p}{V_t} * 10^6 \qquad \text{Enq.1}$$

Where, *TSS* is the total suspended solids in grams per liter (g/L), W_p is the weight of dried particles in grams, and V_t is the sample volume in liters.

The turbidity test was performed as an additional check on suspended solids concentrations. The correlation between the TSS and turbidity (Figure 3.7) indicates a good positive agreement between the turbidity and TSS within the Turbidity meter's maximum measuring capacity. This test includes placing the sample in a vial and a turbidity meter The vial must be cleaned with a microfiber cloth and inverted twice to ensure no bubbles disturb the sample reading. The value displayed on the machine was recorded in NTUs (Figure 3.8).

The total suspended solids concentration (TSS) was calculated using the following equation (Eqn.2):

$$TSS = \frac{1000 * W_p}{\frac{W_p}{G_s} + W_w} \qquad \text{Eqn.2}$$

Where TSS is the suspended solids, W_p is the weight of the dry particles, G is the specific gravity, W_w is the weight of water. For all TSS measurements in the current study, please see Appendix B. Some of these measurements could not be plotted in figure 3-8 as they fell outside the Turbidity Meter used maximum capacity of 4500 [NTU].

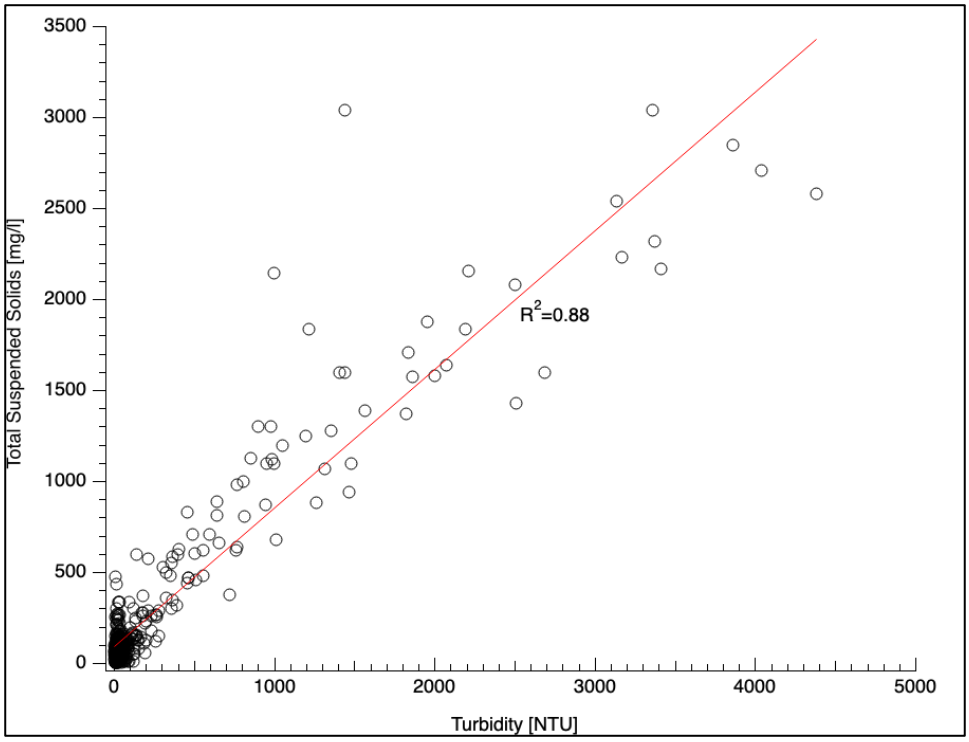

Figure 3-7 The Scatter plot between turbidity and TSS [mg/l]. The x-axis represents the turbidity measurements with their corresponding y-axis TTS measurement for tested samples. good correlation exists for TSS [mg/l] with turbidity measurements for all samples tested.

Figure 3-8 Turbidity meter used to test water samples from the shaker

Chapter 4 Laboratory Experimental Results

4.1 Shaker resuspension analysis procedure

After Shaker experiments were completed the following equations were used the analyze primary data from the Shaker to obtain a resuspension rate; this procedure was formulate by Abdelrhman et al. (1996). The E' (t) the net Erosion rate or entertainment rate was calculated using the following equation (Eqn.3):

$$E' = \left[d \frac{\Delta C}{\Delta t} \right] + C V_s \qquad \text{Eqn3}$$

Where d is the depth of water in the cylinder, ΔC is changed in concentration between each run, Δt change is time (Lavelle and Davis 1987), *Vs*, which is settling velocity, and *C is* the concentration in mg/L

The Actual entertainment rate was calculated using the following equation (Eqn.4):

$$E = E' + D(t) \qquad \text{(Eqn.4)}$$

where *E* is the Actual entertainment rate, E' is the net entrainment rate per unit area of the bed, and *D(t)* is the deposition rate per unit area of the bed (Abdelrahman et al., 1996).

The deposition rate was calculated using the following equation (Eqn.5):

$$D = V_S \, C \qquad \text{(Eqn.5)}$$

Calculating *Vs*, which is settling or depositional velocity, and *c* is the concentration in mg/L, using the following equation (Eqn.6):

$$V_s = V_o \, e^{-kc} \qquad \text{(Eqn.6)}$$

Where *Vo* is hindered settling velocity, *k* is hindered settling coefficient, and *c* is the concentration (Vesilind, 1968).

4.2 Initial experimental results

Before any analysis procedure is conducted, the primary data from the Shaker is plotted. These results included the Recorded RPM at each time interval and the TSS concentration, measured by the filtration processes described in section 3.4. For example, Figure 4-1 shows the Shaker RPM, with TSS concentration mg/l for a settling time of 1 day. The map on the graph represents the area from which this sample was taken. It is evident from Figures 4-1, 4-2, 4-3, and 4-4 that as the settling time increases, the RPM settings increase. For example, in comparing figure 4-1, maximum RPM setting of 300 for 1-day settling, to figure 4-4, maximum RPM of 900, with settling of 12 days. This increase in RPM required to mobilize sediments is because as the samples are allowed to consolidate self-weigh, the bed shear strength increases.

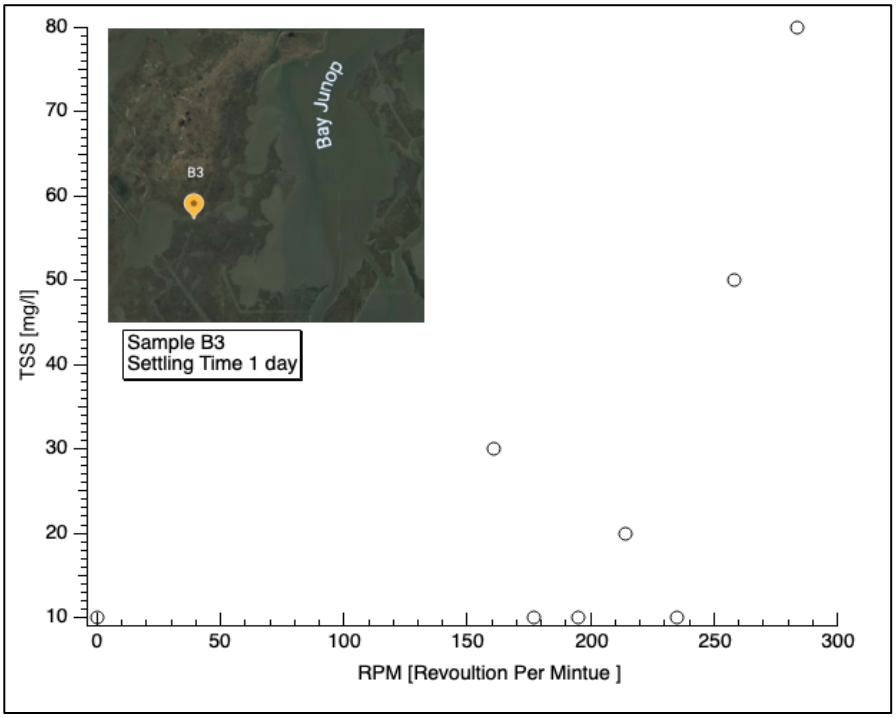

Figure 4-1 Show the primary resuspension test results for one day of settling time. The x-axis in the rpm setting of the shaker and the y-axis is the TSS measurements [mg/l].

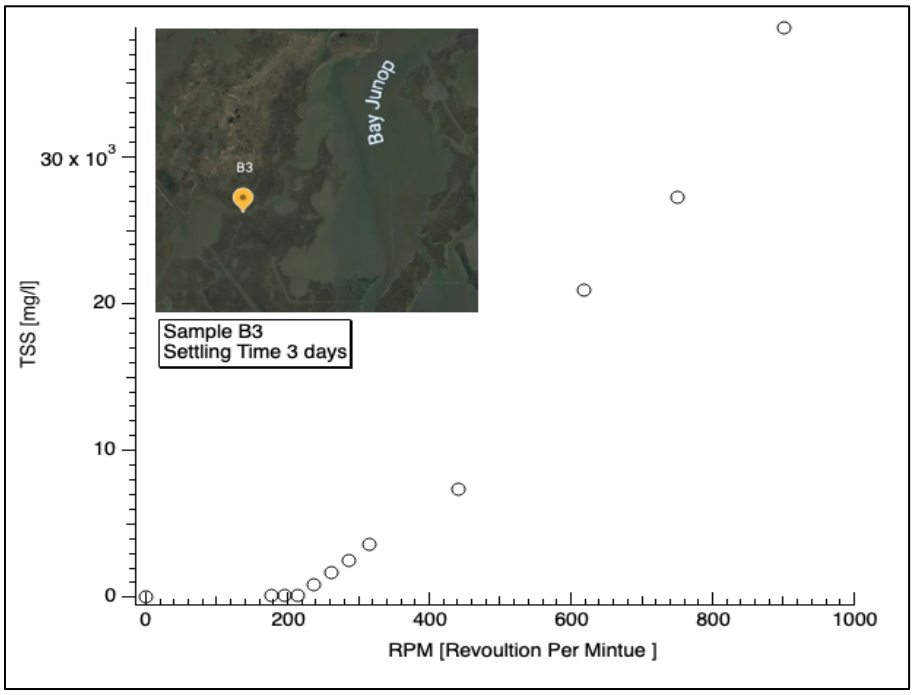

Figure 4-2 Show the primary resuspension test results for three days of settling time. The x-axis in the rpm setting of the shaker and the y-axis is the TSS [mg/l] for that setting.

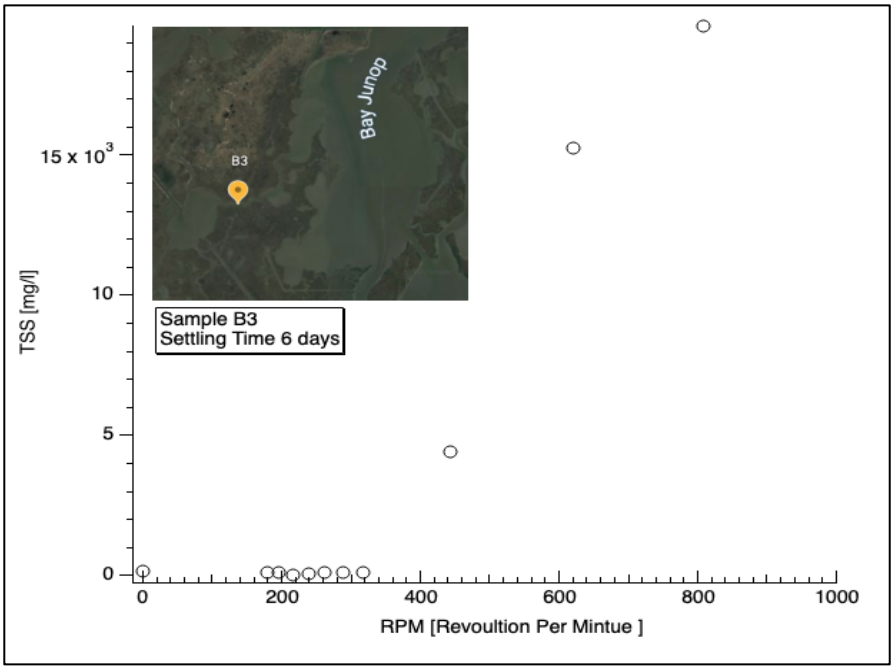

Figure 4-3 Show the primary resuspension test results for six days of settling time. The x-axis in the rpm setting of the shaker and the y-axis is the TSS [mg/l] for that setting.

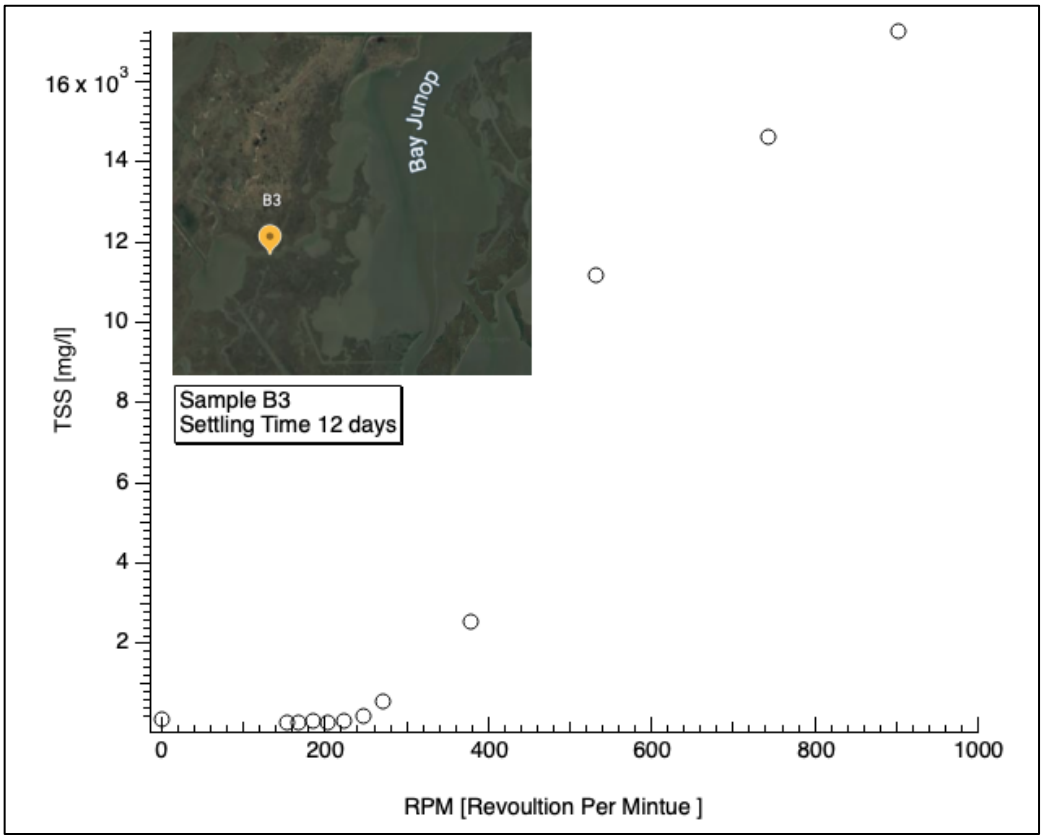

Figure 4-4 Show the primary resuspension test results for 12 days of settling time. The x-axis in the rpm setting of the shaker and the y-axis is the TSS [mg/l] concentration for that setting.

Chapter 5 Ansys Computational Fluid Dynamics (CFD) Shaker Model

5.1 Motivation for modeling the Shaker in Ansys

Tasi and Lick developed the Shaker in 1986. The primary purpose of creating the shaker was for rapid measurements of resuspension. For economics, the shaker is the best choice for erosion measurements when compared to other erosion-measuring devices discussed in Chapter 2. The shaker is also small and compact, meaning grab samples can easily be tested without long sample preparation times. Moreover, the amount of sample required is minimal compared to laboratory flumes. However, the shaker has a significant drawback because flow conditions and shear stresses inside the shaker are unknown (Jaspen, 2005). In addition, concentration calibrations are only valid for identical sediments and sediment conditions, such as self-weight settling times (Jaspen, 2005). This sediment type and sediment condition dependability are evident in Figure 5-6. For example, at 450 RPM, the percentage difference between Lick's 1986 curve and Lick's 1994 curve for shear stress estimation is 127%. In summary, it is evident that when a new sediment type is tested, the shaker requires a new calibration with a flume. Note that this calibration is concentration-based and not shear-stress calibration. Figure 5.1 shows the concentration every

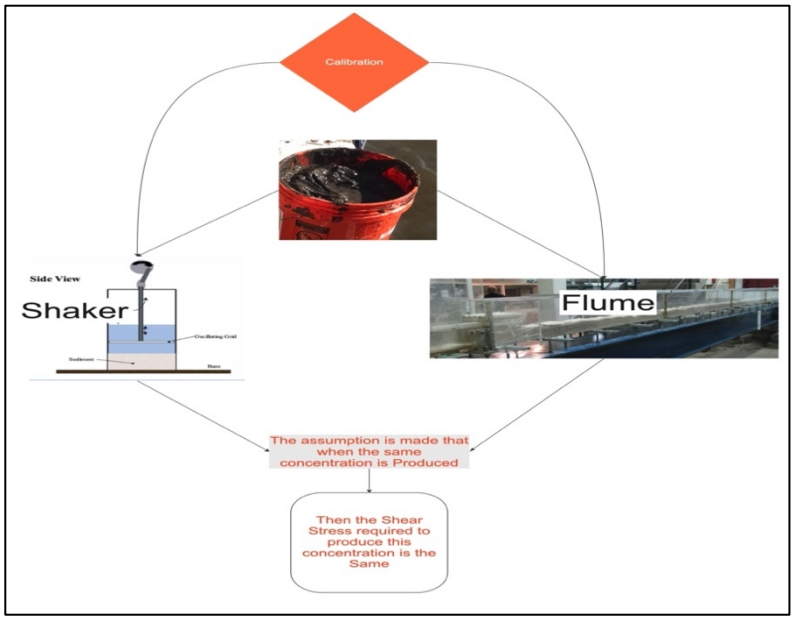

Figure 5-1 The schematic showing Shaker calibration procedure

time new sediments are tested using the Shaker. If this calibration process is fully completed, the

Shaker economic edge is eliminated since two laboratory experiments are needed for every new sample. For the reasons discussed above. A 2D CFD model of the Shaker is created to approximate flow conditions and shear stress values generated by the Shaker. This model will allow improved postprocessing of the erosion tests and change the shear stress calibration curve from flume dependent to Ansys CFD-calculated stress.

5.2 Advantages of using Ansys

- Ansys is a powerful standalone interface with a user-friendly environment and advanced meshing options
- Ansys integrated with two standards, American National Standard Institute and American Society of Mechanical Engineering sections used for example, to design nuclear reactors.
- Transient analysis can be completed economically
- Ansys allow the implementation of complex geometries, constraints, and coupled analysis.

5.3 Governing equations used in Ansys

For all flows, Ansys solves the conservation of mass and conservation of momentum equations.

The mass conservation equation or continuity equation is written as follows (Eqn.7):

$$\frac{\partial \rho}{\partial t} + \nabla . (\rho \vec{v}) = S_m \qquad \text{(Eqn.7)}$$

Where S_m is the mass added to the continuous phase from the dispersed second phase (e.g., due to vaporization of liquid droplets) and any user defined sources. The equation above in the general form (Ansys, 2009).

The momentum conservation in an inertial (non-accelerating) frame by Batchelor (1967) is as follows (Eqn.8):

$$\frac{\partial}{\partial t}(\rho \vec{v}) + \nabla . (\rho \vec{v} \vec{v}) = -\nabla p + \nabla . (\bar{\bar{\tau}}) + p\vec{g} + \vec{F} \qquad \text{(Eqn.8)}$$

Where p is the static pressure, $\bar{\bar{\tau}}$ is the stress tensor, and $p\vec{g}$ and $\vec{F}$ are the gravitational body force and external body forces respectively. $\vec{F}$ also contains model-dependent source terms. The stress tensor $\bar{\bar{\tau}}$ is given by (Eqn.9):

$$\bar{\bar{\tau}} = \mu \left[(\nabla \vec{v} + \nabla \vec{v}^T) - \frac{2}{3} \nabla . \vec{v} I \right] \qquad \text{(Eqn.9)}$$

For turbulence the Standard *k*- ε model wad used. This model is robust, economical, and has reasonable accuracy for a wide range of turbulent flows, which explains its popularity in industrial flows (Ansys, 2009). The turbulence kinetic energy, *k*, and its rate of dissipation, ϵ , are obtained from the following transport equations (Eqn.10 & Eqn.11):

$$\frac{\partial}{\partial t}(pk) + \frac{\partial}{\partial x_i}(pku_i) = \frac{\partial}{\partial x_j}\left[\left(\mu + \frac{\mu_t}{\sigma_k}\right)\frac{\partial k}{\partial x_j}\right] + G_k + G_b - \rho\epsilon - Y_M + S_k \quad \text{(Eqn.10)}$$

and

$$\frac{\partial}{\partial t}(p\epsilon) + \frac{\partial}{\partial x_i}(p\epsilon u_i) = \frac{\partial}{\partial x_j}\left[\left(\mu + \frac{\mu_t}{\sigma_\epsilon}\right)\frac{\partial \epsilon}{\partial x_j}\right] + C_{1\epsilon}\frac{\epsilon}{k} + (G_k + C_{3\epsilon}G_b) - C_{2\epsilon}\rho\frac{\epsilon^2}{k} + S_\epsilon \quad \text{(Eqn.11)}$$

Where, G_k represents the generation of turbulence kinetic energy due to the mean velocity gradients. G_b is the generation of turbulence kinetic energy due to buoyancy. Y_M is the contribution of the fluctuating dilatation in compressible turbulence to the overall dissipation rate.

The turbulent or eddy viscosity, μ_t is calculated by combining *k* and ϵ as follows (Eqn.12):

$$\mu_t = \rho C_\mu \frac{k^2}{\epsilon} \qquad \text{(Eqn.12)}$$

where C_μ is a constant, the turbulence kinetic energy, *k*, and its rate of dissipation, ϵ.

For the current model the constants used had the following values (Eqn.13):

$$C_{1\epsilon} = 1.44, C_{2\epsilon} = 1.92, C_\mu = 0.09, \sigma_k = 1.0, \sigma_\epsilon = 1.3 \quad \text{(Eqn. 13)}$$

The above constants values are Ansys default values determined from experiments with air and water for turbulent shear flows and decaying isotropic grid turbulence. They have been found to work reasonably well for wall-bounded and free-shear flows (Ansys, 2009).

5.4 Modeling procedure

First step before modeling the Shaker is drafting its geometry. The drafting was completed in Soildswork using the Shaker's original blueprints shown in section 3 (Figure3.5). The model is then imported into Ansys for simulations. The Shaker was initially modeled in 3D and had 2,842,470 nodes and 16,337,988 elements. However, it encountered many computationally demanding errors and uneconomical computational times. It was then modeled as 2D using 13,581 nodes and 13,013 elements. Converting the shaker's geometry from 3D to 2D reduces the computational performance and overall efficiency. However, 2D conversion reduces the accuracy of turbulence modeling inside the shaker. The accuracy should not be affected substantially since the shaker is dimensionally small, about 0.0038m^3. Another potential drawback is modeling the soil surface as a flat solid. The soil inside the water column is not perfectly flat, and throughout

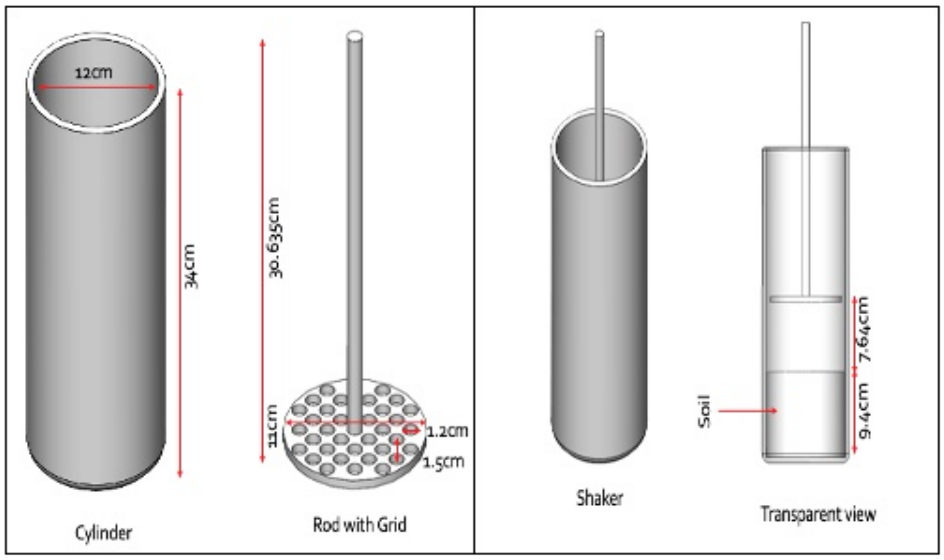

Figure 5-2 Lick Shaker modeled in Soildswork

the Shaker experiment, the surface of the bed changes as sediment is constantly eroded. Finally a potential uncertintiy inside the Shaker comes from modeling the grid with six circular pentrations and then replicating the results assuming five penetrations at each location. This could yield different results and requires futher investigation by using a full 3D model. Furthermore, the grid structure cannot be resolved entirely in 2D, and the results from the centerline of the grid were approximated to other locations on the grid structure itself. This could influence the results.

In Ansys simulation a pressure-based solver was used, and the fluid was assumed to be incompressible, and transient time. Fluid selected inside the column was water with a density of 998.2 kg/m^3 and viscosity of 0.001003 kg/m-s. (Figure 5.3) shows one amplitude of the shakers

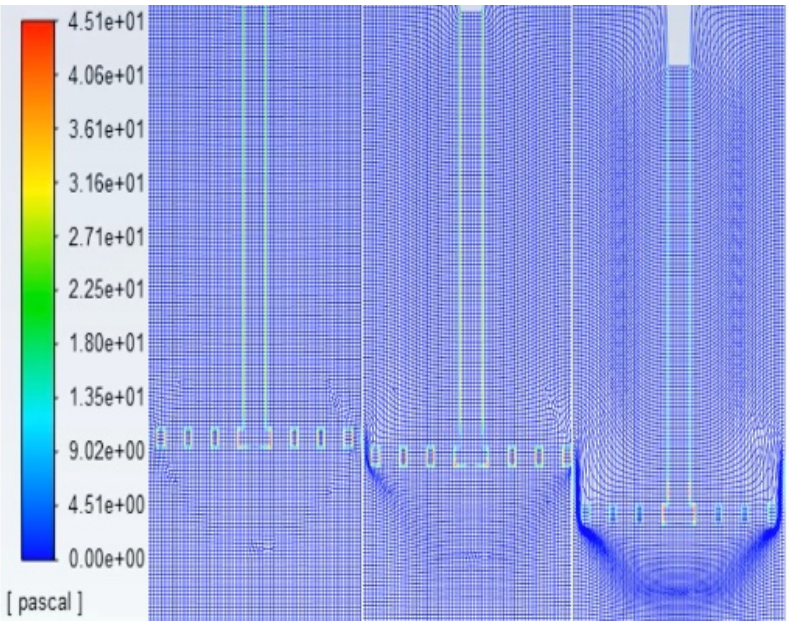

Figure 5-3 shows the modeling of 1 amplitude of the shaker as the grid moves down into the water bath

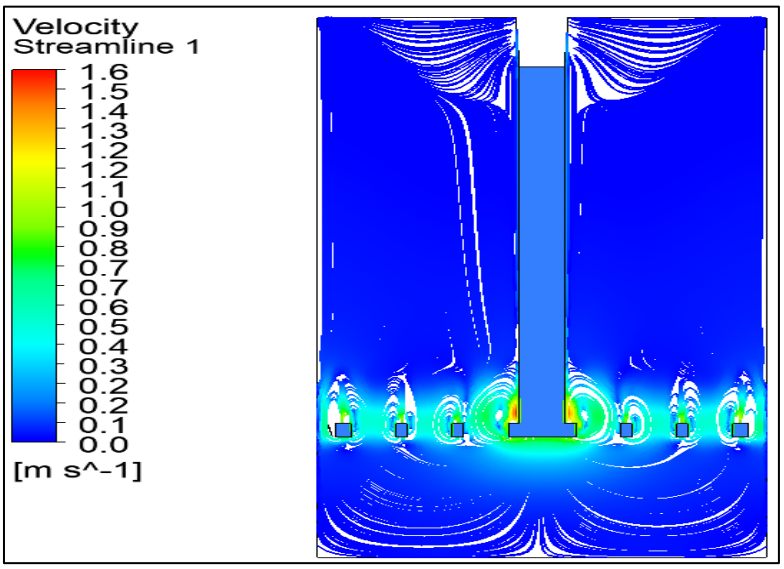

Figure 5-4 shows velocity streamlines generated by the Ansys simulation

oscillation as modeled in ANSYS. (Figure 5.4) shows velocity streamlines around grid openings and inside the water bath.

The software allows the use of a dynamic mesh option, which allows for the modeling of moving parts without the need of overset meshing which introduces interpolation errors at the component/background interface (ANSYS, 2018). For the current model, the dynamic mesh option was used, and the solver used is pressure-based. The 2D space is planar since the slider has a linear velocity converted from angular velocity. This velocity conversion was done using the basic slider crank equations. There is no rotational body inside the water column hence the 2D model is sufficient and economical in computational power and execution time.

Finally, a sensitivity analysis was completed using both a fine and coarse mesh. The sensitivity analysis resulted is the same order of magnitude bed shear stresses (Table 5-1). Finally, a fine mesh was selected as it is more likely to resolve flow around the grid and cylinder walls more effectively. For turbulence, the Standard k-epsilon (2 equation) model was selected and transitional *K- kl*-ω models were used to model turbulence inside the Shaker. Table 5-1 shows the bed shear stress values using different approaches, these results show that the effect of mesh size on the magnitude of bed shear stress was in the same order of magnitude. Moreover, the results from the fine mesh and *K-epsilon* turbulence model were selected for erosion test RPM conversions as they are more likely to better resolve flow around the grid and cylinder walls due to high nodes and element presence.

Moreover, It was necessary to operate the Lick shaker equipment with a frequency between 100 and 900 RPMs. However, the Lick Shaker curves are only accurate for frequency less than 800 RPMs and more than 100 rpm see (Figure 5.5) showing all Shaker calibrations used in past studies.

Case Number	Turbulence Model	Mesh	Max. Velocity, water	Bed Shear Stress	Total Force at the Bed
			[m/s]	[Pa]	[N]
1	K-epsilon	Fine	1.6	0.15	5
2	Transition k-kl		1.7	0.16	5.5
3	K-epsilon	Coarse	1.9	0.4	3.1
4	Transition k-kl		1.6	0.38	3

Table 5-1 Sensitivity analysis results using different turbulence models listed here and different mesh sizes

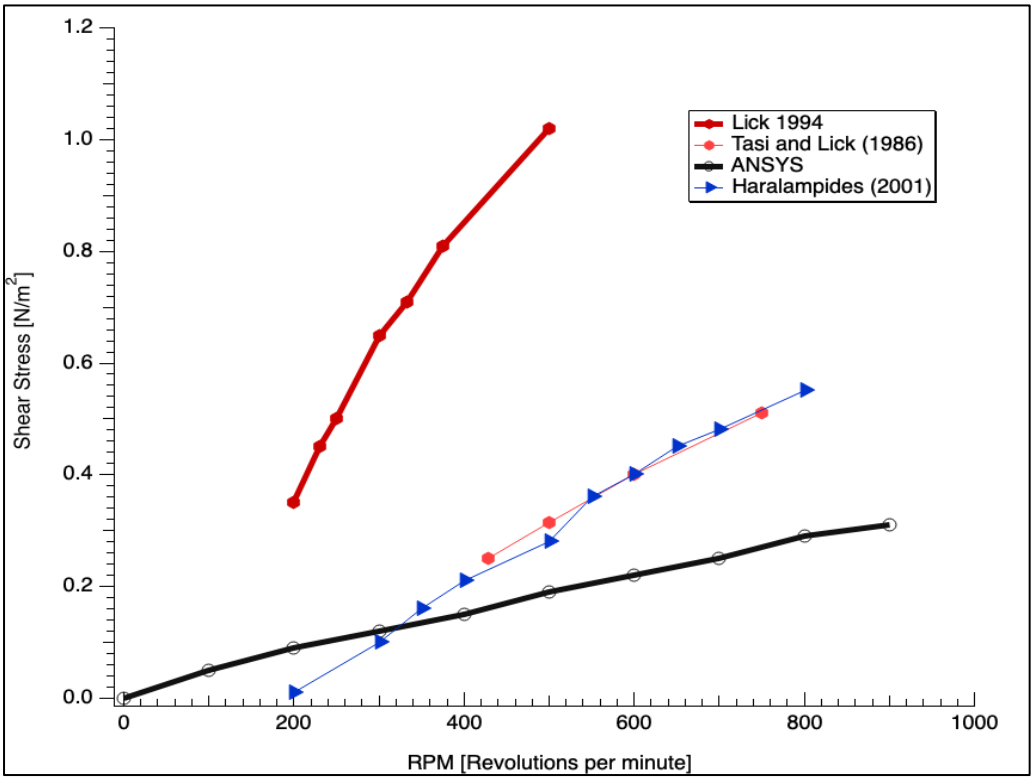

Figure 5-5 The relationship between RPM and shear stress The Black curve is ANSYS modeled. Blue curve from (Haralampides, 2001) Orange Curve (Tasi et al.1986) red curve is redrawn from (DePinto & Lick et al.,1994)

Figure 5.5 Shows all the different calibration curves for the Lick Shaker in the literature. These curves convert the Shaker RPM into shear stress for the resuspension analysis. The black curve is the newly modeled curve based on flow conditions inside the Shaker. Note that previous calibration curves did not cover RPMs below 200 and did not reach RPMs above 800. Therefore, the newly modeled curves reached these Shaker settings observed during the current experiment.

5.5 Statistical significance of the Ansys model

For the bed shear stresses generated by the grid oscillations a two-tailed paired samples *t*-test was conducted to examine whether the mean difference of maximum wall shear stress (Max-WSS) and average wall shear stress (Avg_WSS) was significantly different from zero.

The result of the two-tailed paired samples *t*-test was significant, $t\ (8) = 6.43$, $p < .001$. This finding suggests the difference in the mean of Max_WSS and the mean of Avg_WSS was significantly different from zero. The mean of Max_WSS was significantly higher than the mean

of Avg_WSS. The results are presented in Table 5-2. A bar plot of the means is presented in Figure 5-6. Moreover, A Pearson correlation analysis was conducted between Max_WSS and Avg_WSS. A significant positive correlation was observed between Max_WSS and Avg_WSS, with a correlation of 0.999, indicating a large effect size ($p < .001$). This suggests that as Max_WSS increases, Avg_WSS tends to increase.

Max_WSS [Pa]		Avg_WSS [Pa]				
M	*SD*	*M*	*SD*	*t*	*p*	*d*
0.32	0.15	0.19	0.09	6.43	< .001	2.14

Note. N = 9. Degrees of Freedom for the *t*-statistic = 8. *d* represents Cohen's *d.*

Table 5-2 shows Two-Tailed Paired Samples t-Test for the Difference Between Max_WSS and Avg_WSS

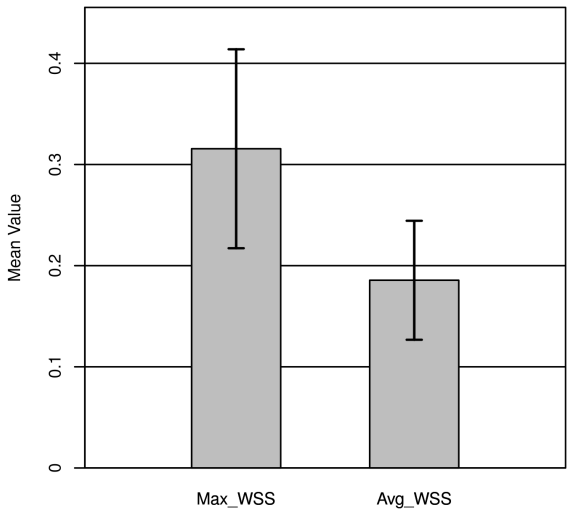

Figure 5-6 The means of Max_WSS [Pa] and Avg_WSS [Pa] with 95.00% CI Error Bars

An analysis of variance (ANOVA) was conducted to determine whether there were significant differences in Shear Stress by the different existing shaker calibration curves. The results of the ANOVA were significant, $F(3, 26) = 10.63$, $p < .001$, indicating there were significant differences in shear stress among the existing calibration curves (Table 5-3). The eta squared was 0.55 indicating Category explains approximately 55% of the variance in Shear Stress. The means and standard deviations are presented in Table 5-4.

Term	*SS*	*df*	*F*	*p*	η_p^2
Category	0.86	3	10.63	< .001	0.55
Residuals	0.70	26			

Table 5-3 shows analysis of variance table for Shear Stress estimations using the different existing calibration curves

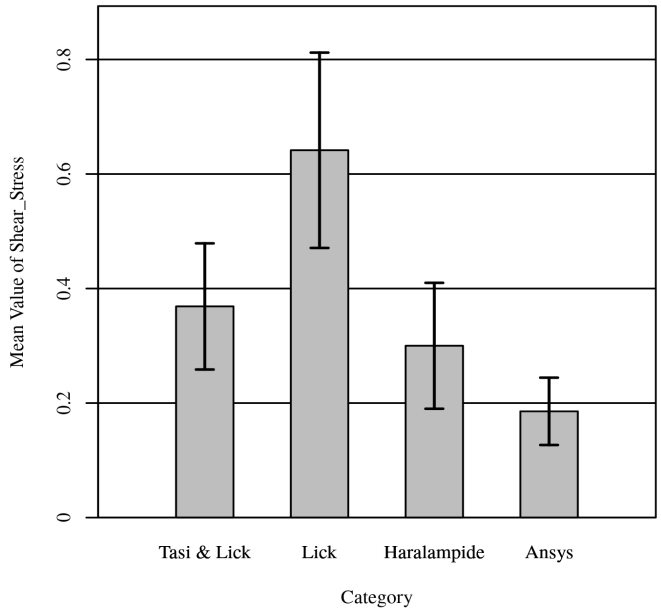

Figure 5-7 Means of shear stress [Pa] by the three different calibration types with 95.00% CI Error Bars

Combination	*M*	*SD*	*n*
Tasi & Lick (1986)	0.37	0.11	4
Lick (DePinto & Lick et al.,1994)	0.64	0.23	7
Haralampides (2000)	0.30	0.18	10
Ansys	0.19	0.09	9

Table 5-4 Mean, Standard Deviation, and Sample Size for Shear Stress by the different published calibration curves

Post-hoc analysis for the main effect of calibration curves, the mean of shear stress [Pa] for Lick ($M = 0.64$, $SD = 0.23$) was significantly larger than for Haralampides ($M = 0.30$, $SD = 0.18$), $p = .001$. For the main effect of category, the mean of shear stress for Lick ($M = 0.64$, $SD = 0.23$) was significantly larger than for current Ansys ($M = 0.19$, $SD = 0.09$), $p < .001$. No other significant effects were found. A bar plot of the means is presented in Figure 5-7 shows the differences in shear stress [Pa] estimations using different calibration curves.

Chapter 6 Analyses of Experimental Data

6.1 Critical shear strength

In the resuspension of cohesive soils, sediment is entrained when the shear stress acting on the sediments exceeds the shear strength holding the sediments. Winterwerp et al. (2004) show the different mechanisms by which erosion could occur. In the current study, two modes of erosion were observed. The first is surface erosion, a drained failure in which no change in pore water occurs due to loading. Second is mass erosion, an undrained failure as water can't drain out of the soil during failure.

The erosion threshold is a parameter used to describe the onset of erosion and sediment transport processes. Moreover, because of the difficulty in determining the start of resuspension, an abrupt change in the total suspended solids concentration is often used to determine the critical shear stress that initiates erosion. Therefore, in section 6.2, two erosion-critical shear stresses will be analyzed one is for surface erosion, and the other is for mass erosion.

6.2 Surficial and mass critical shear strength

After the Shaker resuspension test is completed, the results are analyzed for critical shear stress of erosion. This analysis is a graphical procedure that involves graphing the results and determining the shear stresses responsible for the rapid increases in concentration. Figure 6-1 shows the increase in concentration as stress increases inside the Shaker. After resuspension test are completed, and the results are analyzed for critical shear stress of erosion. This analysis is a graphical procedure that involves graphing the results and determining the shear stresses responsible for the rapid increases in concentration. Figure 6-1 shows the increase in concentration as stress increases inside the Shaker. Initially, the concentration increase is minimal, indicating that the sediment bed actively resists the Shaker's forces. However, at 0.096 N/m^2 visible increases in concentrations implies that at least the surface layer of sediment is being resuspended. As the Shaker generates more significant stresses, e.g., at 0.116 N/m^2, it is visible that concentrations are increasing at a higher rate which implies that mass erosion of the bed material has started. This two-stage resuspension behavior allows the estimation of a critical shear stress for surface erosion τc [Pa] surface and a critical shear stress for mass erosion τc [Pa] mass. The same behavior can be seen in (Figures 6-2, 6-3, and 6-4). This surface and mass erosion characterization was only

possible due to the longer-duration shaker tests. Early erosion tests using the Shaker only characterized the surface erosion critical shear stress.

The same critical shear analysis was completed for all Samples tested; these plots can be found in Appendix A. In addition, the associated geotechnical properties of the sample, settling time, and sample geographic location is reported on all plots. One of the goals of this study was to provide engineers and scientists with necessary sediment transport modeling inputs. By presenting how the critical shear stress is determined and including all the relevant geotechnical engineering parameters, an engineer or scientist can decide whether to decrease the critical shear stress value and perhaps be more conservative or increase the value depending on site-specific conditions. However, it should be noted that this data is site-specific and represents resuspension behavior at one time. Therefore, it is challenging to predict the properties of these sediments at a later time. For example, after a storm, when mass transport occurs, sediment is mixed with other grain sizes leading to very different erosion properties.

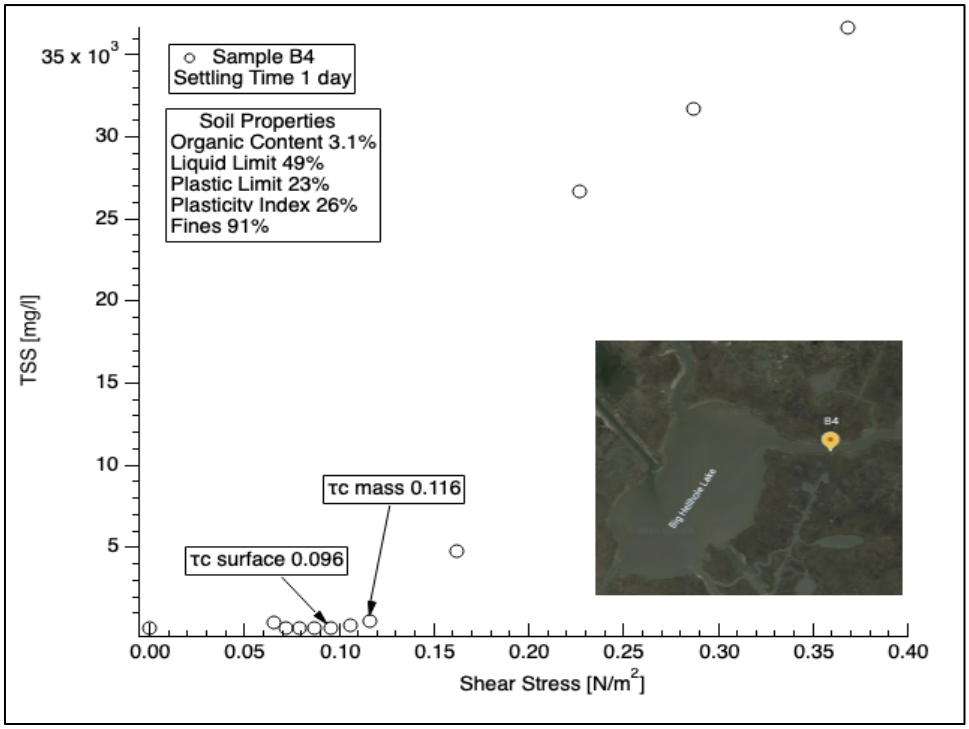

Figure 6-1 Concentrations inside the Shaker as a function of bottom shear stress [Pa]. For sample B4 with one day settling time τc shows the erosion critical shear stress for surface and mass erosion.

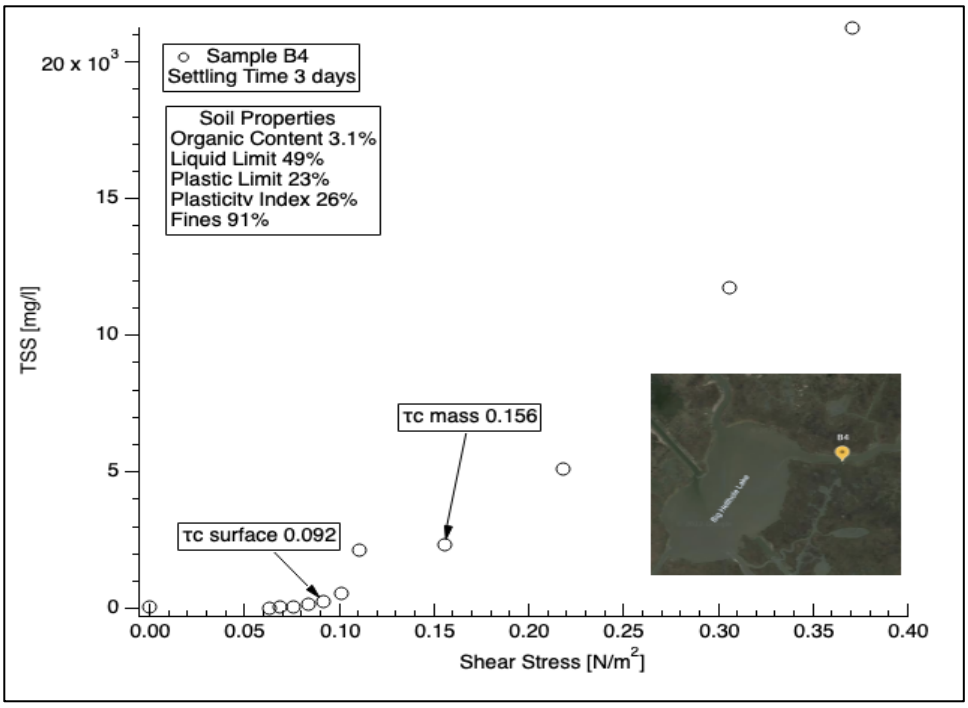

Figure 6-2 Concentrations inside the Shaker as a function of bottom shear stress. For sample B4 with three days of settling time τc [Pa] shows the erosion critical shear stress for surface and mass erosion.

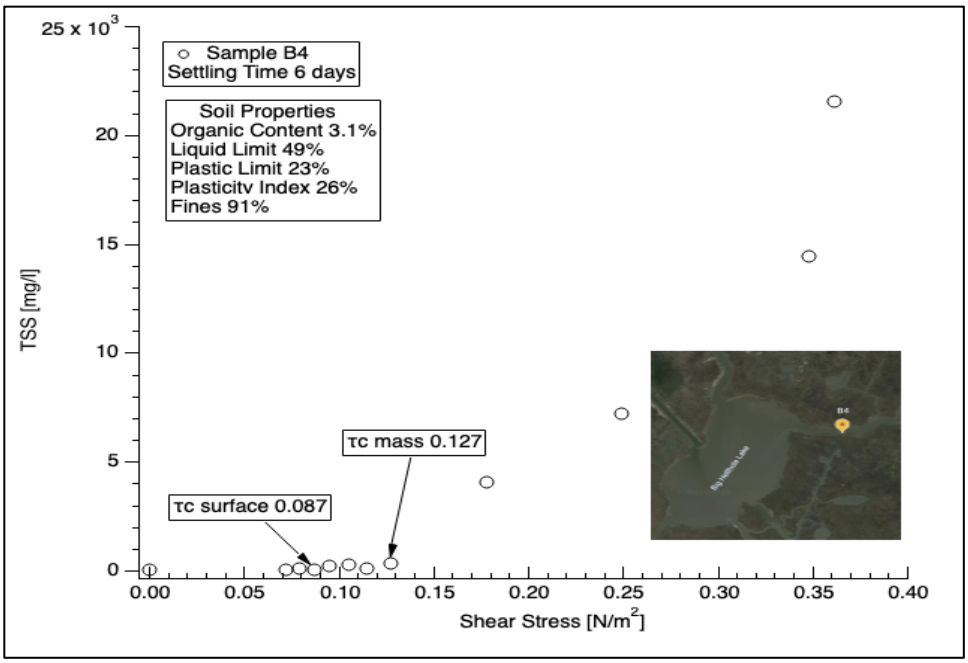

Figure 6-3 Concentrations inside the Shaker as a function of bottom shear stress. For sample B4 with 6 days of settling time τc [Pa] shows the erosion critical shear stress for surface and mass erosion.

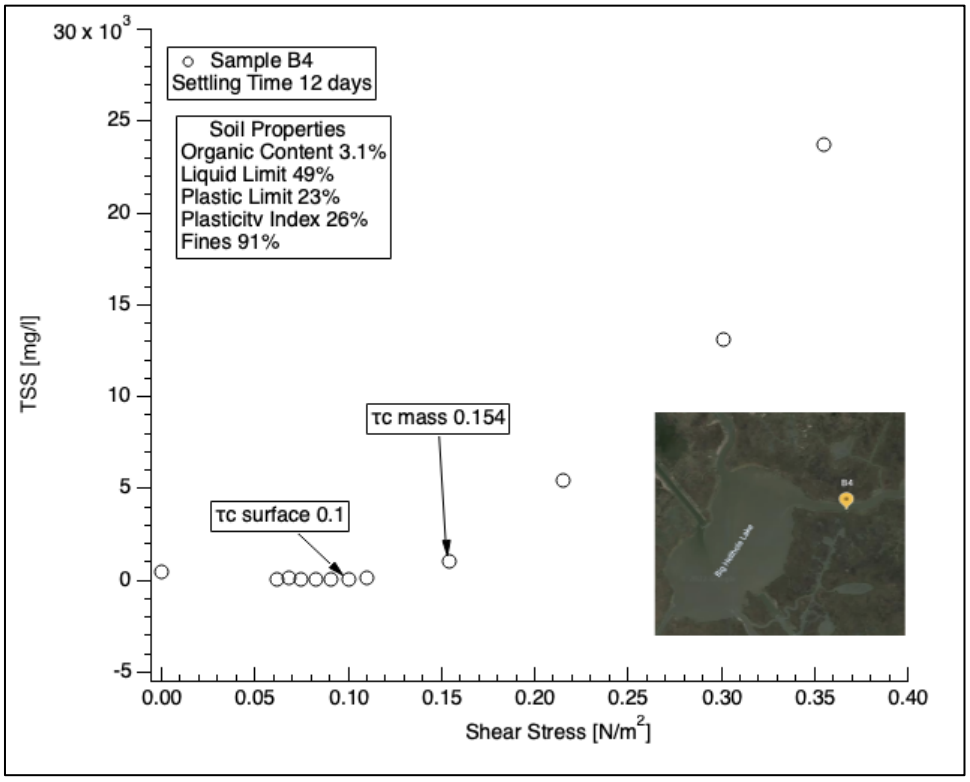

Figure 6-4 Concentrations inside the Shaker as a function of bottom shear stress. For sample B4 with 12 days of settling time τc [Pa] shows the erosion critical shear stress for surface and mass erosion.

6.3 Erosion rates and excess shear formulations

From the experimental results, the below formulation is proposed. (Eqn.14) was found between salinity and settling time (Figures 6-5, and 6-6). Based on four samples with an average liquid limit of 50.3 and a plasticity index of 23.5, respectively. The constant next to the excess shear term is another calibration coefficient known as *(m)*. This empirical erosion constant is a function of soil properties (Partheniades, 1962), (Ariathurai, 1974). These relationships aim to improve the sediment redistribution calibration parameters in the 2017 Louisiana master plan.

$$\boldsymbol{\varepsilon = m\,(\tau_b - \tau_c)}$$

$$\begin{aligned} m &= 0.71 \Rightarrow S_t \leq 1\ day \\ m &= 0.54 \Rightarrow St \leq 3\ days \\ m &= 0.41 \Rightarrow S_t \leq 6\ days \\ m &= 0.35 \Rightarrow S_t \leq 12\ days \end{aligned} \qquad \text{(Eqn.14)}$$

$$If\ \ 4 \leq Salinity(ppt) \leq 10$$

Where ε is the erosion rate (g.m^{-2}. s^{-1}), and S_t is the settling time (days). These coefficients are a

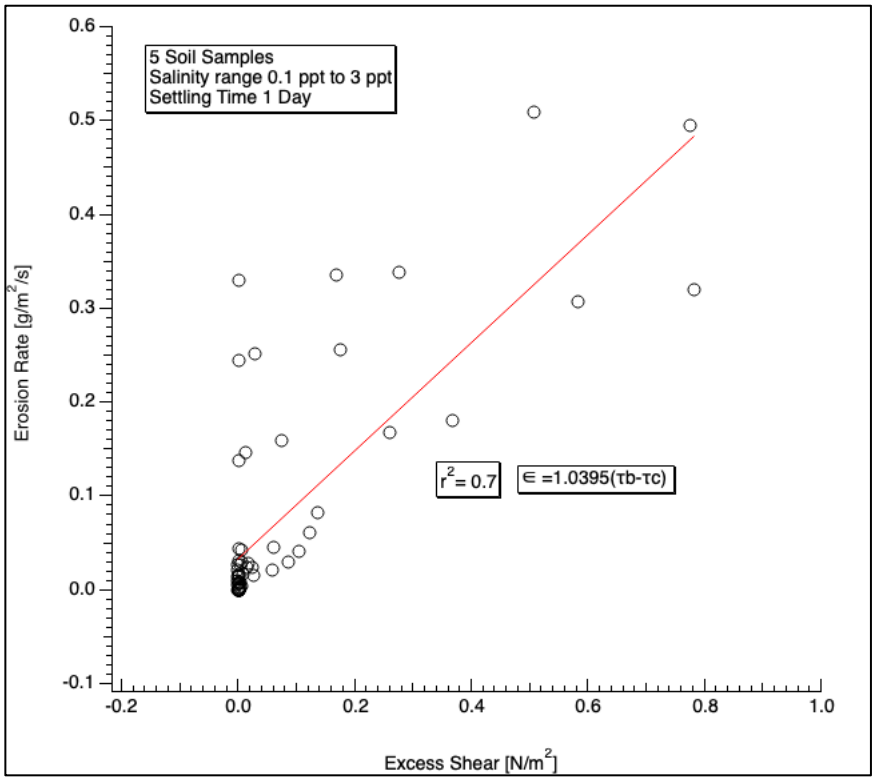

Figure 6-5 Erosion rate [g.m^{-2}. s^{-1}] obtained experimentally along with (*m*) coefficient. Note This is for 1-day self-weight settling

function of bed properties, and experimental data should be used when available. However, it

should be noted that these relationships are based on six series that have been tested for 24 runs using a range of settling times. Another two sets of equations have been developed using two salinity ranges of 4 to 10ppt and one series for 32ppt (Eqn.15). All Similar plots will be found in appendix A.

$$\boldsymbol{\varepsilon = m\,(\tau_b - \tau_c)}$$

$$\begin{aligned} m &= 0.71 \;\Rightarrow S_t \leq 1\ day \\ m &= 0.54 \;\Rightarrow\; St \leq 3\ days \\ m &= 0.41 \;\Rightarrow S_t \leq 6\ days \\ m &= 0.35 \Rightarrow S_t \leq 12\ days \end{aligned} \qquad \text{Eqn.15}$$

$$If\ \ 4 \leq Salinity(ppt) \leq 10$$

The equations above were based on four experiments, with 16 runs on samples with an average plasticity index of 25.8% and a liquid limit of 55%.

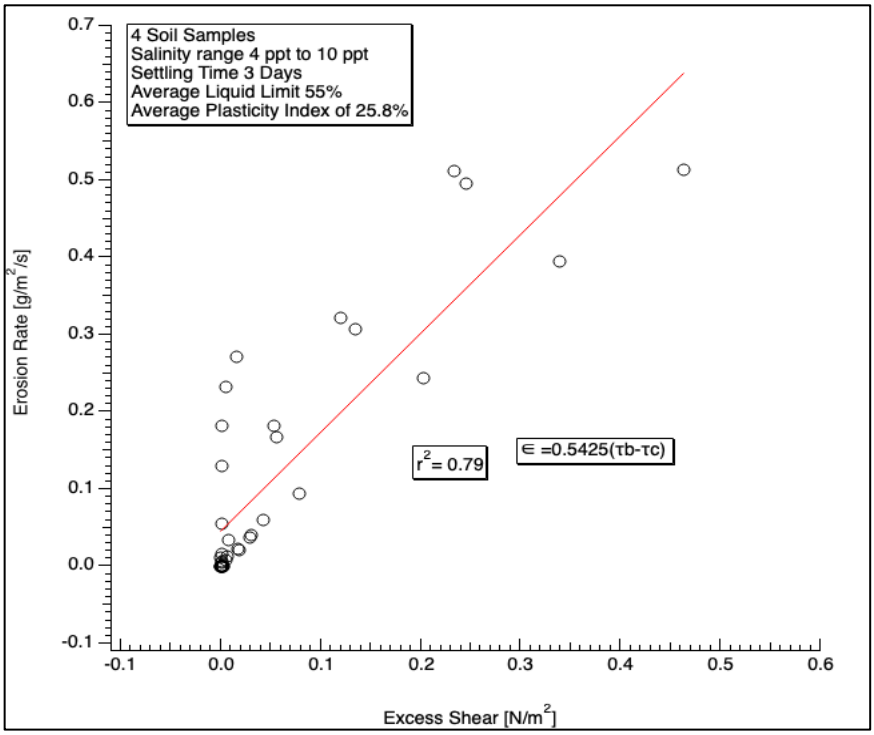

Figure 6-6 Erosion rate [g.m^{-2}. s^{-1}] obtained experimentally along with *(m)* coefficient. Note This is for 3-days self-weight settling

6.4 Plasticity index correlations

Plasticity index correlation with critical shear stress was first developed by Smerdon and Beasley (1959). This following formulation was based on erosion experiments conducted in an open flume with a loose cohesive bed (Eqn.16). Where, τc is in N/m^2, and PI in [%].

$$\tau c = 0.0034(PI)^{0.84} \quad \text{Eqn.16}$$

From current experiments Eqn.17 is developed based on 56 erosion tests. This following relationship is for settling times of twelve days (Figure 6-7). Where, τc is in N/m^2, and PI in [%].

$$\tau c = 0.0231(PI)^{0.74} \quad \text{Eqn.17}$$

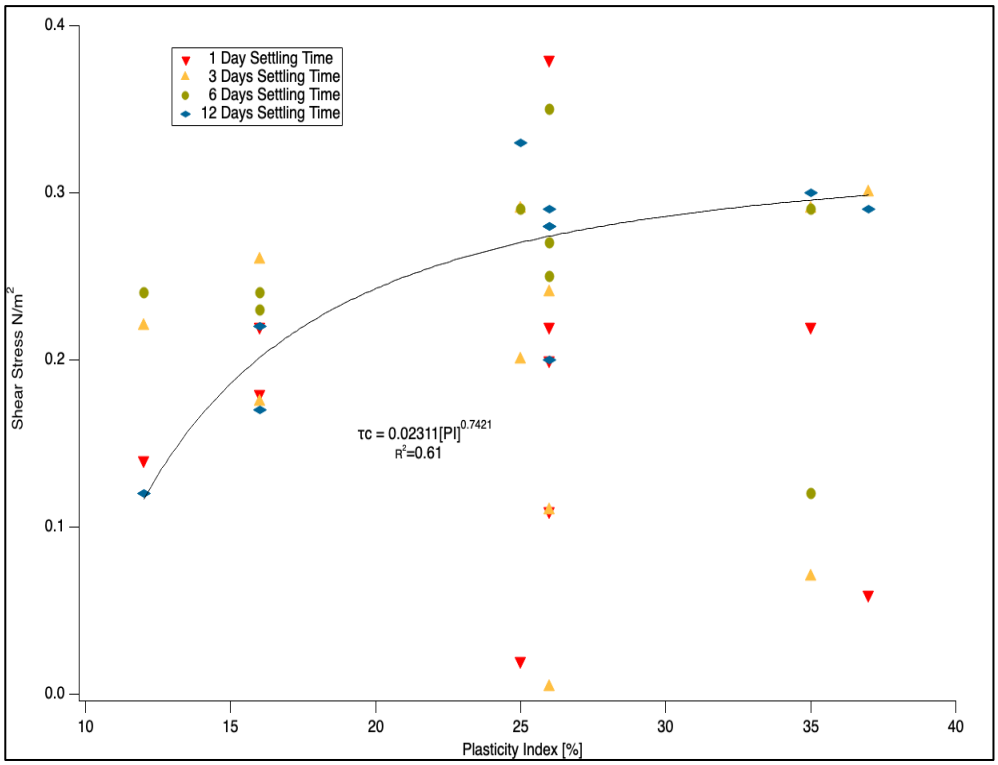

Figure 6-7 The Scatter plot shows the relationship between shear stress and plasticity index. The best fit between plasticity index [%] and critical shear stress [Pa] is shown. Note that different colors indicate different settling time.

6.5 Critical shear stress of erosion and settling times

Based on all the erosion experiments conducted, a critical shear stress relationship was formulated as a function of settling time. A similar relationship of critical shear with settling time was established by Malay et al. (2014). However, that formulation only extended to 4 days of settling time and did not include both surface and mass erosion critical shear stress. For The current study,

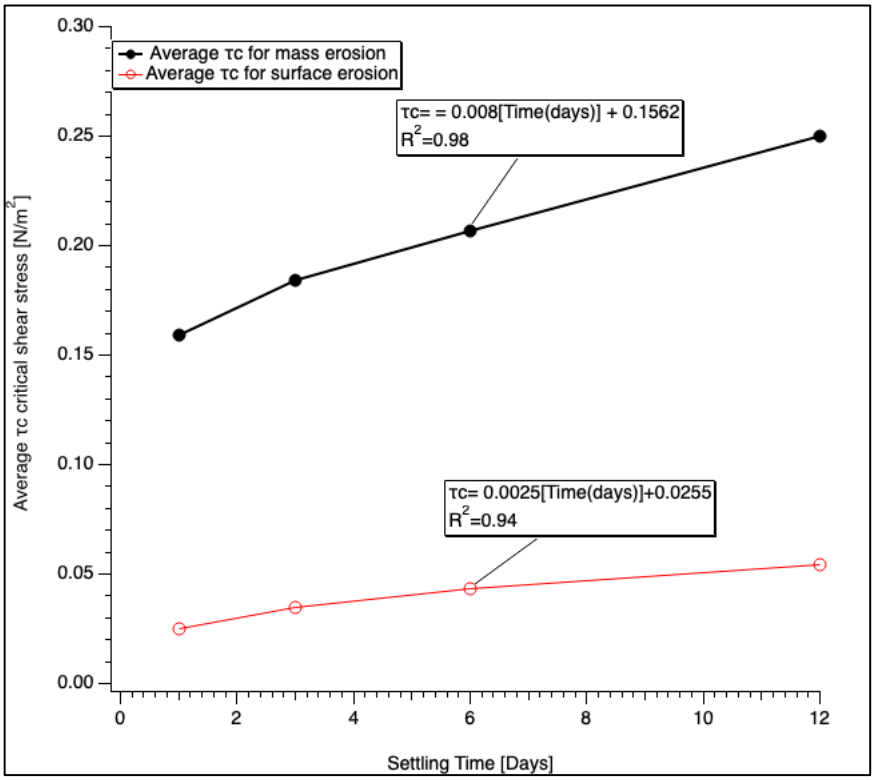

Figure 6-8 Shows the relationship between average critical shear stress and settling time. The red color shows the relationships for shear stress [Pa] τc and black color shows the sample relationship for mass erosion.

Figure 6-8 shows that as settling time increases, the average critical shear stress for surface and mass erosion increases. However, this formulation should not be extended past 12 days unless additional longer resuspension experiments are conducted. The current study found the following equations related settling time to the average mass and surface critical shear stress [Pa] of erosion (Eqn.18 & Eqn.19) (Figure 6-8). Where, τ_c is in [Pa], and Time in [days].

$$\tau_{c\,mass} = 0.008[Time] + 0.1562 \qquad \text{Eqn.18}$$

$$\tau_{c\,surface} = 0.0025[Time] + 0.0255 \qquad \text{Enq.19}$$

Chapter 7 Resuspension and Sediment Distribution Model

7.1 Model theory

The model basis for the open water portion and the marsh accretion in section 7.6 is a simplified version of the CPRA mass balance approach. This mass balance equation was applied to sediment resuspension in open water and marsh platform (CPRA, 2017) (Eqn.20).

$$\frac{\partial C_{k,j}}{\partial t} = -\frac{C_{k,j}\eta_j}{y_j} + \frac{\sum i \sum trib \sum div\left[C_{k,j,i,trib,div} Q_{i,trib,div}\right]}{y_j A_{s,j}} + \frac{f_{dis} \sum_i \lambda_i \frac{A_i}{L_i}\left(C_{k,j} - C_{k,nb}\right)}{y_j A_{s,j}} + \frac{\sum_l S_{r,k,j,l}}{y_j A_{s,j}} \quad Eqn.\,20$$

where: k sediment class, j is number of subcompartment, i number of link, trib is tributary, div is diversion, nb referrers to neighboring subcompartment, dis is dispersivity, r is source sink, s is surface, I is source sink index, $C_{k,j}$ is concentration, Q is water discharge, $A_{s,j}$ is the water surface area, n is water elevation, n' is elevation rate change, $S_{r,k,j,I}$ is the subcompartment source, y_j is subcompartment water depth, t is time, λ_i is diffusivity in link i, L_i is effective link length.

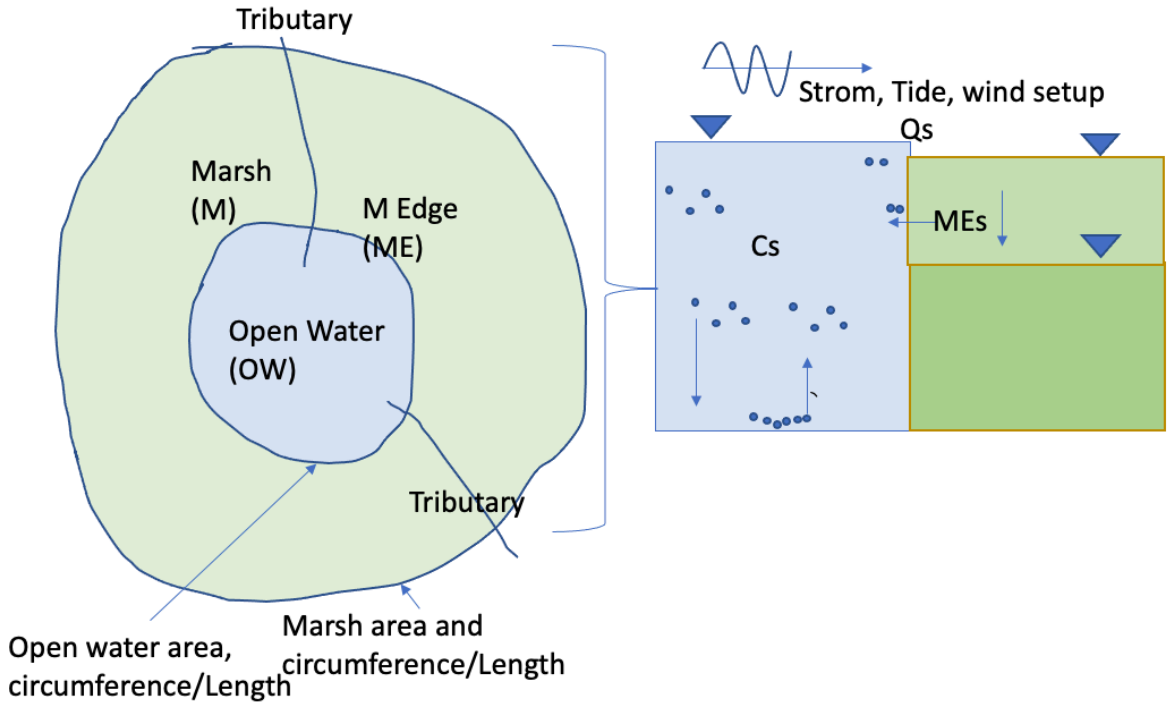

Figure 7-1 Open water marsh exchange processes. On the left is a schematic of the marsh and open water connection needed to model accretion. The right side shows the marsh platform setup for flow rates and elevation with the process drivers.

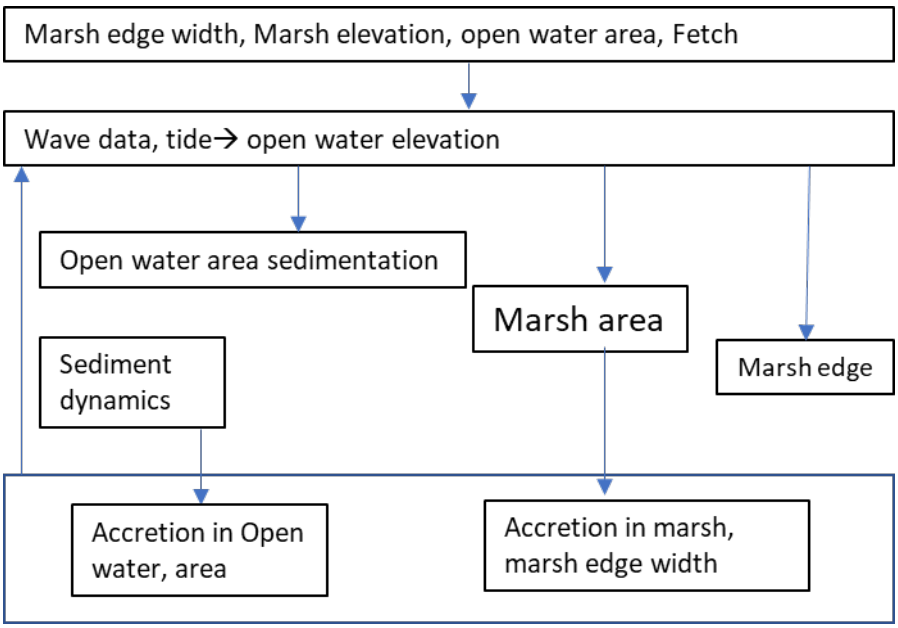

Figure 7-2 Sediment accretion on marsh platform model flowchart showing inputs and variables needed to capture these processes.

The main objective of the numerical modeling of sediment transport is to demonstrate the application of the experimental results in a field situation. Figure 7-1 and 7-2 shows the open water cell setup along with the marsh accretion section. In this study the primary sediments examined are silts and clays with low sand content. However, the model will include a non-cohesive sediments class (sand) to simulate the resuspension of cohesive and non-cohesive sediments. The framework for this modeling approach is based on (CPRA, 2017; (US Army Corps & of Engineers, 2011); Filostrat, 2014). The following equation is used to calculate cohesive sediment resuspension (Eqn.21):

$$E = \frac{a_0}{T_d{}^m}\left(\frac{\tau_b - \tau_c}{\tau_c}\right)^n \qquad \text{Eqn.21}$$

Where E = resuspension potential (mg m^{-2}); a_0 = constant depending on bed material; T_d = time after deposition (days); τ_b = bed shear stress (N.m^{-2}); τ_c = critical shear stress for erosion (N.m^{-2}); m and n, constants dependent on the depositional criteria.

The bed shear stress is calculated using the following equation Eqn.22 (Phillips, 1977)

$$\tau_{b=0.5\rho_w C_f U_b{}^2} \quad \text{Eqn.22}$$

Where C_f = dimensionless friction factor, ρ_w = density of water (kg.m^{-3}), and U_b = bed velocity.

The Young and Verhagan Formulation predicts the energy of wind waves for a given fetch (Young & Verhagen, 1996). Using the following equation Eqn.23:

$$\epsilon = 3.64 \times 10^{-3}.\left(\tanh[A_1]\,.\tanh\left[\frac{B_1}{\tanh[A_1]}\right]\right)^n \quad \text{Eqn. 23}$$

Where,

$$n = 1.74$$

$$A_1 = 0.494\mathcal{S}^{0.75}$$

$$B_1 = 3.13 \times 10^{-3}x^{0.57}, \mathcal{S} = \frac{gd}{U_{10}{}^2}, x = \frac{gf}{U_{10}{}^2}$$

$$v = 0.133\left\{tanhA_2 tanh\left(\frac{B_2}{tanhA_2}\right)\right\}^{-0.37}$$

$$A_2 = 0.133\mathcal{S}^{1.01}$$

$$B_2 = 5.215 \times 10^{-4}x^{0.73}$$

The wind-induced currents are calculated using the following equations Eqn.24 (Rossby & Montgomery, 1935) (US Army Corps & of Engineers, 2011)

$$U_b = U + U_{tide} + U_w + U_{orb} \quad \text{Eqn.24}$$

U_{orb} is the orbital velocity calculated using Eqn. (21), g = gravitational acceleration (m.s^{-2}); H_s = significant wave height (m); T = wave period (s); d = water depth (m).

Wave induced current U_w = (m.s^{-1}) (Eqn.25), depth averaged, K_a = constant related to grain size, calculated using Eqn.25.

$$U_w = K_a U_w \quad \text{Eqn.25}$$

$$U_{orb} = \frac{gH_sT}{2lcosh(\frac{2\pi d}{l})} \qquad \text{Eqn.26}$$

Wavelength can be estimated with reasonable accuracy using the following equations (Eqn.27;Eqn.28) (US Army Corps & of Engineers, 2011):

$$l = l_0 \tanh\left(\frac{2\pi d}{l_o}\right) \qquad \text{Eqn.27}$$

$$l_o = \frac{gT^2}{2\pi} \qquad \text{Eqn.28}$$

Where l_o = deep water wavelength (m), *T* is period, and *d* depth (m).

For sediment deposition rate (m.s^{-1}), the calculation depends on the settling velocity of suspended sediments inside the water column. These velocities are measured in the laboratory using a mini column hindered settling test (Roberts, 2022). The settling velocity can also be calculated using Stoke's law. The following equation (Eqn.29):

$$W_s = \sqrt{\frac{4gD_{50}}{3C_d}(\frac{\rho_s}{\rho_w} - 1)} \qquad \text{Eqn.29}$$

In which D_{50} = mean particle diameter (m), ρ_s = particle densities (kg.m^{-3}); ρ_w= water densities (kg.m^{-3}); and C_d is the coefficient.

To estimate the fraction of clay particles that will form floc. Following Kotylar et al. (1996) 5 ppt threshold will be used as *Ssmax*. The following equation will be used to estimate the percentage of P_{floc} flocculating clay particles (Eqn.30).

$$P_{floc} = \begin{cases} \frac{P_{flocmax}}{S_{smax}} S_s & S_s < S_{smax} \\ P_{floc} & S_s \geq S_{smax} \end{cases} \qquad \text{Eqn.30}$$

S_s is the salinity concentration, S_{smax} is the salinity threshold above which no increase in $P_{flocmax}$ flocculation limit occurs (Kotylar et al., 1996);(CPRA, 2017);(Deltares, 2022). P_{floc} is the fraction to form floc.

After the flocculated percentage is calculated, a settling velocity is needed for these clay flocculants. This settling velocity w_s can be calculated using the same subroutine in the 2017 Louisiana Coastal Master Plan using the following formulation (Eqn.31):

$$\begin{cases} w_s & C_{clay} < C_1 \\ a \frac{{C_{clay}}^n}{({C_{clay}}^2 + b^2)^m} & C_1 < C_{clay} < C_3 \\ negligible & C_2 < C_{clay} \end{cases} \qquad \text{Eqn.31}$$

Calculating the depositional velocity of cohesive sediments $V_{d,k}$ using Krone, (1962). The following equation is used (Eqn.32):

$$V_{d,k} = w_{sk}(1 - \frac{\tau_b}{\tau_{d,k}}) \qquad \text{Eqn.32}$$

Where w_{sk} is the settling velocity, $\tau_{d,k}$ is the critical depositional velocity.

Based on Lake Pontchartrain's fetch map see Appendix B, the model is set up as one cell with a constant depth and different fetch cases (CPRA, 2012; CPRA, 2017). This cell requires depth, fetch, and wind speed to estimate hydrodynamic forcing on the bed material. Setting up the model in Python as the computational language. The critical shear stress relationship was added to vary

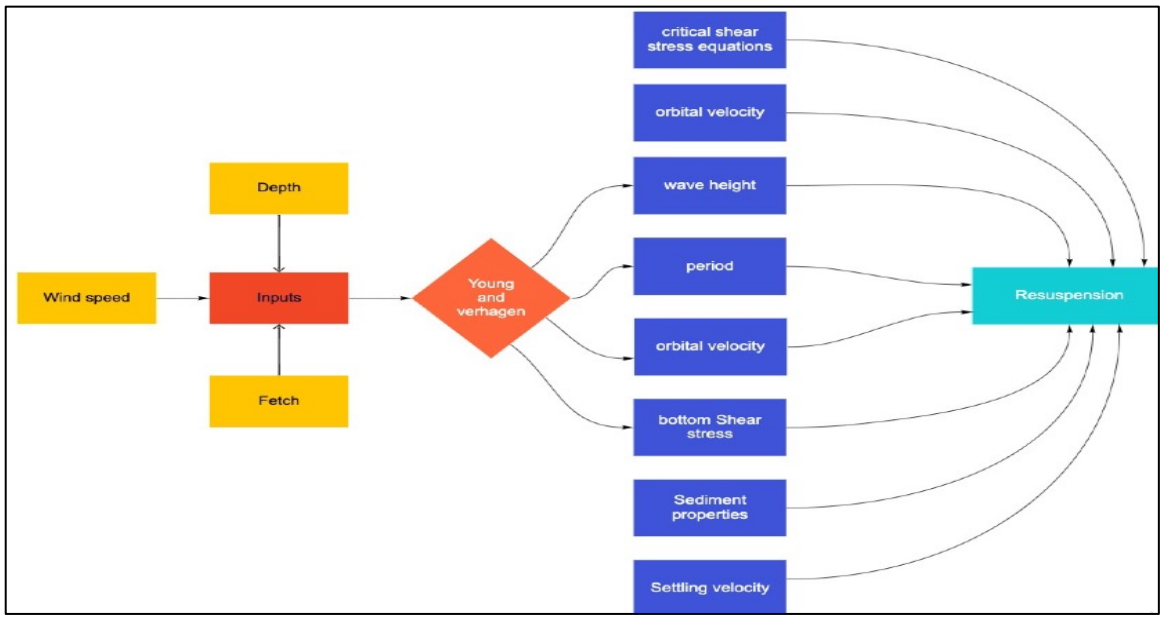

Figure 7-3 Sediment resuspension in open water model flow chart showing inputs and variables, and equations which produce a sediment resuspension value.

the critical shear stress or erosion based on laboratory testing. However, a clip function to this critical shear for erosion formulation so that the value of critical shear does not exceed the max critical shear observed in the current Shaker experiment. Figure 7.3 shows a flow chart of the required parameters for estimating resuspension.

7.2 Programming

The current programming language used is Python the computational environment is PyCharm. The main reason for selecting Python is the graphical abilities and speed at which data analysis can take place. For example, the Previous version of the current model was conducted in Fortran, and then the data had to be exported into excel. After that, charts, graphs, and model output can be plotted and analyzed. This is a cumbersome process uneconomical and could generate data assimilation errors. Therefore, Matplotlib is utilized in the current model, allowing instant graphical output to eliminate valuable time from the data analysis procedure (J. D. Hunter, 2007). Moreover, The ICM is much larger and captures a wide range of processes making it

computationally demanding to answer research questions. Hence, a simpler Python model will allow research questions to be answered efficiently.

7.3 Model testing and validation

The main objective of the numerical modeling of sediment transport is to demonstrate the application of the experimental results in a field situation. The model was initially tested using wind Speed data for 350 days was from USGS 07381340 Caillou Lake (Sister Lake) SW of Dulac, LA. The wind speed was converted from mile/hour to meter/sec, and the wind direction was degree clockwise from true north. All inputs are converted to a .csv file and imported into PyCharm. PyCharm is an Integrated Development Environment where the model can be executed.

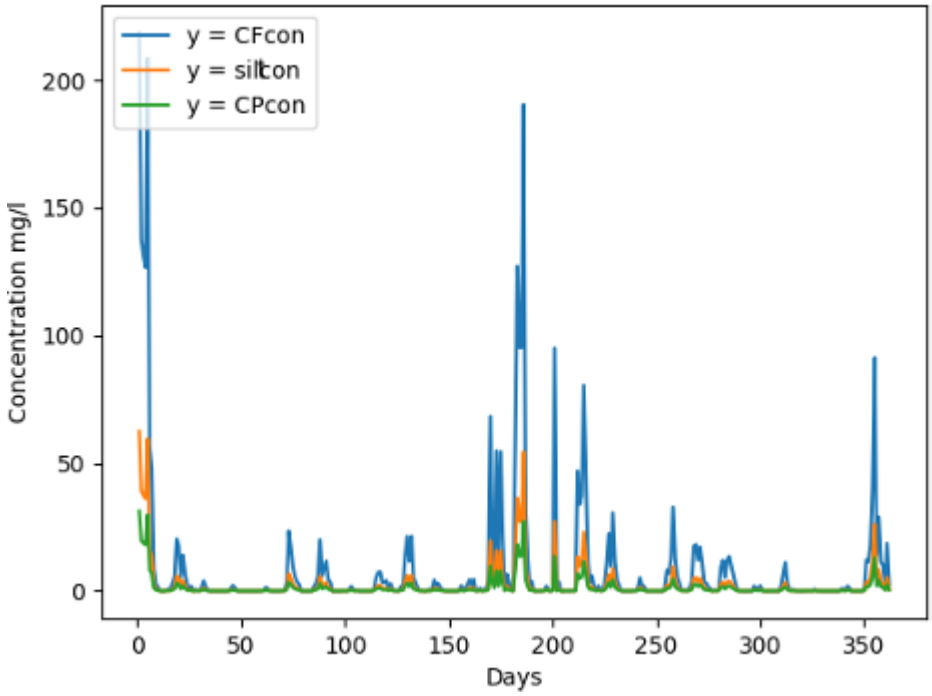

Figure 7-4 The time series plot of concentration of clay floc (CFcon), Silt (Siltcon), and Clay particulate (CPcon). τc=0.1 [Pa] and water depth of four meters.

It was observed that adding a critical shear stress relationship based on current experiments as opposed to using a fixed critical shear stress value of erosion tends to overestimate the resuspension. Figure 7-4 shows the resuspension of clay floc, silts, and clay particulate when using a fixed critical shear stress of erosion. Figure 7-5 shows the resuspension behavior when using a time varying critical shear stress. It is noticeable that the resuspension is reduced because a changing critical shear stress for erosion is used. These results could be interpreted that using

varying shear stress is more likely to mimic the natural environment where cycles and erosion, and deposition happen. Moreover, as seen earlier in figure 4-8, the value of the critical shear stress for erosion varies with settling time, so it is assumed that a fixed critical shear stress of erosion is not an accurate representation of field conditions. For the resuspension rate $g/m^2/s$ the same observation was made. If a time varying critical shear stress equation is used the resuspension rate is decreases.

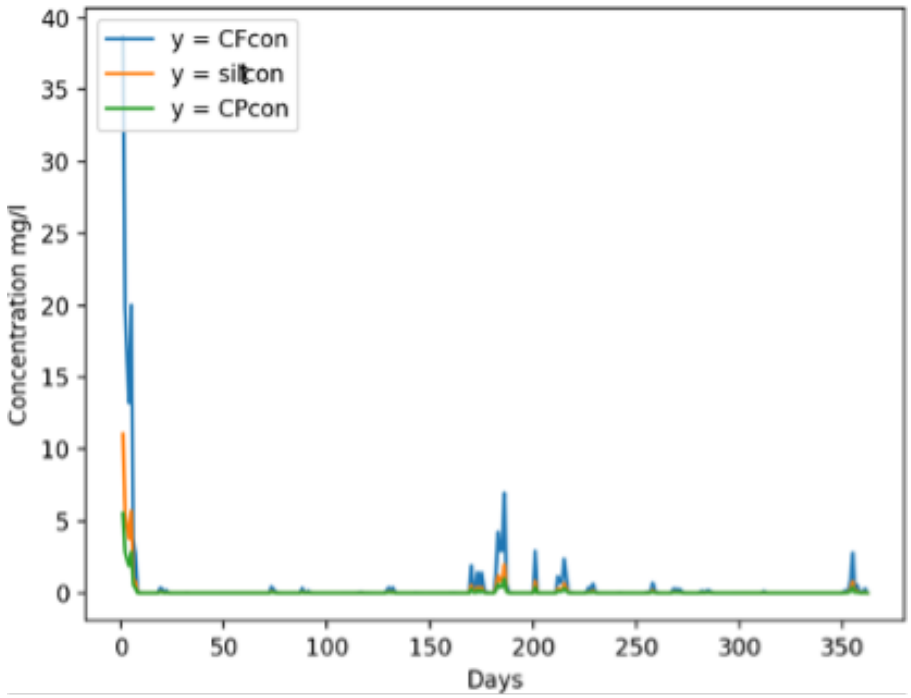

Figure 7-5 The time series plot of concentration of clay floc (CFcon), Silt (Siltcon), and Clay particulate (CPcon). Tc [Pa] = 0.0075(Days)+0.159 and water depth of four meters.

7.4 Model outputs

The wind speed record is in Appendix B used to generate these outputs. This record is from the New Orleans Lakefront Airport between 1990 and 2007. Figure 7-6 shows the concentration increase for the different sediment classes. The simulation was conducted using τc of 0.1 N/m^2 and depth of three meters. Using the same wind conditions and calibration parameters, see

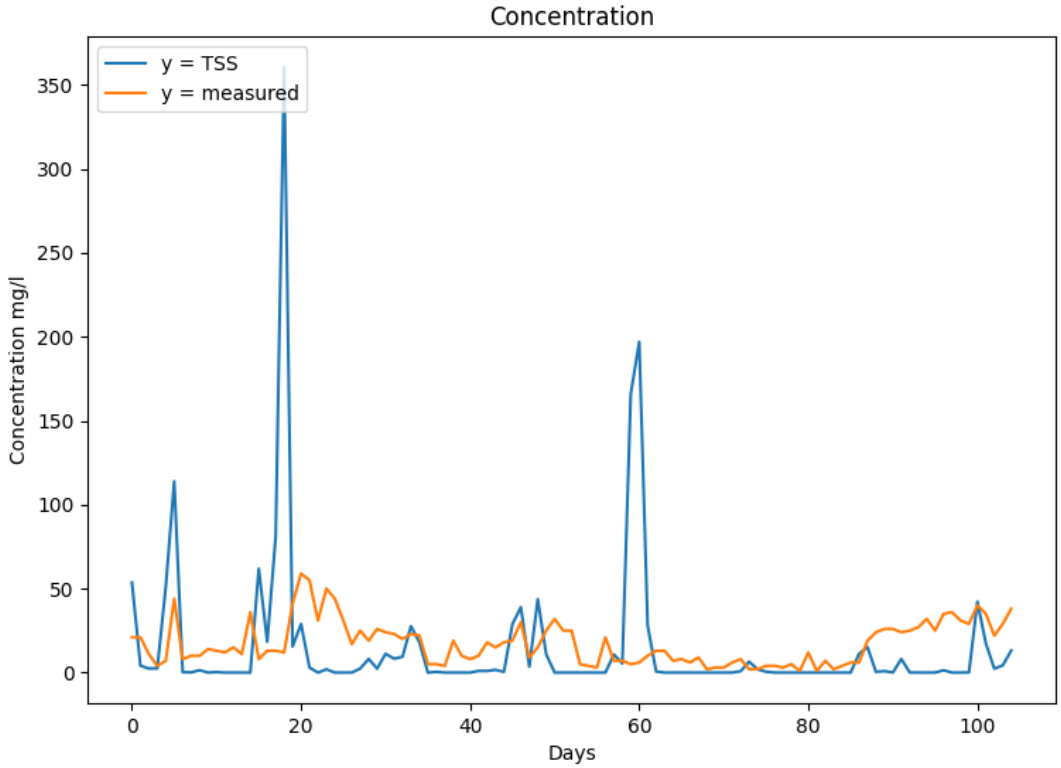

Figure 7-6 Show the total suspended solids concentration TSS [mg/l] output of the model compared to the observation. The mean bias error was 2.47 [mg/l]. Water depth used is three [meters].

Appendix B for all preset parameters. Figures 7-7, 7-8, and 7-9 have concentration decreased in all three constituents concentrations [mg/l] as the depth of simulations increased. Figures 7-10, 7-11, and 7-12 show that the suspended sediment concentration decreases when a varying shear stress formulation is introduced. Note that the shear stress formulation used in the simulation is derived in section 6.5. Moreover, this concentration decrease occurs over all the different depths examined. The summary for mean concentration for all the simulations are in Appendix B.

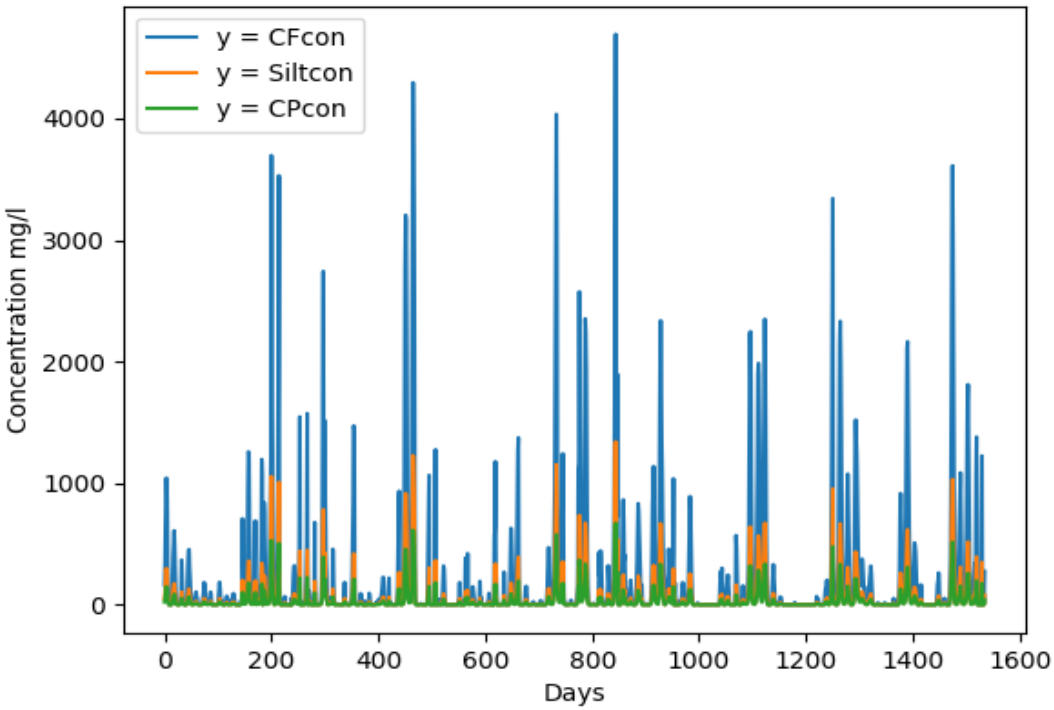

Figure 7-7 Times series of the concentrations simulated by the model corresponding to the value of shear stress $\tau c = 0.1$ [Pa] and one meter depth. Cfcon, is the clay floc concentration [mg/l], Siltcon is the silt concentration in [mg/l], and CPcon is clay particulate concentration [mg/l].

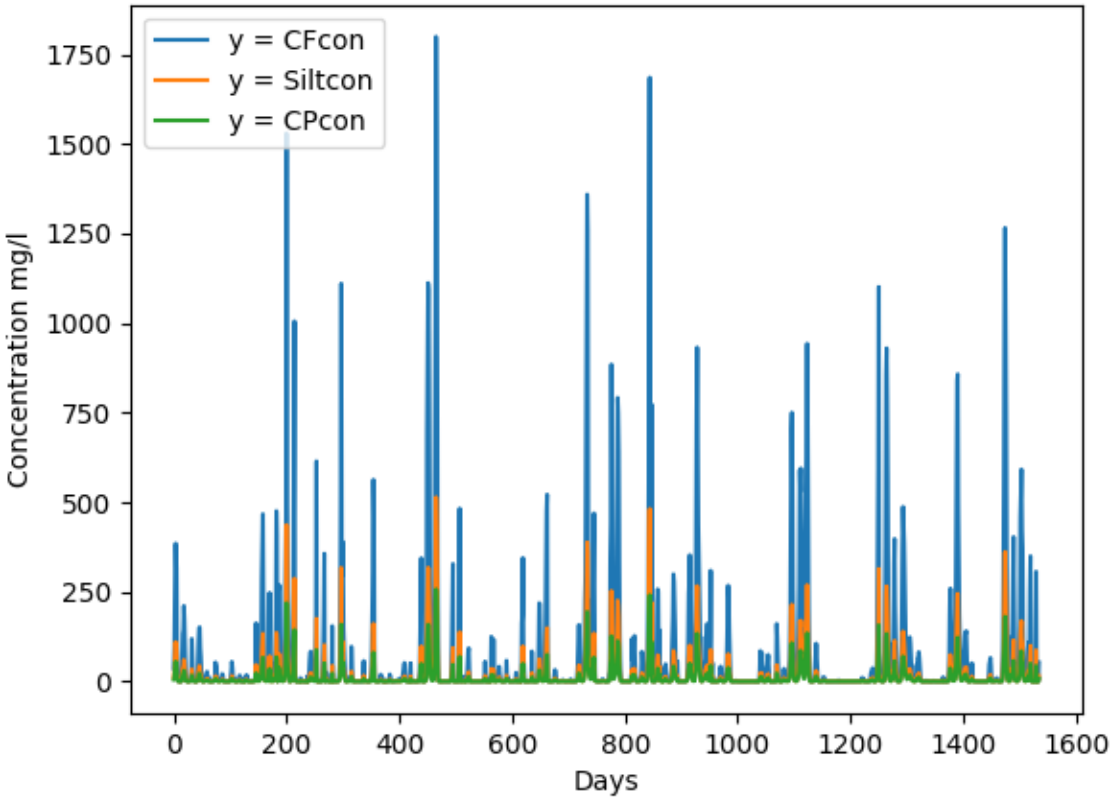

Figure 7-8 Times series of the concentrations simulated by the model corresponding to the value of shear stress τc 0.1 [Pa] and two-meter depth. Cfcon, is the clay floc concentration [mg/l], Siltcon is the silt concentration in [mg/l], and CPcon is clay particulate concentration [mg/l].

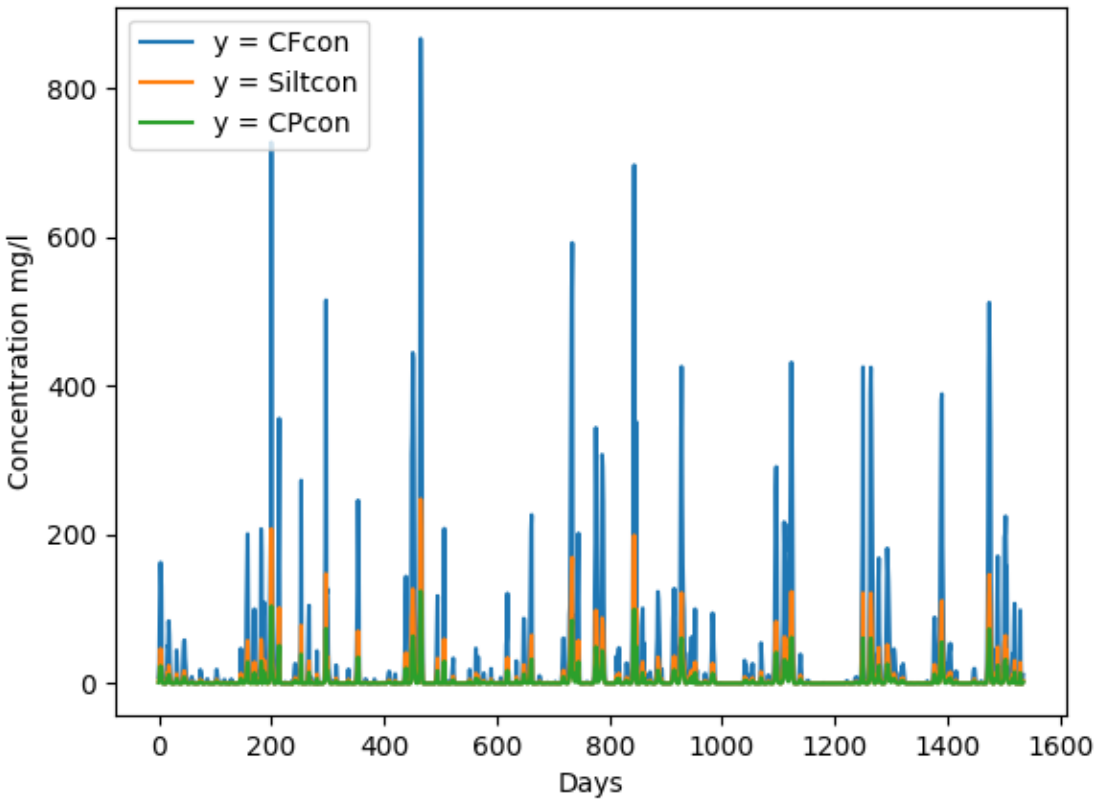

Figure 7-9 Times series of the concentrations simulated by the model corresponding to the value of shear stress τc 0.1 [Pa] and three-meter depth. Cfcon, is the clay floc concentration [mg/l], Siltcon is the silt concentration in [mg/l], and CPcon is clay particulate concentration [mg/l].

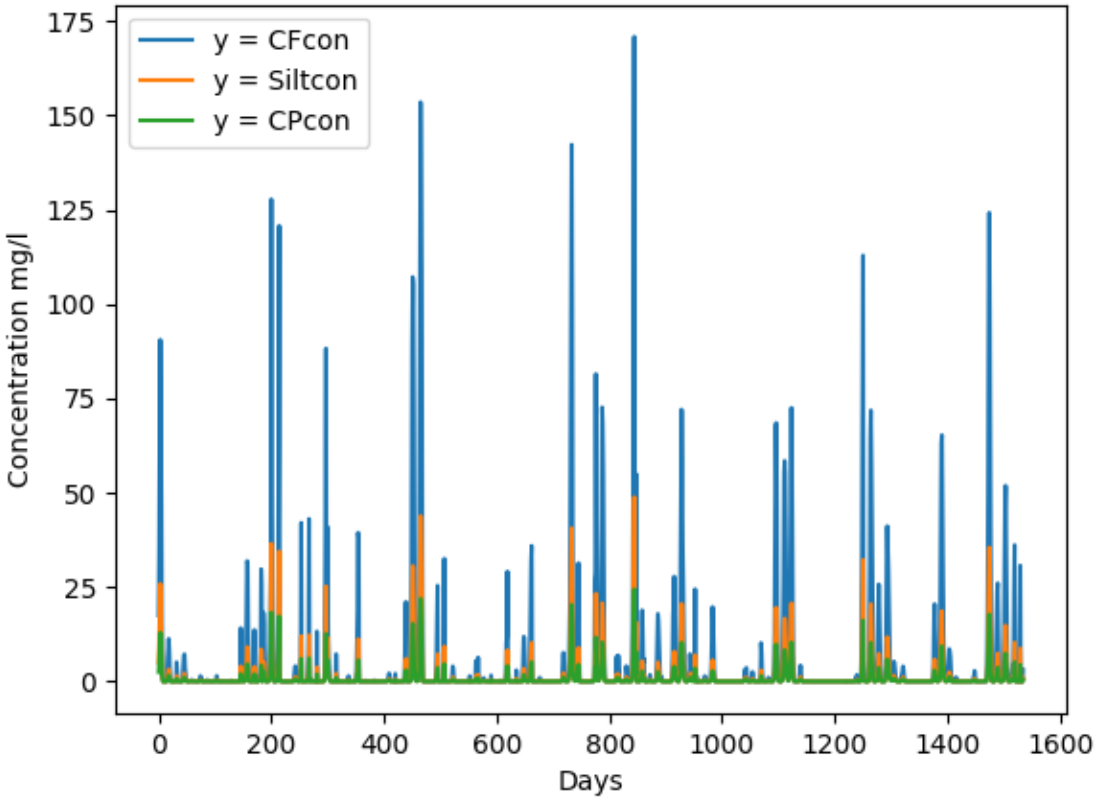

Figure 7-10 Times series of the concentrations simulated by the model corresponding to the value of shear stress [Pa] $\tau c = 0.008 * day + 0.1562$ and One-meter depth. Cfcon, is the clay floc concentration [mg/l], Siltcon is the silt concentration in [mg/l], and CPcon is clay particulate concentration [mg/l].

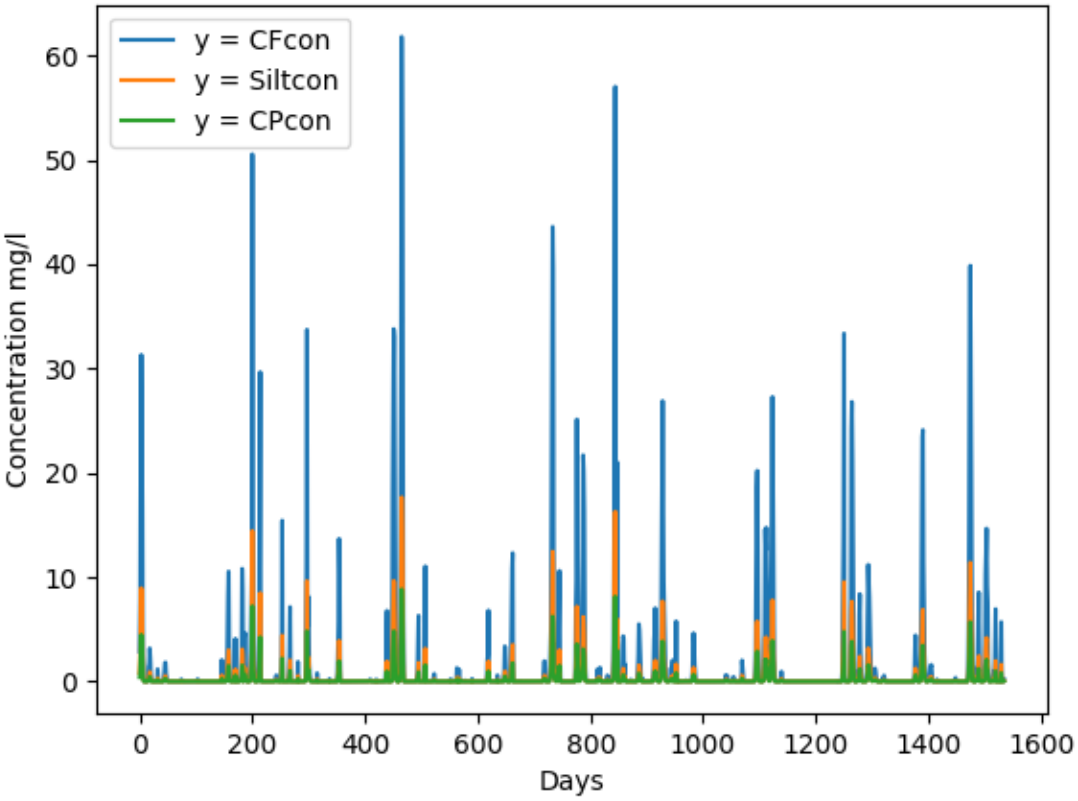

Figure 7-11 Times series of the concentrations simulated by the model corresponding to the value of shear stress [Pa] $\tau c = 0.008 * day + 0.1562$ and two-meter depth. Cfcon, is the clay floc concentration [mg/l], Siltcon is the silt concentration in [mg/l], and CPcon is clay particulate concentration [mg/l].

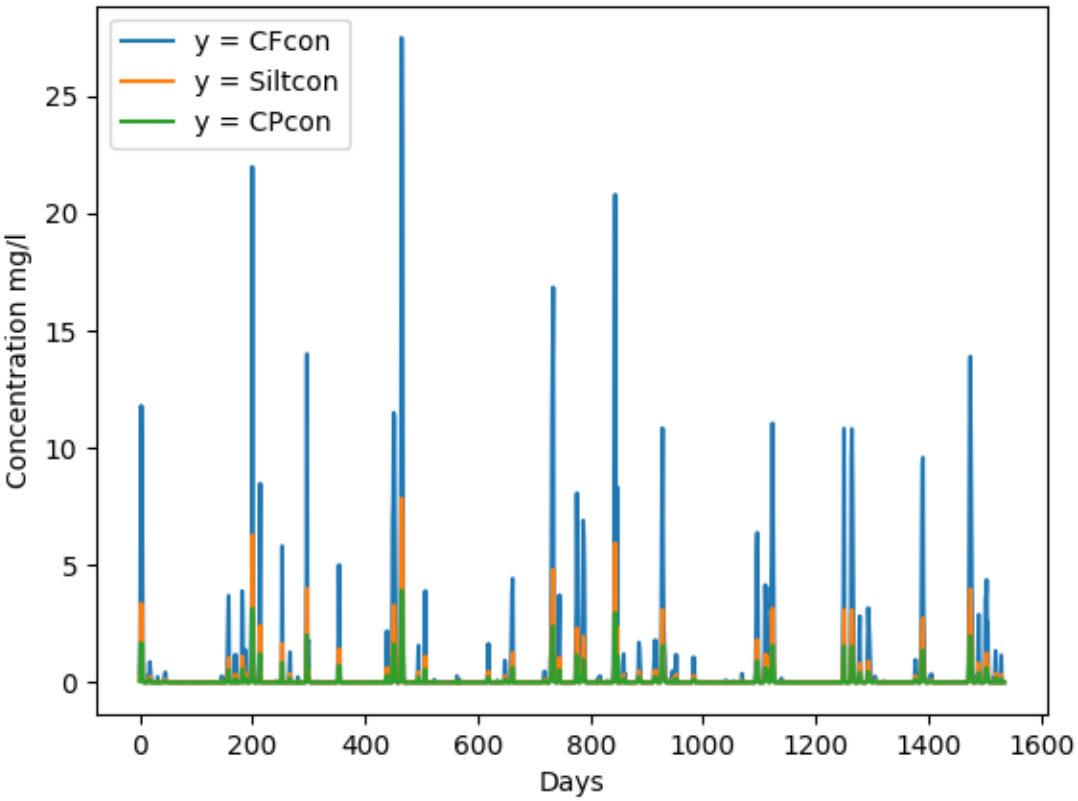

Figure 7-12 Times series of the concentrations simulated by the model corresponding to the value of shear stress [Pa] $\tau c = 0.008 * day + 0.1562$ and three-meter depth. Cfcon, is the clay floc concentration [mg/l], Siltcon is the silt concentration in [mg/l], and CPcon is clay particulate concentration [mg/l].

7.5 Marsh platform accretion Introduction:

Marsh is a type of wetland which frequently inundated with water. The location of a marsh is usually in the upper coastal intertidal zone between land and brackish water. The two main types of marsh are tidal and nontidal. In a nontidal region, the presence of salt will yield a nontidal brackish marsh with black needle-rush vegetation, and if no salt is present, then a fringe swamp forest with gum and cypress may be present. In tidal environments, the presence of salt will lead to a freshwater tidal swamp, and the absence of salt leads to cordgrass in the upper intertidal zone. These marshes provide a buffer zone from storms by attenuating wave energy. They also provide numerous habitats for fish, birds, and wildlife. The rich biodiversity supports the commercial fishing of shrimps and crabs, which supports many local communities trading these commodities. More recently, marshes are getting the recognition they deserve in combating climate change by blue carbon sequestration. Salt marsh has been shown to have an annual sequestration rate of 8 tones/year/hectare, around eight times more than tropical forests. Most of the captured carbon is stockpiled underground through marsh vegetation and extensive root systems in the form of soil organic matter (SOM). Villa & Bernal (2018) showed that in many marsh types, an increase in accretion rates corresponds to an increase in carbon sequestration rates. Therefore, it is vital to protect these wetlands. The Mississippi delta is very efficient in carbon capture (Wang et al., 2019). This sequestration is mainly done below ground by the remains of organic biomass, which get locked in the roots of various vegetation types.

Another implication of this marsh platform accretion model to be presented in section 7.6 is sediment trapping in the marsh platform during marsh inundation. Therefore, a marsh accretion rate will be estimated based on elevated meteorological conditions. The accretion rate will be calculated using the concentrations simulated by the accretion model multiplied by the settling velocity of sediments typical to this area. This deposition will be summed over the marsh inundation period to give an accretion rate. For example, the current marsh platform simulation produced an accretion rate for hurricane Issac in 2012 of 22464 g/m^2.

7.6 Accretion model formulation:

After calculating the resuspension concentration using the resuspension model, the next step is an attempt to determine the accretion rate for a given marsh edge. Main equations driving the processes are the sediment mass balance in the CPRA (2017), see (Eqn.20). For flow into the marsh in (m^3d^{-1}) the following equation is used Eqn.33 (Kadlec & Knight, 1996):

$$Q_{marsh=(a\times10^7)(W)(H)^3\left(\frac{\eta_{ow}-\eta_m}{L}\right)} \quad Eqn.33$$

Where a is a calibration coefficient $m^{-1}d^{-1}$, w is with of flow path (m), H marsh water depth (m), and η_{ow} Is the stage elevation in open water (m), and $\eta_m$stage elevation in marsh (m). L is the

distance between stage locations in (m). Note that all the units were converted to US for the current simulation.

7.7 Marsh accretion simulations

For the location of the marsh platform accretion simulation the boundary of The Coastwide Refence Monitoring System (CRMS 4245) station was selected Appendix B contains the full USGS map, and relevant information for the station. This station has some accretion rate measurements of about 20.1 mm (0.78 inches) per year between 2019 and 2020. The accretion model was run for the previously mentioned wind record for the selected area and did not affect the initial marsh platform elevation.

To Inundate the marsh, another simulation was performed using wind record and water elevations from New Canal Station, LA - Station ID: 8761927 are shown in Appendix B. The Period selected was during Hurricane Isaac landfall from August 27, 2017, to August 31, 2012. Figure 7-15 shows bed shear stress generated by the model. Figure 7-16 shows the TSS concentrations [mg/l] resulting from hurricane-force winds. Figure 7-17 shows the marsh platform deposition rate using the model shown in Appendix B. This accretion model is a simplified model using sediment mass balance (Eqn.20), and (Eqn.33) which is applied to the areas shown in figures 7-13 and 7-14. This model has yet to be validated as it is extremely difficult to obtain TSS concentration measurements during hurricane-force winds. It should be noted that the are physical limitations on the maximum concentration. For example, it cannot exceed the concentration of a packed bed. Furthermore, the receding concentration in Lake Pontchartrain normally takes about 24 hours to drop. The integration of the depositional rate curve in Figure 7.17 yields the sediment accretion for this event. An accretion of 22464 g/m^2 was obtained for this event.

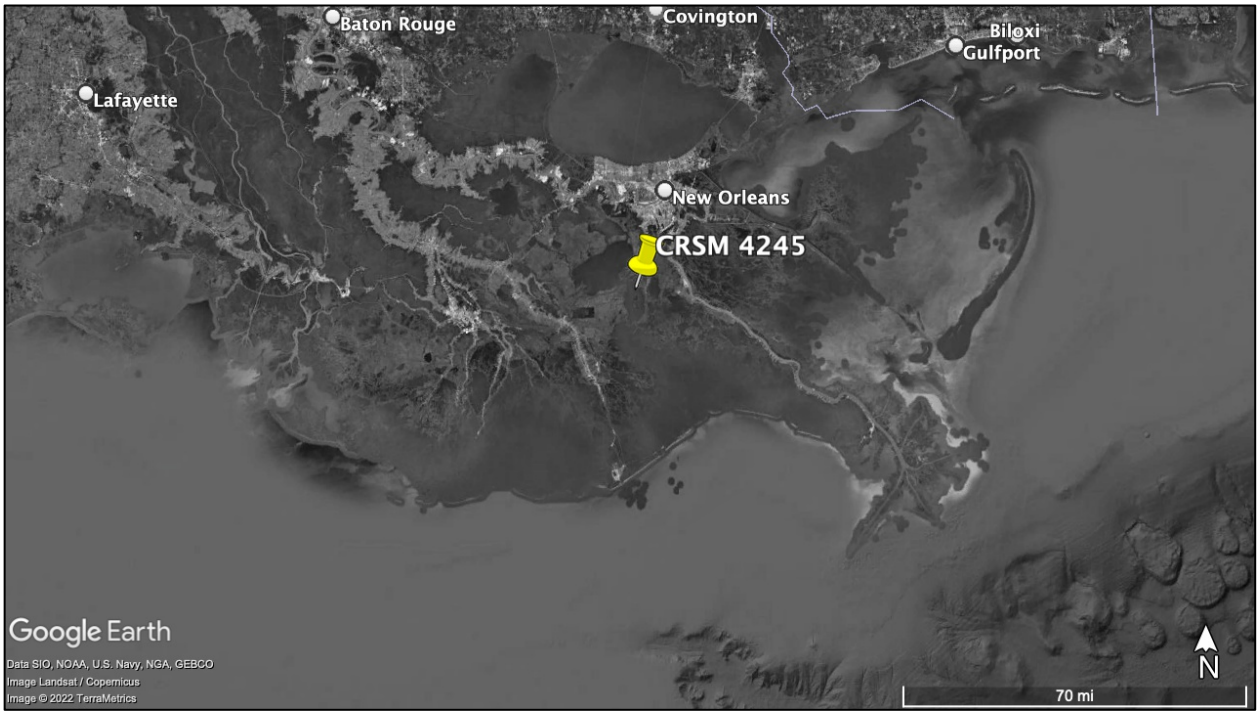

Figure 7-13 Location of the Coastwide Reference Monitoring System (CRMS 4245) station used in simulation The yellow pin represents the Station Location

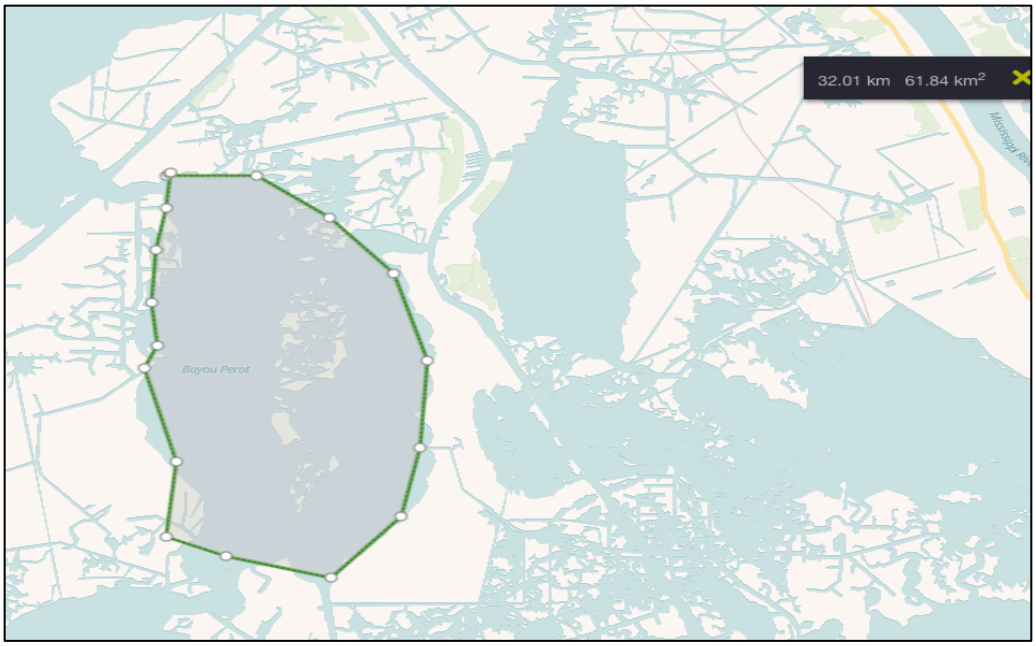

Figure 7-14 Size and location of the area selected to the application of marsh accretion simulation

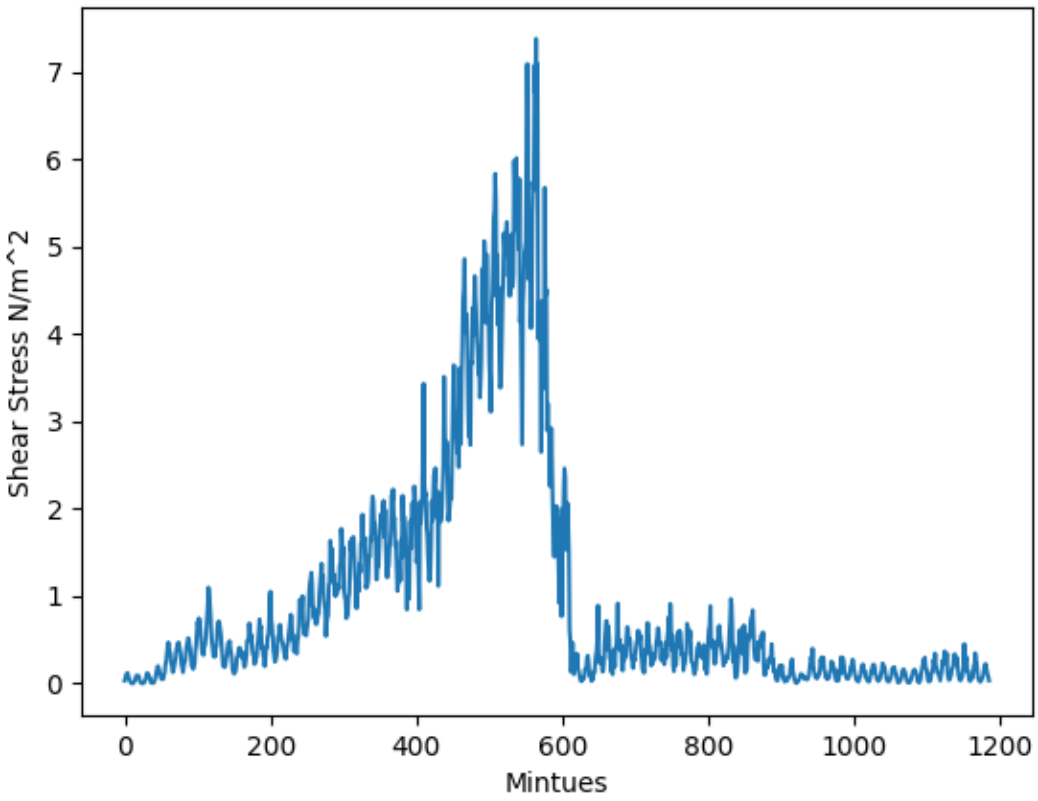

Figure 7-15 Bed shear stress [Pa] simulated by the model during Hurricane Isaac. The y-axis represents the model calculated bed shear stress [Pa] in response to the wind record from Station 8761927 From August 27, 2017, to August 31, 2012.

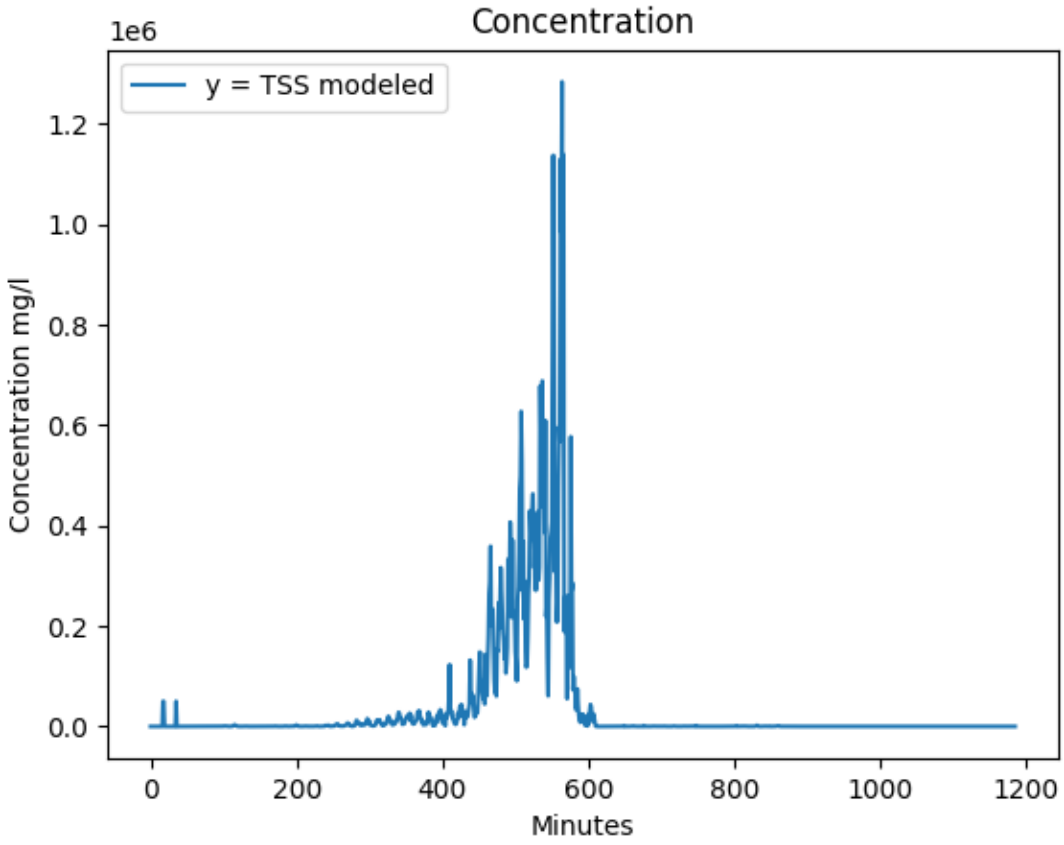

Figure 7-16 TSS concentration [mg/l] simulated by the model during Hurricane Isaac. The y-axis represents the model calculated TSS in [mg/l] corresponding to the wind record from Station 8761927 From August 27, 2017, to August 31, 2012.

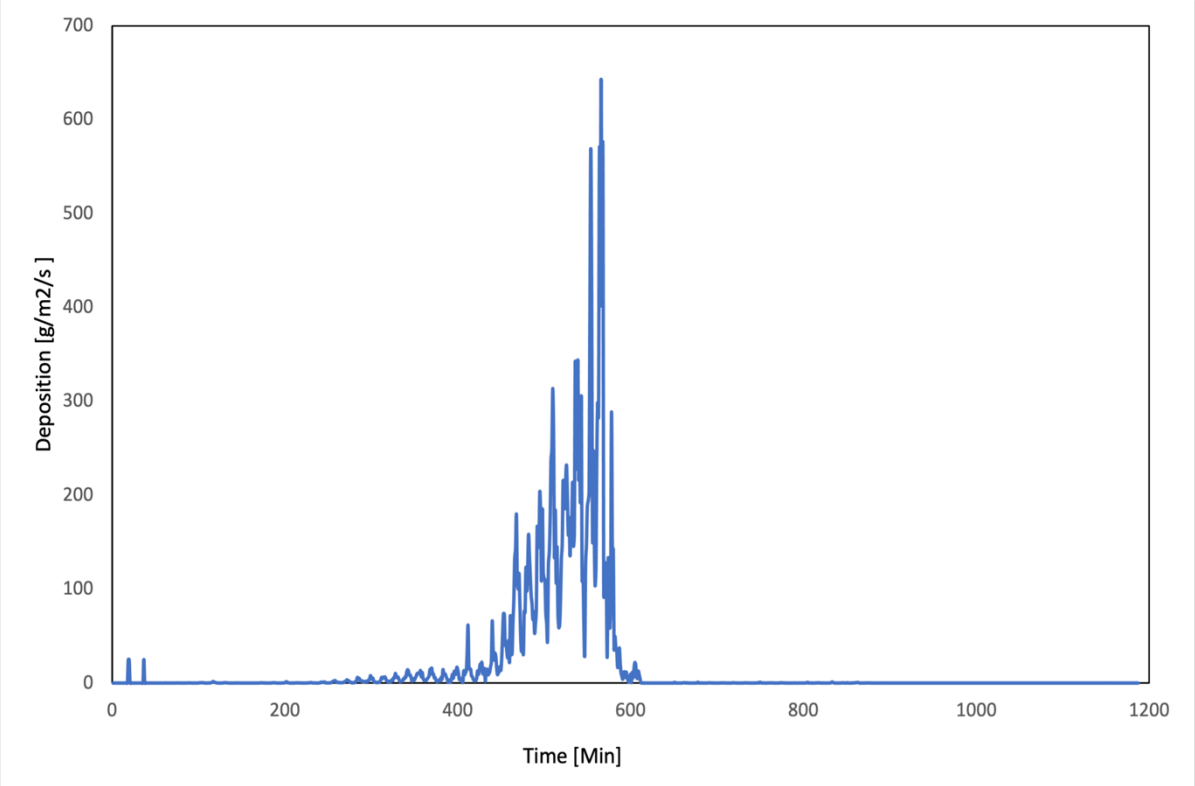

Figure 7-17 The deposition [g/m^2/s] rate for the simulated period for Hurricane Isaac. corresponding to the wind record from Station 8761927 From August 27, 2017, to August 31, 2012.

Chapter 8 Discussion

Soil strength measurement is often used in engineering design. However, laboratory strength is only sometimes an accurate measure of field strength. For example, the sampling technique, the calibration of testing equipment, and the rate of applied stresses during a strength test could change the strength measurement. Therefore, engineers must always rely on their experience and judgment when selecting laboratory testing procedures.

The current study is one of the ways the strength of low-strength sediment can be measured. Other erosion-measuring devices are summarized in the literature review chapter. Comparing the results of the current shaker experiments to previously conducted experiments that use different devices would be imprecise because, for example, the shaker applies stresses that are very different from the flume-applied shear stresses. Nevertheless, a comparison to previous erosion tests is beneficial to the current effort. For example, Gibbs (1962) conducted flume tests on clay and silts and predicted that critical shear stress was 0.7 Pa to 2.87 Pa with an average plasticity index of 16. In the current experiment, critical shear stress values are 0.065 Pa to 0.215 Pa and average plasticity index of 20. This lower critical shear stress value can be attributed to the fact that the surface erosion was examined, lowering the range of critical shear stresses.

Moreover, Lyle and Smerdon (1965) performed flume tests on silty clay loam, black clay, and Lake Charles clay, finding a power relationship to the plasticity index. A similar relationship was also established in the current shaker tests. Establishing a similar power relationship with to Lyle and Smerdon indicates that plasticity is potentially an important erosion parameter irrespective of the erosion testing device. An observation of model outputs shows that using a varying critical shear strength relationship as a model input rather than a fixed critical shear strength reduces the resuspension quantity at one, two, and three-meters depth. The mean TSS concentration (mg/l) produced by the model for one meter depth is 332 (mg/l) for a fixed τc of 0.1 Pa. On the other hand, the mean TSS concentration is 7.88 (mg/l) using $\tau c\ [Pa] = 0.008 * day + 0.1562$. However, this initial observation might translate into something other than other resuspension models and may be related to the currently used model. However, since the shear strength is the primary input, this relation should be examined in further resuspension studies and using different models.

The current study's self-weight settling time varied from one day to 12 days. This causes the sediment to consolidate slightly, specifically the surface layer, as the soil particles settle inside the water column. However, the deeper layers are not truly consolidated because, by definition, these sediments are saturated, and the void spaces contain incompressible water. Therefore, water must drain from the pore spaces for these sediments to truly consolidate and gain an increase in particle friction. Nevertheless, these sediments did gain some strength as part of the initial slight consolidation and perhaps due to biological activities inside the soil water column.

In the current study, the sample withdrawn from the shaker was replaced with site water rather than tap water. This has important implications for resuspension. For example, Fukuda & Lick (1980) showed that increasing the ionic strength of water by using tap water increases the degree of flocculation of the suspended sediments. It should also be noted that the locations sampled contained, on average, an organic content of four percent. The presence of organic could influence the erosion processes by, for example, clogging pore space and decreasing the permeability of the soil (Briaud et al., 2019). Moreover, early studies have shown that the presence of benthic organisms that secrete chemicals can reduce erosion by enhancing sedimentary cohesion (Ravens & Gschwend, 1999). More recently, Pant (2013) found reinforcing effects of fine soils and through attachment to the roots using electron microscope images and CSM tests.

The marsh edge simulation produced an accretion rate for hurricane Issac in 2012 of 22464 g/m^2, Tweel & Turner (2012) estimated 74600 g/m^2 for hurricane Gustav in 2005. As mentioned earlier, validating the marsh accretion model is challenging, as field TSS measurements need to be obtained during hurricane-force winds. In addition, the wind record could contain measurement errors, as censors may fail during these events. The current model is simplified, and only accounts for the effect of the waves in a shallow environment.

Other sources of uncertainty in the present study could come from the TSS measurements which were used. For instance, the fundamental difference between SCC and TSS methods is that the TSS uses part of the sample withdrawn, and CSS uses the entire sample. Moreover, Glysson and Gray (2002) examined 14,466 paired SSC and TSS samples and showed that the range of errors in TSS measurements is 40%. The accuracy of these measurements is vital to how critical shear stress values are derived from suspended sediment concertation values. Hence, it is recommended that future studies use SCC (ASTM, 1999) method for concentration measurements

Chapter 9 Conclusions

- The study primary purpose is measuring the erosion potential of cohesive sediments using the lick shaker. However, the shaker's shear stresses, and flow conditions were unknown, so the shaker was modeled in 2-D using Ansys providing flow conditions inside the water column.
- The tests conducted show two types of erosion surface and mass hence two critical shear stresses are identified. Furthermore,
- Good relationship was shown between the average critical shear stress and settling time exists for selected settling times.
- On the plasticity index and mass critical shear, the soils tested showed a moderate relationship. The plasticity index is widely used by soil engineering to classify soils strength and compressibility, so this should allow erosion potential criteria to be more approachable to soil engineers.
- A classification is proposed for erosion parameter *(m)* and varying with salinity. In a case the soil index properties are similar the relationship can be used.
- For sediments resuspension numerical modeling, with the new addition of a time-dependent critical shear stress formulation based on experimental data. This also the critical shear stress to varied with time. The critical shear is the main driver of sediment resuspension in all transport models. Theoretically without exceeding the shear strength there is no resuspension and subsequent transport.
- If anyone plans to use the critical shear for mass and surface, and the calibration coefficients (*m*) parameters, they must know that these relationships are site-specific and soil specific.
- The maximum bed shear stress produced by the Lick shaker was 0.6 Pa. However, shear stresses shown by (Howes et al. 2010) are between 425 Pa and 3600 Pa during storm conditions. Hence, one must exercise caution using these results to model massive transport phenomena. The current model produced a maximum bed shear of 7.1 Pa for Hurricane Isaac simulation.

Chapter 10 Recommendations For Future Work

- The current shaker experiment reached 12 days of settling time. Future tests should extend past 12 days to examine the behavior of the shear strength for longer settling times.
- Using a parallel apparatus that constantly monitors and records concentrations in the water column will eliminate having to disturb the grid while withdrawing sub-samples and decrease the cost of obtaining more site water since no water will need to be withdrawn. An example of such an apparatus is the Optical backscatter (OBS). The particle size range for best operation is 200-400 μm. Concentrations may range up to 100 g/L.
- Integrating an opening into the water bath column where sediments are placed could ensure that sampling is always conducted at the exact location.
- Expand the Ansys Shaker model to 3D and include sediments. This will further improve the Shaker simulations.
- The salinity and resuspension relationship should be examined further. The results in section 4.2 show that the resuspension behavior changes primarily decrease with salinity increases. However, more tests are needed to confirm this behavior.
- There was an attempt to approximate the thickness of the layer resuspended after or during each Shaker test. However, this could not be complete because the water becomes highly turbid, and the layer can be seen clearly. If further studies can somehow quantify this layer, this would address some weaknesses of using the Shaker compared to Flume experiments.
- The accuracy of these TSS measurements is significant to how critical shear stress values are derived from suspended sediment concertation values. Hence, it is recommended that future studies use SCC method (ASTM, 1999) for concentration measurements.

REFERENCES

Abdel-Rahman, N. M. (1963). *The Effect of Flowing Water on Cohesive Beds* [ETH Zurich]. https://doi.org/10.3929/ethz-a-000088475

Ansys. (2009). *Ansys Fluent Release 12.0 Theory Guide*.

Ansys. (2017). *Ansys Fluent Tutorial Guide Release 18*.

ASTM, 1999, Standard Test Method for Determining Sediment Concentration in Water Samples: American Society of Testing and Materials, D 3977-97, Vol. 11.02, pp. 389-394.

Ariathurai, C. R. (1974). *A Finite Element Model for Sediment Transport in Estuaries* [Ph.D. dissertation]. University of California, Davis.

Batchelor, G. K. (1967). *An introduction to fluid dynamics* (First Cambridge mathematical library edition). Cambridge University Press.

Baumann, R. H., & Turner, R. E. (1990). *Direct impacts of outer continental shelf activities on wetland loss in the central Gulf of Mexico*. 10.

Blum, M. D., & Roberts, H. H. (2012). The Mississippi Delta Region: Past, Present, and Future. *Annual Review of Earth and Planetary Sciences*, *40*(1), 655–683. https://doi.org/10.1146/annurev-earth-042711-105248

Booij, R. (1994). *Measurements of the Flow Field in a Rotating Annular Flume*.

Briaud, J.-L., Iman, S., Hamn, C. C., Medina-Cetina, & Zenon. (2019). *Relationship Between Erodibility and Properties of Soils*. The National Academies Press. https://doi.org/10.17226/25470

Briaud, J.-L., Ting, F., & Chen, H. C. (1990). *Sricos: Prediction of Scour Rate at Bridge Piers* (No. 2937–1). Texas A&M University.

CDC. (2013). *Deaths Associated with Hurricane Sandy*. Center for Disease Control. https://www.cdc.gov/mmwr/preview/mmwrhtml/mm6

Costanza, R., Pérez-Maqueo, O., Martinez, M. L., Sutton, P., Anderson, S. J., & Mulder, K. (2008). The Value of Coastal Wetlands for Hurricane Protection. *AMBIO: A Journal of the Human Environment*, *37*(4), 241–248. https://doi.org/10.1579/0044-7447(2008)37[241:TVOCWF]2.0.CO;2

Couvillion, B., Beck, H., Schoolmaster, D., & Fischer, M. (2016). *Land Area Change in Coastal Louisiana (1932 to 2016)*. USGS.

CPRA. (2007). *Louisiana's 2007 Comprehensive Master Plan for a Sustainable Coast and Appendices* (p. 170). https://cims.coastal.louisiana.gov/RecordDetail.aspx?Root=0&sid=670#

CPRA. (2012). *Louisiana's 2012 Comprehensive Master Plan for a Sustainable Coast and Appendices* (p. 171).

CPRA. (2017). *Louisiana's 2017 Comprehensive Master Plan for a Sustainable Coast and Appendices* (p. 171).

CWPPRA. (2012). *The 2012 Evaluation Report to the U.S. Congress on the Effectiveness of Coastal Wetlands Planning, Protection and Restoration Act Projects*.

De Roo, A. P. J., & Jetten, V. G. (1999). Calibrating and validating the LISEM model for two data sets from the Netherlands and South Africa. *CATENA*, *37*(3), 477–493. https://doi.org/10.1016/S0341-8162(99)00034-X

Deltares. (2022). *Delft 3D-flow Simulation of Multi-Dimensional Hydrodynamic Flows and Transport Phenomena, Including Sediments User Manual*.

DePinto, J. V., Lick, W. J., & Paul, J. F. (Eds.). (1994). *Transport and transformation of contaminants near the sediment-water interface*. Lewis Publishers.

ECOMSED. (2002). *ECOMSED Version 1.3 User Manual*.

Filostrat, J. E. (2014). *Estimation of Sediment Resuspension and Deposition in Coastal Waters* [MS Thesis]. University of New Orleans.

Flanagan, D. C., Ascough, J. C., Nearing, M. A., & Laflen, J. M. (2001). The Water Erosion Prediction Project (WEPP) Model. In R. S. Harmon & W. W. Doe (Eds.), *Landscape Erosion and Evolution Modeling* (pp. 145–199). Springer US. https://doi.org/10.1007/978-1-4615-0575-4_7

Fukuda, M. K., & Lick, W. (1980). The Entrainment of Cohesive Sediments in Freshwater. *Journal of Geophysical Research*, *85*(C5), 2813. https://doi.org/10.1029/JC085iC05p02813

Ghose-Hajra, M., McCorquodale, A., Mattson, G., Jerolleman, D., & Filostrat, J. (2015). Effects of salinity and particle concentration on sediment hydrodynamics and critical bed-shear-stress for erosion of fine grained sediments used in wetland restoration projects. *Proceedings of the International Association of Hydrological Sciences*, *367*, 435–441. https://doi.org/10.5194/piahs-367-435-2015

Gibbs, H. J. (1962). *A study of erosion and tractive force characteristics in relation to soil mechanics properties*. Office of Assistant Commissioner and Chief Engineer Division of Engineering Laboratories.

Glysson, G. D. (2002). *TOTAL SUSPENDED SOLIDS DATA FOR USE IN SEDIMENT STUDIES*. 3.

Gounder Krishnappan, B., Stone, M., Granger, S., Upadhayay, H., Tang, Q., Zhang, Y., & Collins, A. (2020). Experimental Investigation of Erosion Characteristics of Fine-Grained Cohesive Sediments. *Water*, *12*(5), 1511. https://doi.org/10.3390/w12051511

Haralampides, K. (2000). *A Study of the Hydrodynamics and Salinity Regimes of the Lake Pontchartrain System* [Ph.D. dissertation]. University of New Orleans.

Howes, N. C., FitzGerald, D. M., Hughes, Z. J., Georgiou, I. Y., Kulp, M. A., Miner, M. D., Smith, J. M., & Barras, J. A. (2010). Hurricane-induced failure of low salinity wetlands. *Proceedings of the National Academy of Sciences*, *107*(32), 14014–14019. https://doi.org/10.1073/pnas.0914582107

J. D. Hunter. (2007). Matplotlib: A 2D Graphics Environment. *Computing in Science & Engineering*, *9*(3), 90–95. https://doi.org/10.1109/MCSE.2007.55

Jepsen, R. A. (2006). Uncertainty in Experimental Techniques for Measuring Sediment Erodability: Uncertainty for Sediment Erodability. *Integrated Environmental Assessment and Management*, *2*(1), 39–43. https://doi.org/10.1002/ieam.5630020108

Jerolleman, D. (2014). *Non-Thesis Report Submitted to the Department of Civil Engineering, University of New Orleans; for Partial Fulfillment of the Master of Science Degree.*

Kadlec, R. H., & Knight, R. L. (1996). *Treatment wetlands*. Lewis Publishers.

Kawata, Y., & Tsuchiya, Y. (1987). Applicability of Sub-Sand System to Beach Erosion Control. *Coastal Engineering 1986*, 1255–1267. https://doi.org/10.1061/9780872626003.092

Kotylar, L. S., Sparks, B. D., & Schutte, R. (1996). Effect of Salt on the Flocculation Behavior of Nano Particles in Oil Sands Fine Tailings. *Clays and Clay Minerals*, *44*(1), 121–131. https://doi.org/10.1346/CCMN.1996.0440111

Krone, R. B. (1962). *Flume Studies of the Transport of Sediment in Estuarial Shoaling Processes; Final Report* (p. 129).

Larsen, R. (2008). *Erosion Function Apparatus*. 16.

Lavelle, J. W., & W R Davis. (n.d.). *Measurements of benthic sediment erodibility in Puget Sound, Washington*. 36.

Mahmoodabadi, M., Ghadiri, H., Rose, C., Yu, B., Rafahi, H., & Rouhipour, H. (2014). Evaluation of GUEST and WEPP with a new approach for the determination of sediment transport capacity. *Journal of Hydrology*, *513*, 413–421. https://doi.org/10.1016/j.jhydrol.2014.03.060

Mattson, G. (2014). *Characterization of Dredged Sediment Used in Coastal Restoration and Marsh Creation Projects* [MS Thesis]. University of New Orleans.

McNeil, J., Taylor, C., & Lick, W. (1996). Measurements of Erosion of Undisturbed Bottom Sediments with Depth. *Journal of Hydraulic Engineering*, *122*(6), 316–324. https://doi.org/10.1061/(ASCE)0733-9429(1996)122:6(316)

Mebust, C. M. (2015). *Analysis of Sedimentation Characteristics of Dredge Sediment Used in Coastal Restoration and Marsh Creation Projects* [MS Thesis]. University of New Orleans.

Mehta, A. J. (1973). *Depositional Behavior of Cohesive Sediments* [Ph.D. dissertation]. The University of Florida.

Mentaschi, L., Vousdoukas, M. I., Pekel, J.-F., Voukouvalas, E., & Feyen, L. (2018). Global Long-Term Observations of Coastal Erosion and Accretion. *Scientific Reports*, *8*(1), 12876. https://doi.org/10.1038/s41598-018-30904-w

Mingham, C. (2003). Chapter 3 Advanced Numerical Methods for Coastal Hydrodynamics. In V. C. Lakhan (Ed.), *Elsevier Oceanography Series* (Vol. 67, pp. 73–91). Elsevier. https://doi.org/10.1016/S0422-9894(03)80120-4

Mitchell, J. K., & Soga, K. (2005). *Fundamentals of Soil Behavior*.

Möller, I., Kudella, M., Rupprecht, F., Spencer, T., Paul, M., van Wesenbeeck, B. K., Wolters, G., Jensen, K., Bouma, T. J., Miranda-Lange, M., & Schimmels, S. (2014). Wave Attenuation Over Coastal Salt Marshes Under Storm Surge Conditions. *Nature Geoscience*, *7*(10), 727–731. https://doi.org/10.1038/ngeo2251

Narayan, S., Beck, M. W., Reguero, B. G., Losada, I. J., van Wesenbeeck, B., Pontee, N., Sanchirico, J. N., Ingram, J. C., Lange, G.-M., & Burks-Copes, K. A. (2016). The Effectiveness, Costs and Coastal Protection Benefits of Natural and Nature-Based Defences. *PLOS ONE*, *11*(5), e0154735. https://doi.org/10.1371/journal.pone.0154735

Pant, H. (2013). *Erosional resistance of cohesive sediments in coastal saltmarshes* [Master of Science in Civil Engineering, Louisiana State University and Agricultural and Mechanical College]. https://doi.org/10.31390/gradschool_theses.386

Partheniades, E. (1962). *A Study of Erosion and Deposition of Cohesive Soils in Salt Water* [Ph.D. dissertation]. University of California, Berkeley.

Partheniades, E. (2009). *Cohesive Sediments in Open Channels: Properties, Transport, and Applications*. Butterworth-Heinemann.

Phillips, O. M. (1977). *The dynamics of the upper ocean* (2. ed). Cambridge Univ. Pr.

Ravens, T. M., & Gschwend, P. M. (1999). Flume Measurements of Sediment Erodibility in Boston Harbor. *Journal of Hydraulic Engineering*, *125*(10), 998–1005. https://doi.org/10.1061/(ASCE)0733-9429(1999)125:10(998)

Rijn, L. C. van. (1993). *Principles of sediment transport in rivers, estuaries and coastal seas*. Aqua Publications.

RMS. (2021). *RMS Estimates US$31– $44 Billion in Total U.S. Onshore and Offshore Insured Losses from Hurricane Ida*. https://www.rms.com/newsroom/press-releases/press-detail/2021-09-16/rms-estimates-us31-44-billion-in-total-us-onshore-and-offshore-insured-losses-from-hurricane-ida

Roberts, B. (2022). *Effects of Organic Matter on Settling Velocity of Coastal Sediments Used in Coastal Restoration and Marsh Creation Projects* [MS Thesis]. University of New Orleans.

Roberts, H. H., DeLaune, R. D., White, J. R., Li, C., Sasser, C. E., Braud, D., Weeks, E., & Khalil, S. (2015). Floods and Cold Front Passages: Impacts on Coastal Marshes in a River Diversion Setting (Wax Lake Delta Area, Louisiana). *Journal of Coastal Research*, *315*, 1057–1068. https://doi.org/10.2112/JCOASTRES-D-14-00173.1

Rossby, C.-G., & Montgomery, R. B. (1935). *The layer of frictional influence in wind and ocean currents*. Massachusetts Institute of Technology and Woods Hole Oceanographic Institution. https://doi.org/10.1575/1912/1157

Shu, C., Tan, G., Chen, P., Wang, J., & Lv, P. (2020a). Experimental Study on Incipient Shear Stress of Consolidated Cohesive Sediment. *Arabian Journal of Geosciences*, *13*(18), 964. https://doi.org/10.1007/s12517-020-05978-4

Shu, C., Tan, G., Chen, P., Wang, J., & Lv, P. (2020b). Experimental study on incipient shear stress of consolidated cohesive sediment. *Arabian Journal of Geosciences*, *13*(18), 964. https://doi.org/10.1007/s12517-020-05978-4

Simons, M., Podger, G., & Cooke, R. (1996). IQQM—a Hydrologic Modelling Tool for Water Resource and Salinity Management. *Modelling and Simulation Theme: Regional Development and Environmental Change*, *11*(1), 185–192. https://doi.org/10.1016/S0266-9838(96)00019-6

Smerdon, E. T., & Beasley, R. P. (1959). *The Tractive Force Theory Applied to Stability of Open Channels in Cohesive Soils*. 36.

Smith, J. (2010). *Fine Sediments Dynamics in Dredge Plumes*. 130.

Tolhurst, T. J., Black, K. S., Shayler, S. A., Mather, S., Black, I., Baker, K., & Paterson, D. M. (1999). Measuring the in situ Erosion Shear Stress of Intertidal Sediments with the Cohesive Strength Meter (CSM). *Estuarine, Coastal and Shelf Science*, *49*(2), 281–294. https://doi.org/10.1006/ecss.1999.0512

Tweel, A. W., & Turner, R. E. (2012). Landscape-Scale Analysis of Wetland Sediment Deposition from Four Tropical Cyclone Events. *PLoS ONE*, *7*(11), e50528. https://doi.org/10.1371/journal.pone.0050528

Trammell, M. A. (2004). *Laboratory Apparatus and Methodology for Determining Water Erosion Rates of Erodible Rock and Cohesive Sediments* [MS Thesis]. University of Florida, Gainesville.

Tsai, C.-H., & Lick, W. (1986). A Portable Device for Measuring Sediment Resuspension. *Journal of Great Lakes Research*, *12*(4), 314–321. https://doi.org/10.1016/S0380-1330(86)71731-0

US Army Corps & of Engineers. (2011). *Coastal Engineering Manual—Part VI EM 1110-2-1100*. US Army Corps of Engineers.

Vermeyen, T. (1995). *Erosional and Depositional Characteristics of Cohesive Sediments Found in Elephant Butte Reservoir, New Mexico*. 40.

Villa, J. A., & Bernal, B. (2018). Carbon sequestration in wetlands, from science to practice: An overview of the biogeochemical process, measurement methods, and policy framework. *Wetlands and Carbon Revisited*, *114*, 115–128. https://doi.org/10.1016/j.ecoleng.2017.06.037

Vsilind, P. (1968). *A. Theoretical Considerations: Design of Prototype Thickeners from Batch Settling Tests*. Water and Sewage Works.

W. M. Lyle and E. T. Smerdon. (1965). Relation of Compaction and Other Soil Properties to Erosion Resistance of Soils. *Transactions of the ASAE*, *8*(3), 0419–0422. https://doi.org/10.13031/2013.40536

Wang, F., Lu, X., Sanders, C. J., & Tang, J. (2019). Tidal wetland resilience to sea level rise increases their carbon sequestration capacity in United States. *Nature Communications*, *10*(1), 5434. https://doi.org/10.1038/s41467-019-13294-z

Williams, R. S., Ferrigno, J. G., Swithinbank, C., Lucchitta, B. K., & Seekins, B. A. (1995). Coastal-change and glaciological maps of Antarctica. *Annals of Glaciology*, *21*, 284–290. https://doi.org/10.3189/S0260305500015950

Winterwerp, J. C., & Kesteren, W. G. M. van. (2004). *Introduction to the Physics of Cohesive Sediment in the Marine Environment*. Elsevier.

Yang, C. T. (2006). *Erosion and Sedimentation Manual*. U.S. Department of the Interior.

Young, I. R., & Verhagen, L. A. (1996). The growth of fetch limited waves in water of finite depth. Part 1. Total energy and peak frequency. *Coastal Engineering*, *29*(1), 47–78. https://doi.org/10.1016/S0378-3839(96)00006-3

Young, R. A., Onstad, C. A., Bosch, D. D., & Anderson, W. P. (1987). *AGNPS, Agricultural Non-Point-Source Pollution Model: A watershed analysis tool. Research report*. https://www.osti.gov/biblio/5563556

Appendix A

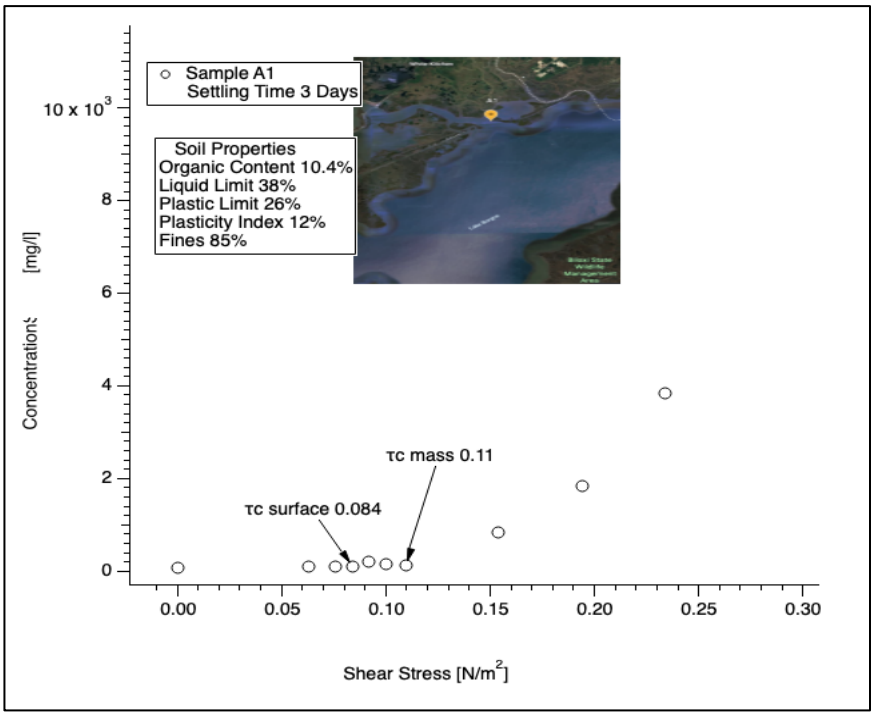

Figure 12-1 Concentrations inside the Shaker as a function of bottom shear stress. For sample A1 with 3 days of settling time τc shows the erosion critical shear stress for surface and mass erosion.

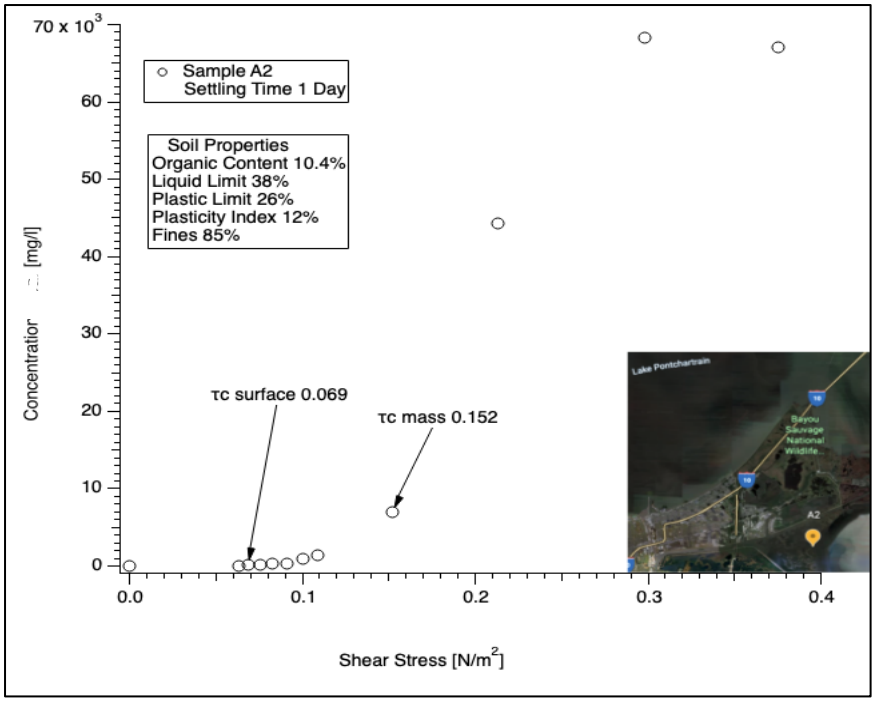

Figure 12-2 Concentrations inside the Shaker as a function of bottom shear stress. For sample A2 with 1 day of settling time τc shows the erosion critical shear stress for surface and mass erosion.

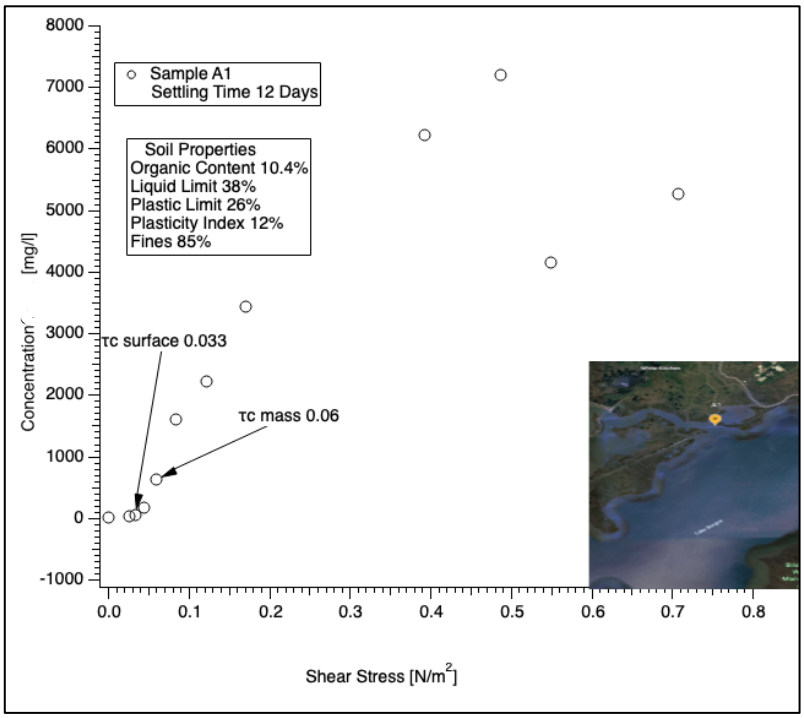

Figure 12-3 Concentrations inside the Shaker as a function of bottom shear stress. For sample A1 with 12 days of settling time τc shows the erosion critical shear stress for surface and mass erosion.

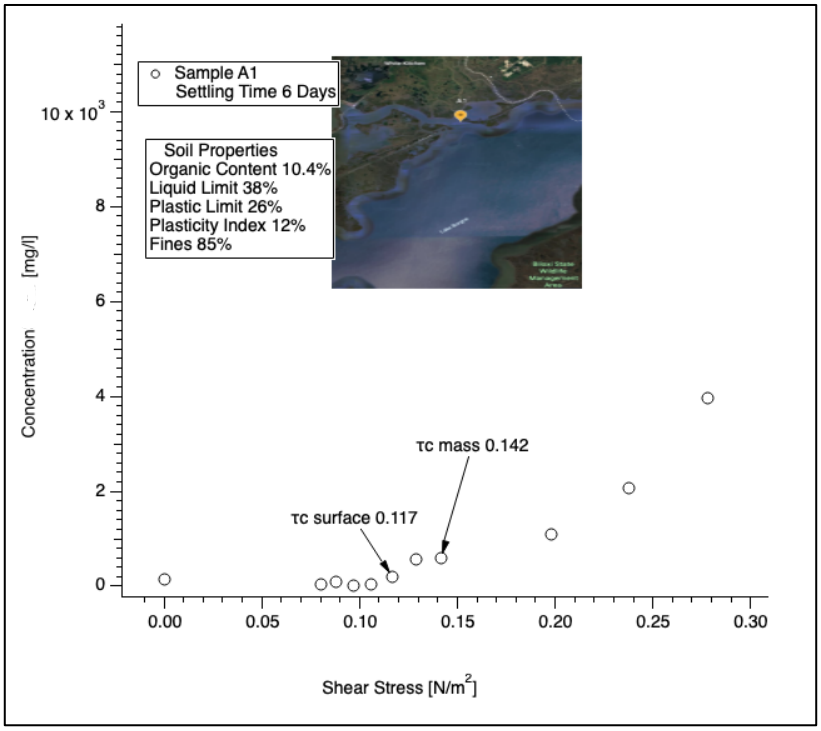

Figure 12-4 Concentrations inside the Shaker as a function of bottom shear stress. For sample A1 with 6 days of settling time τc shows the erosion critical shear stress for surface and mass erosion.

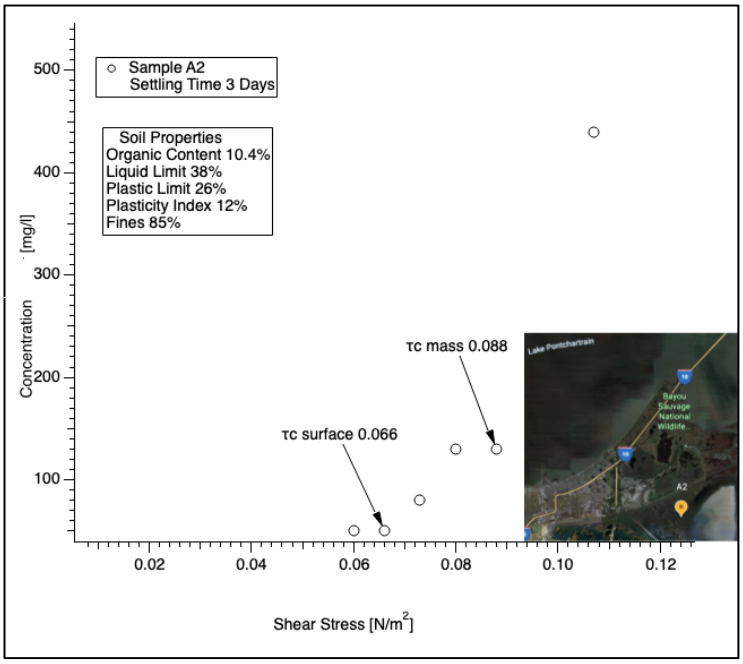

Figure 12-5 Concentrations inside the Shaker as a function of bottom shear stress. For sample A2 with 3 days of settling time τc shows the erosion critical shear stress for surface and mass erosion.

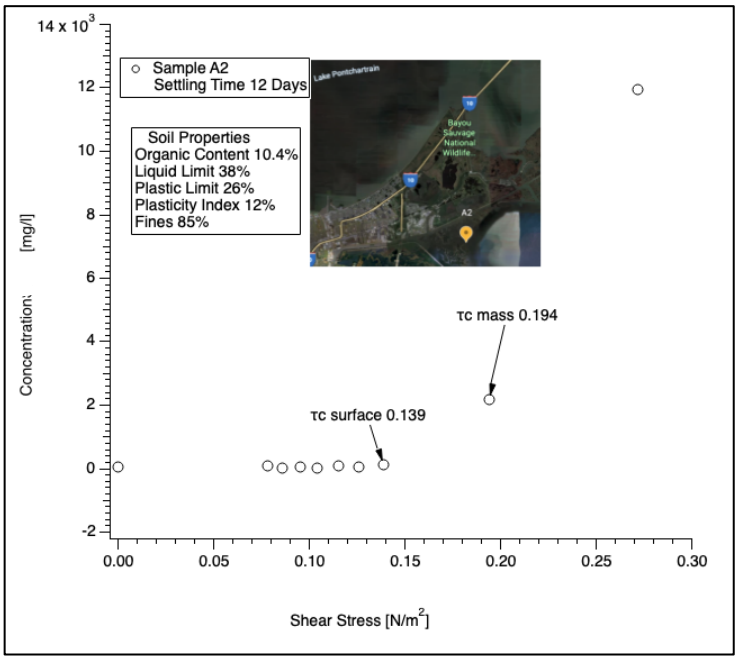

Figure 12-6 Concentrations inside the Shaker as a function of bottom shear stress. For sample A2 with 12 days of settling time τc shows the erosion critical shear stress for surface and mass erosion.

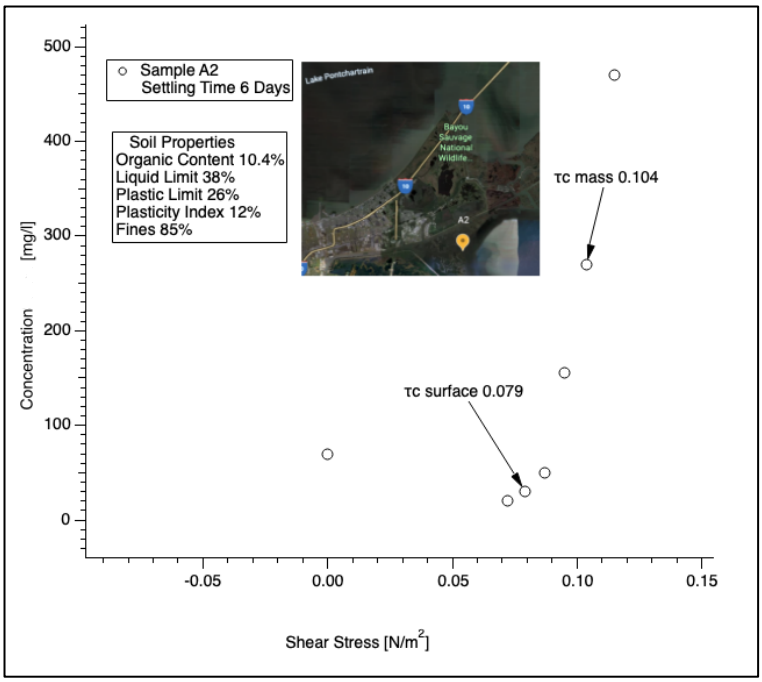

Figure 12-8 Concentrations inside the Shaker as a function of bottom shear stress. For sample A2 with 6 days of settling time τc shows the erosion critical shear stress for surface and mass erosion.

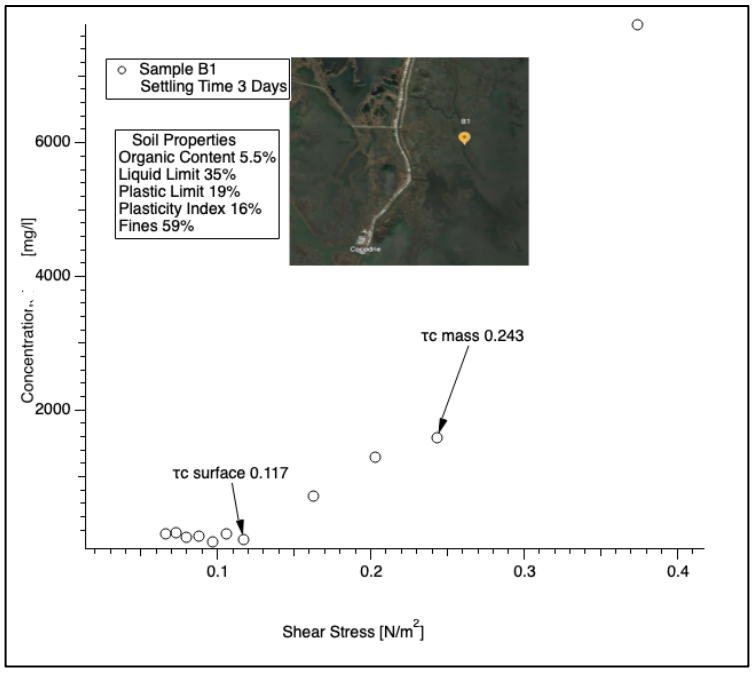

Figure 12-7 Concentrations inside the Shaker as a function of bottom shear stress. For sample B1 with 3 days of settling time τc shows the erosion critical shear stress for surface and mass erosion.

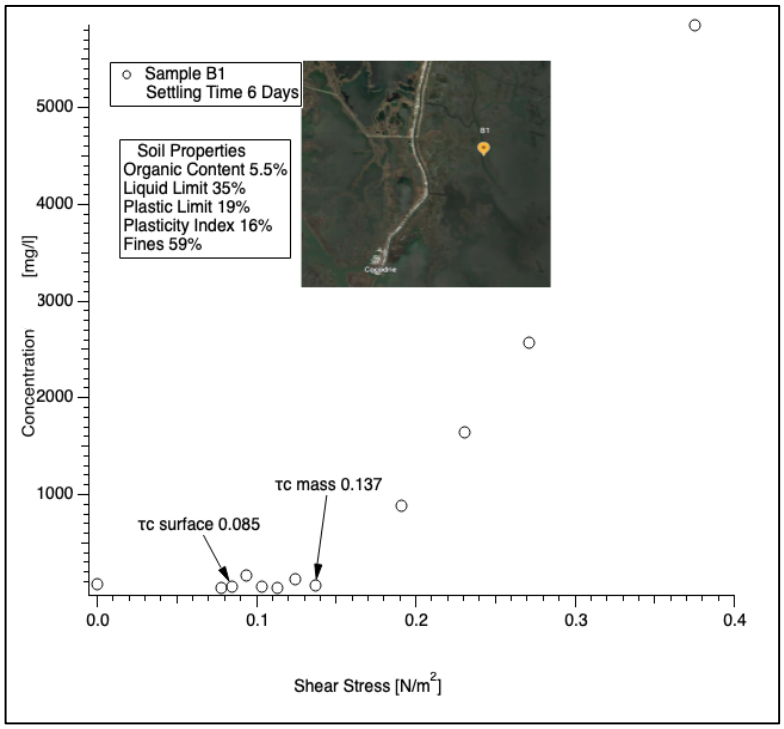

Figure 12-10 Concentrations inside the Shaker as a function of bottom shear stress. For sample B1 with 6 days of settling time τc shows the erosion critical shear stress for surface and mass erosion.

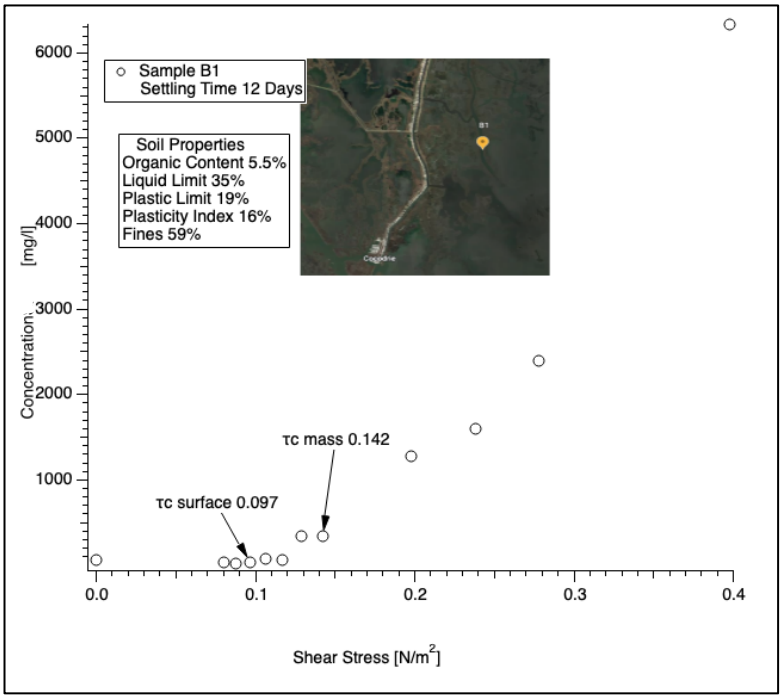

Figure 12-9 Concentrations inside the Shaker as a function of bottom shear stress. For sample B1 with 12 days of settling time τc shows the erosion critical shear stress for surface and mass erosion.

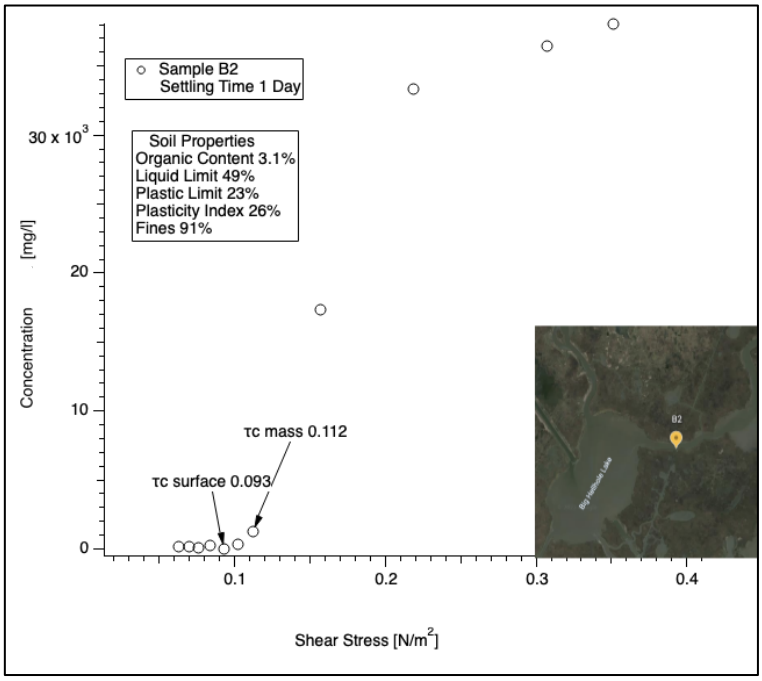

Figure 12-12 Concentrations inside the Shaker as a function of bottom shear stress. For sample B1 with one day of settling time τc shows the erosion critical shear stress for surface and mass erosion.

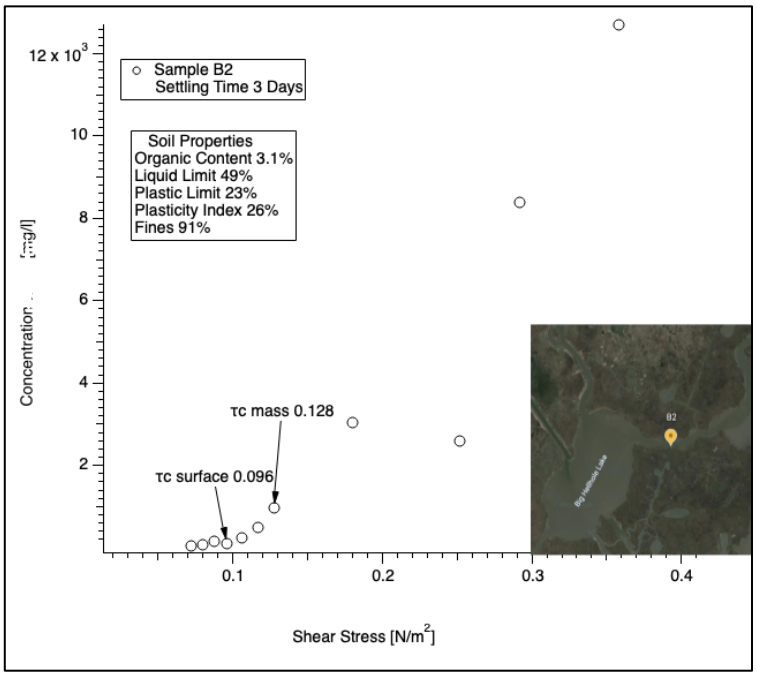

Figure 12-11 Concentrations inside the Shaker as a function of bottom shear stress. For sample B2 with six days of settling time τc shows the erosion critical shear stress for surface and mass erosion.

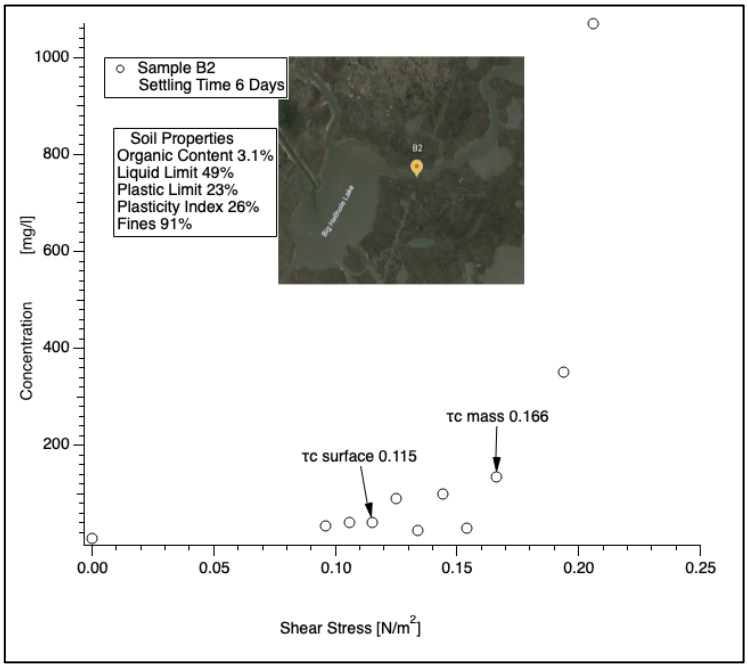

Figure 12-13 Concentrations inside the Shaker as a function of bottom shear stress. For sample B2 with five days of settling time τc shows the erosion critical shear stress for surface and mass erosion.

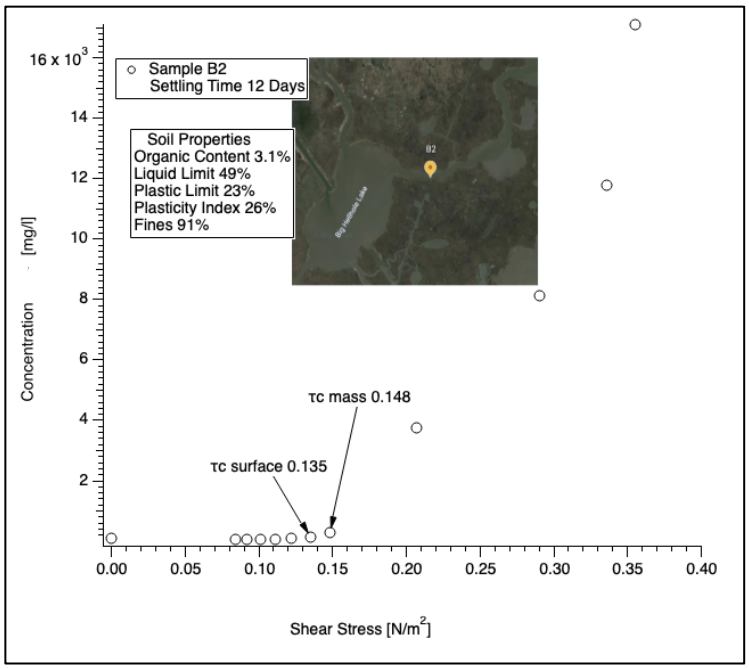

Figure 12-14 Concentrations inside the Shaker as a function of bottom shear stress. For sample B2 with 12 days of settling time τc shows the erosion critical shear stress for surface and mass erosion.

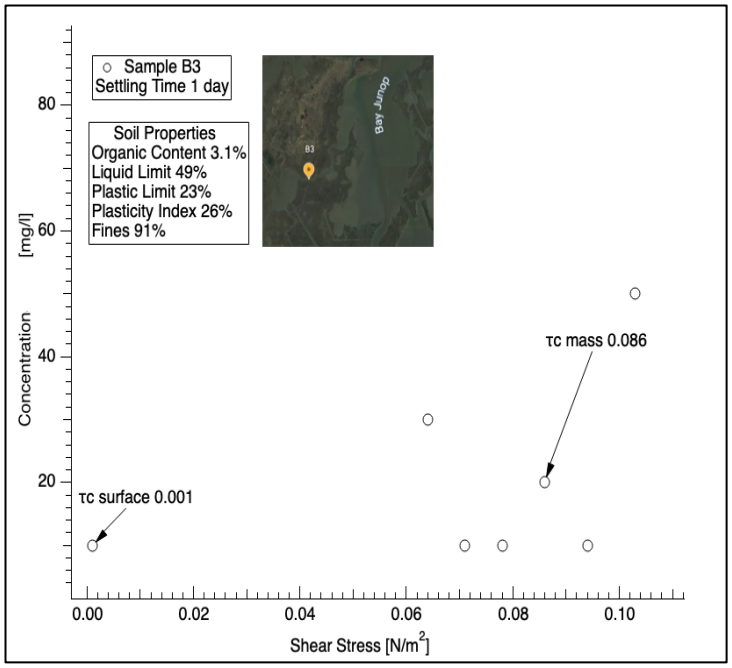

Figure 12-16 Concentrations inside the Shaker as a function of bottom shear stress. For sample B3 with one day of settling time τc shows the erosion critical shear stress for surface and mass erosion.

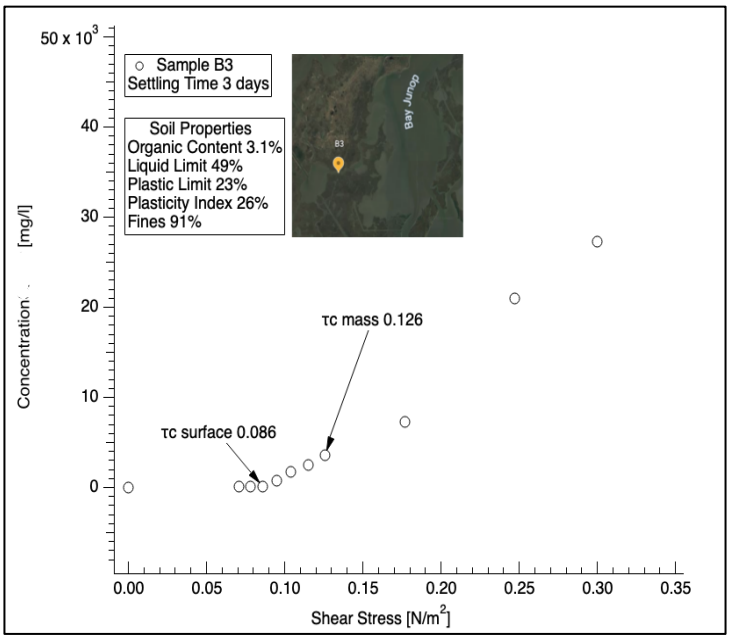

Figure 12-15 Concentrations inside the Shaker as a function of bottom shear stress. For sample B3 with three days of settling time τc shows the erosion critical shear stress for surface and mass erosion.

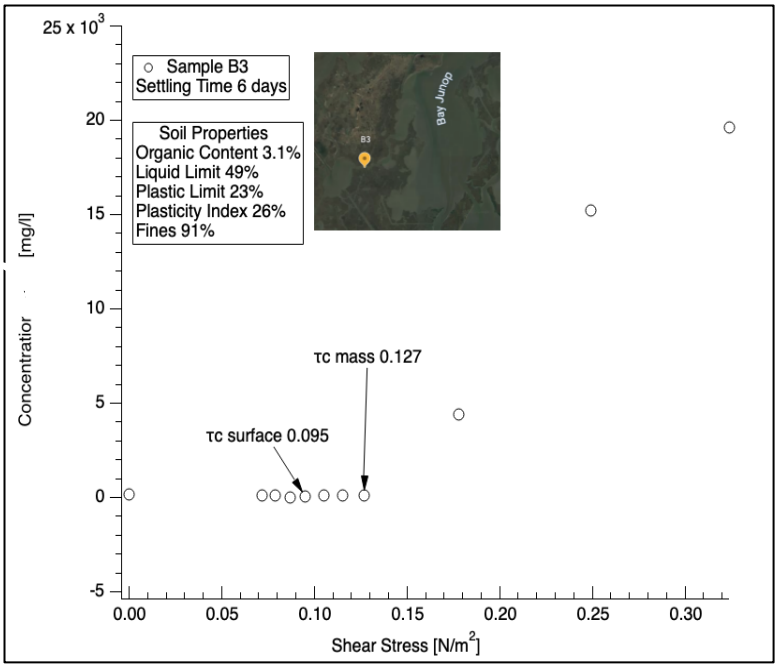

Figure 12-17 Concentrations inside the Shaker as a function of bottom shear stress. For sample B3 with six days of settling time τc shows the erosion critical shear stress for surface and mass erosion.

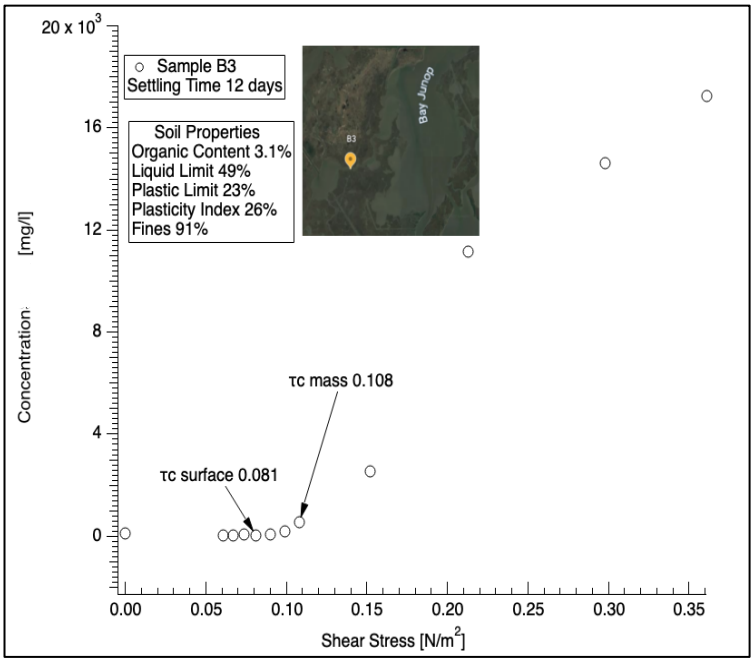

Figure 12-18 Concentrations inside the Shaker as a function of bottom shear stress. For sample B3 with 12 days of settling time τc shows the erosion critical shear stress for surface and mass erosion.

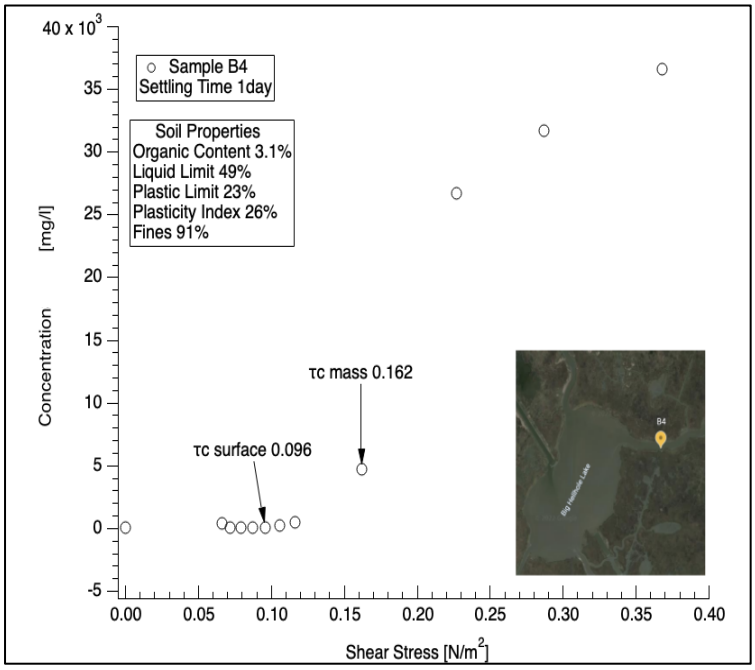

Figure 12-19 Concentrations inside the Shaker as a function of bottom shear stress. For sample B4 with one day of settling time τc shows the erosion critical shear stress for surface and mass erosion.

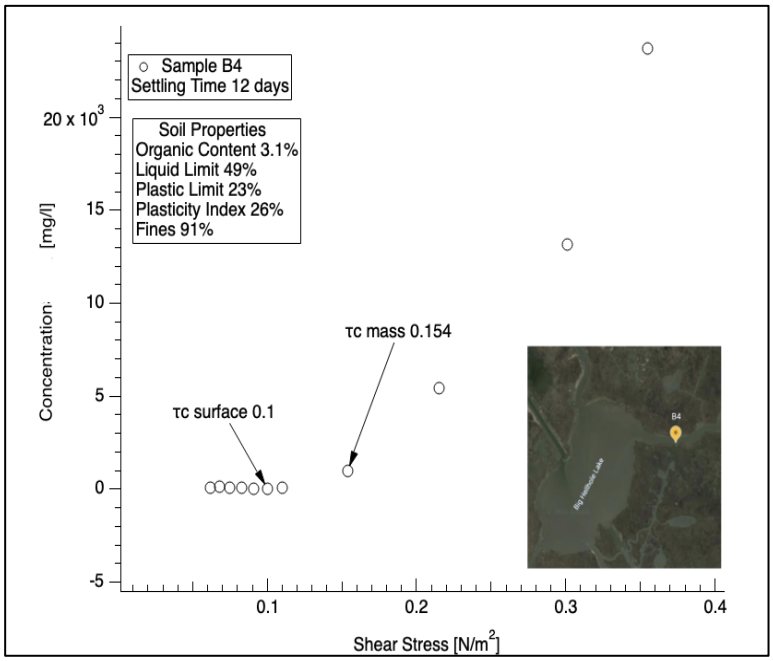

Figure 12-20 Concentrations inside the Shaker as a function of bottom shear stress. For sample B4 with 12 days of settling time τc shows the erosion critical shear stress for surface and mass erosion.

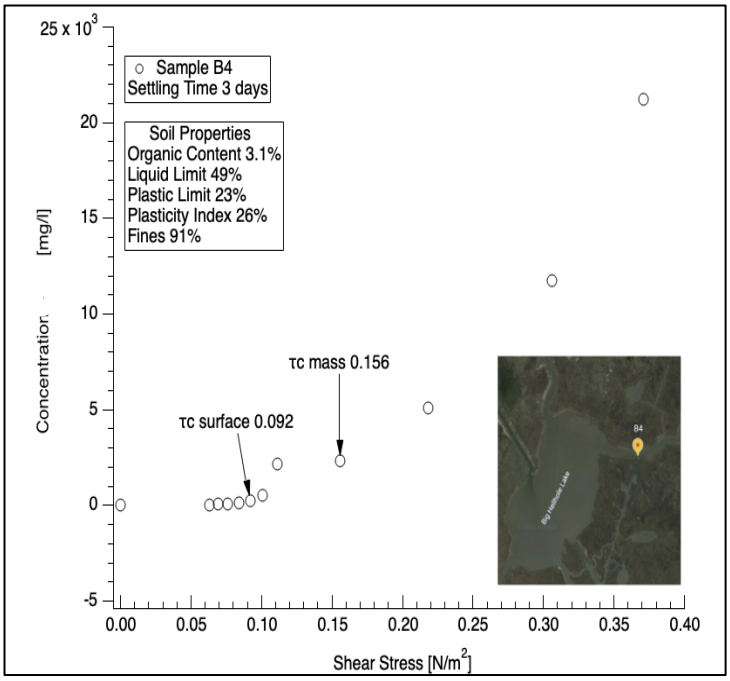

Figure 12-22 Concentrations inside the Shaker as a function of bottom shear stress. For sample B4 with three days of settling time τc shows the erosion critical shear stress for surface and mass erosion.

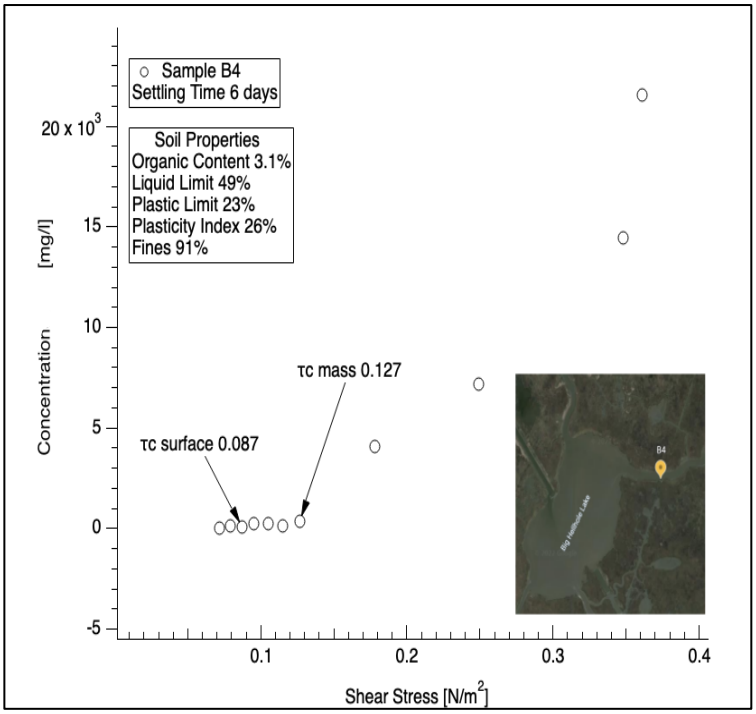

Figure 12-21 Concentrations inside the Shaker as a function of bottom shear stress. For sample B4 with six days of settling time τc shows the erosion critical shear stress for surface and mass erosion.

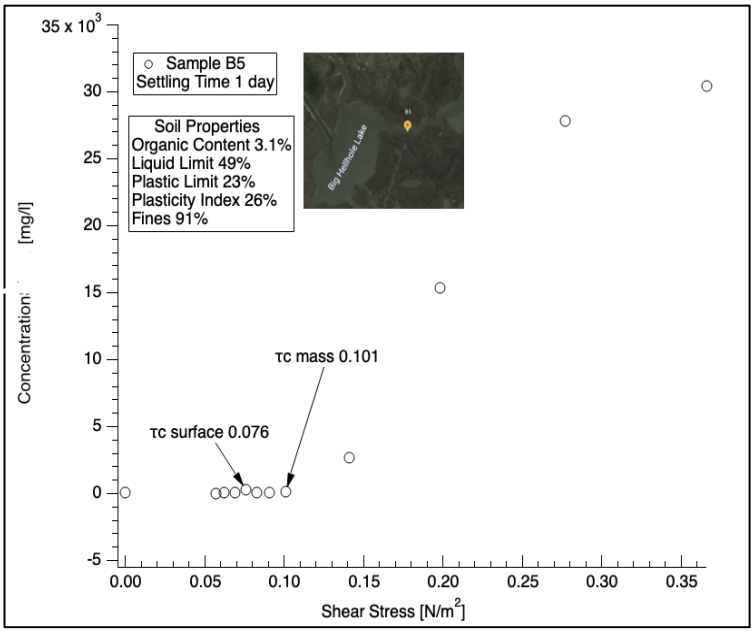

Figure 12-24 Concentrations inside the Shaker as a function of bottom shear stress. For sample B5 with one day of settling time τc shows the erosion critical shear stress for surface and mass erosion.

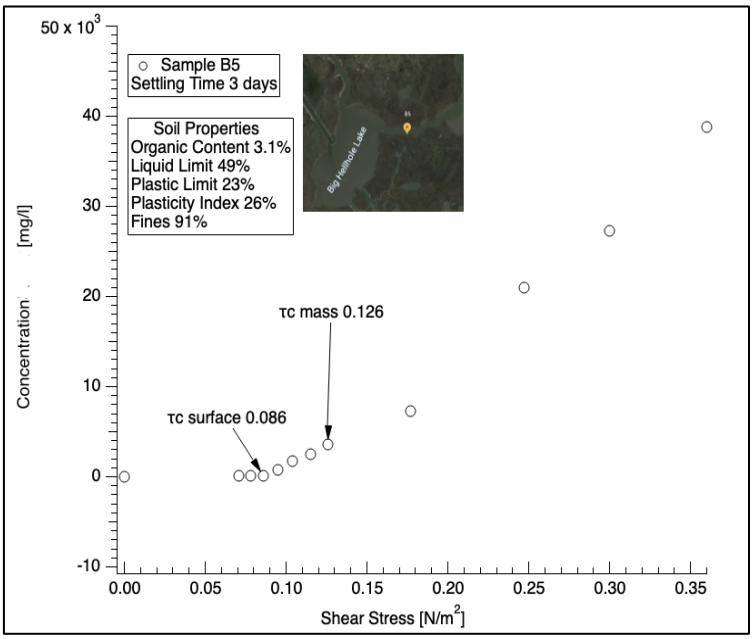

Figure 12-23 Concentrations inside the Shaker as a function of bottom shear stress. For sample B5 with three days of settling time τc shows the erosion critical shear stress for surface and mass erosion.

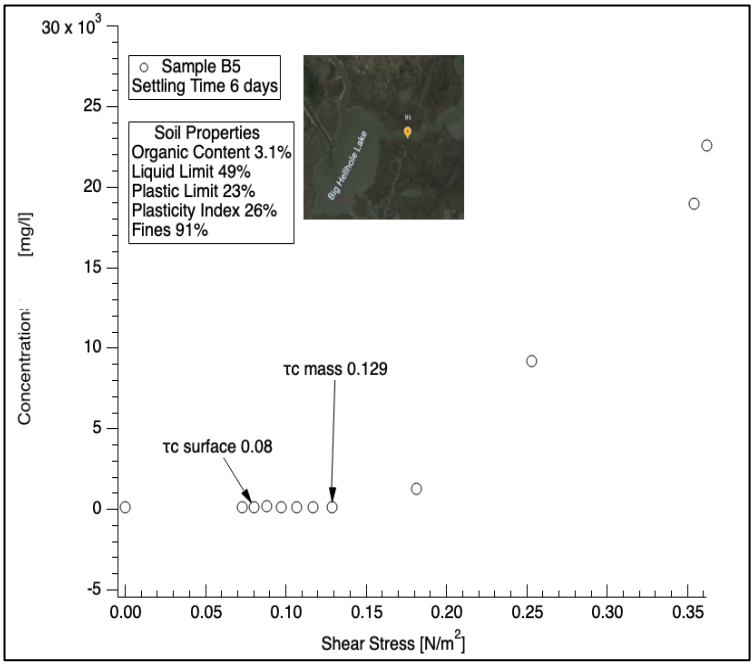

Figure 12-26 Concentrations inside the Shaker as a function of bottom shear stress. For sample B5 with six days of settling time τc shows the erosion critical shear stress for surface and mass erosion.

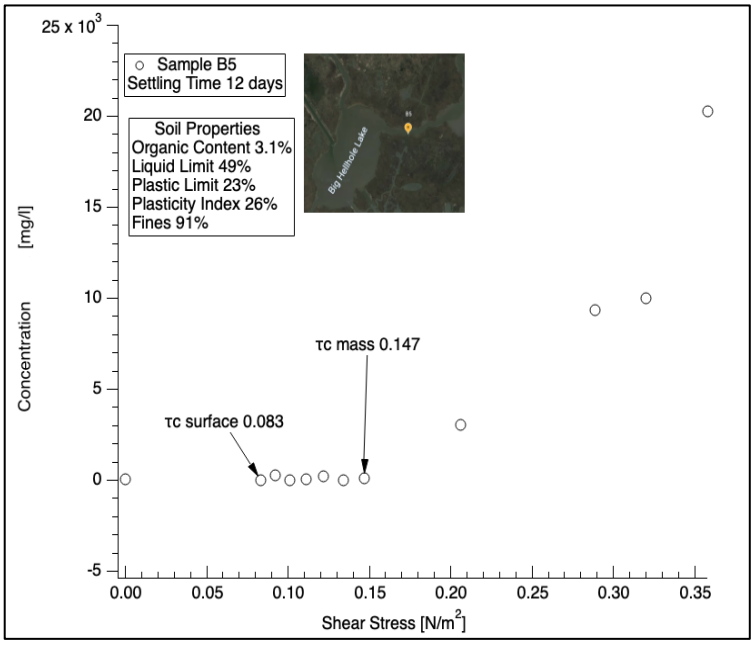

Figure 12-25 Concentrations inside the Shaker as a function of bottom shear stress. For sample B5 with 12 days of settling time τc shows the erosion critical shear stress for surface and mass erosion.

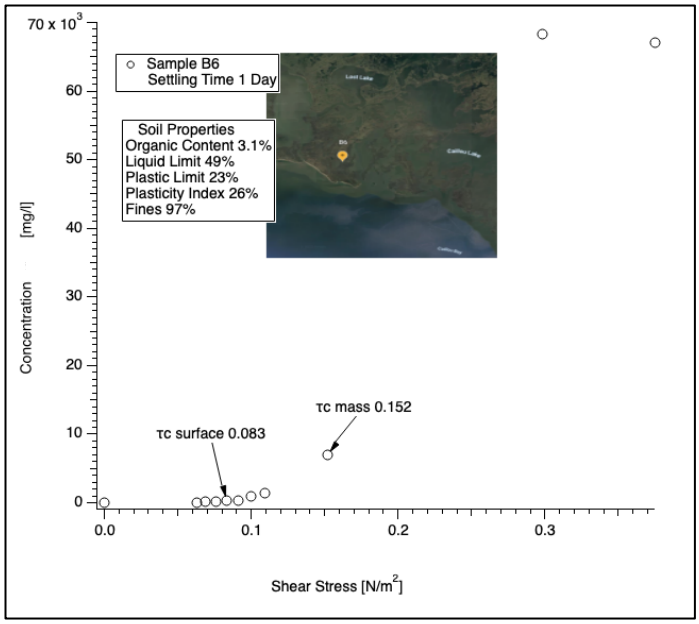

Figure 12-27 Concentrations inside the Shaker as a function of bottom shear stress. For sample B6 with one day of settling time τc shows the erosion critical shear stress for surface and mass erosion.

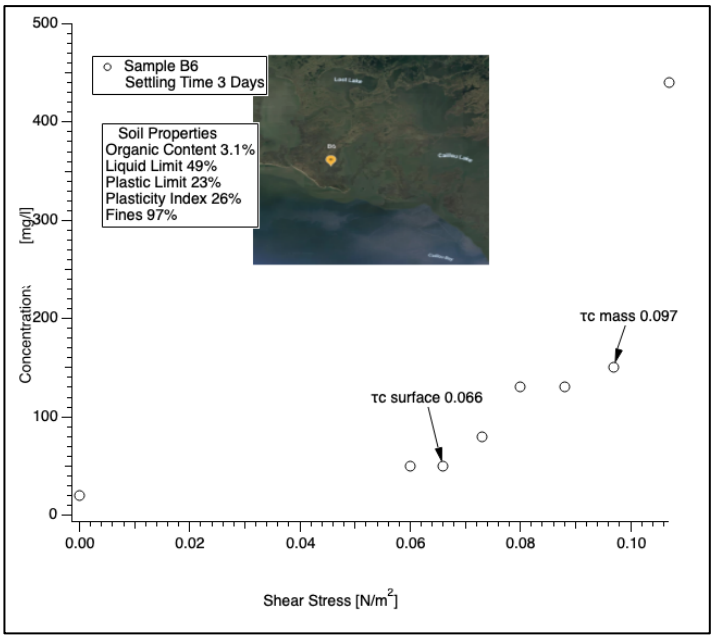

Figure 12-28 Concentrations inside the Shaker as a function of bottom shear stress. For sample B6 with three days of settling time τc shows the erosion critical shear stress for surface and mass erosion.

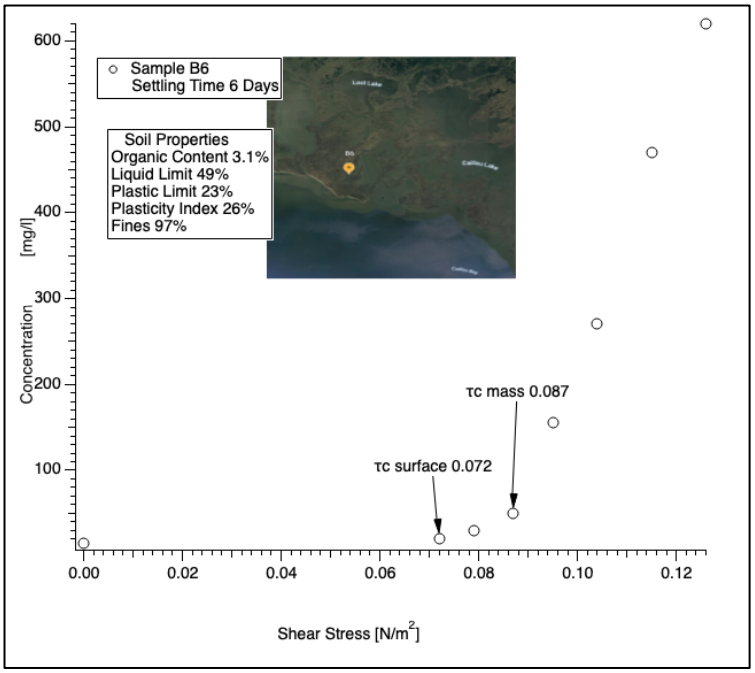

Figure 12-29 Concentrations inside the Shaker as a function of bottom shear stress. For sample B6 with six days of settling time τc shows the erosion critical shear stress for surface and mass erosion.

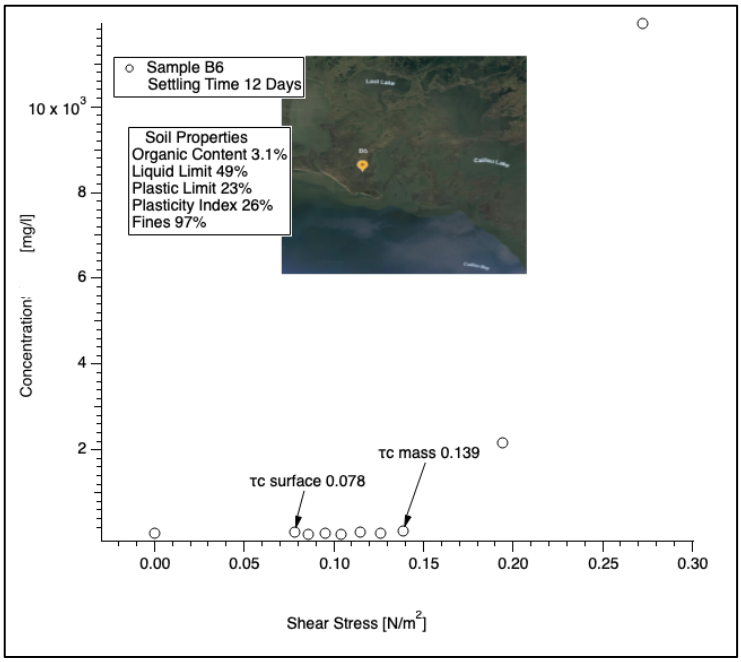

Figure 12-30 Concentrations inside the Shaker as a function of bottom shear stress. For sample B6 with 12 days of settling time τc shows the erosion critical shear stress for surface and mass erosion.

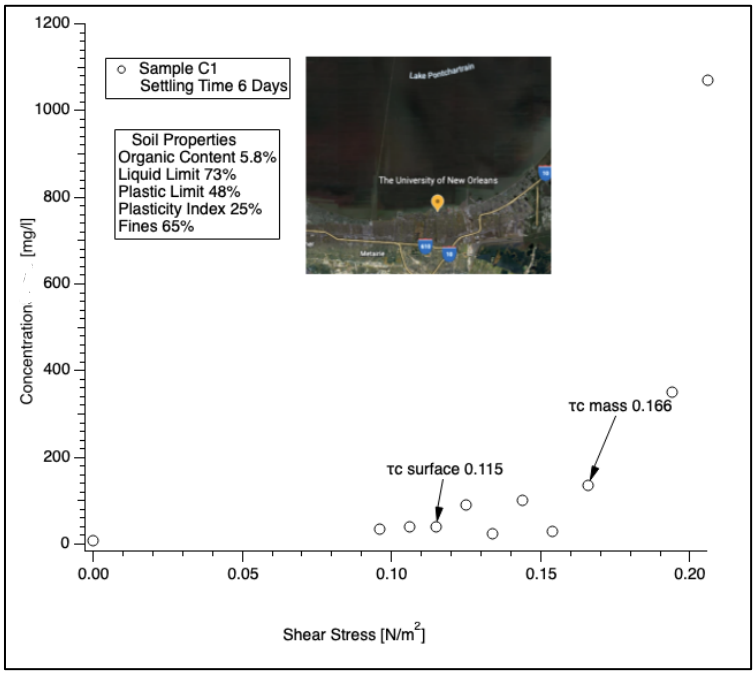

Figure 12-31 Concentrations inside the Shaker as a function of bottom shear stress. For sample C1 with six days of settling time τc shows the erosion critical shear stress for surface and mass erosion.

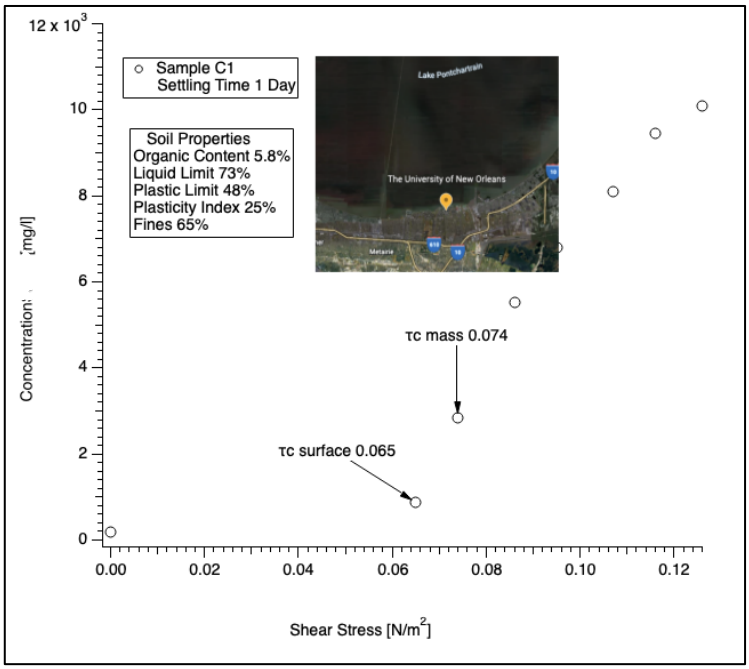

Figure 12-32 Concentrations inside the Shaker as a function of bottom shear stress. For sample C1 with one day of settling time τc shows the erosion critical shear stress for surface and mass erosion.

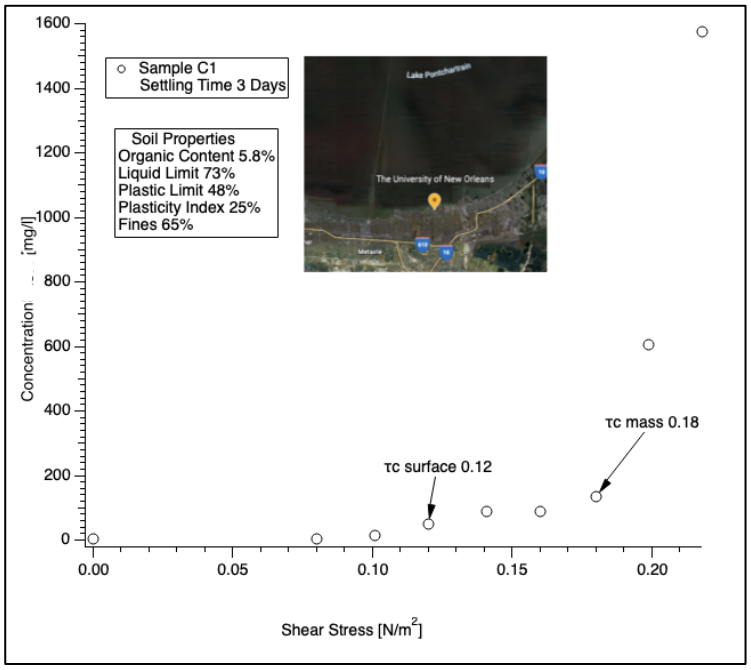

Figure 12-34 Concentrations inside the Shaker as a function of bottom shear stress. For sample C1 with three days of settling time τc shows the erosion critical shear stress for surface and mass erosion.

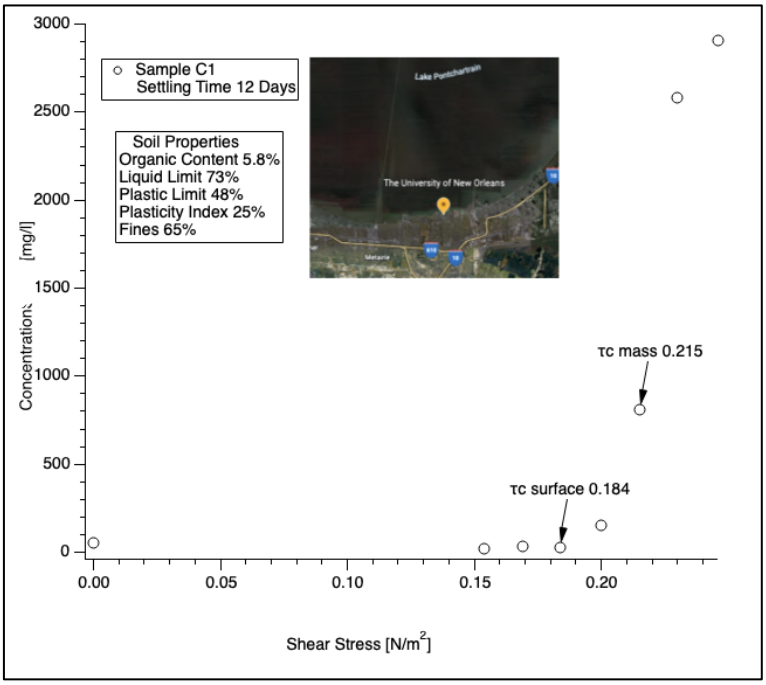

Figure 12-33 Concentrations inside the Shaker as a function of bottom shear stress. For sample C1 with 12 days of settling time τc shows the erosion critical shear stress for surface and mass erosion.

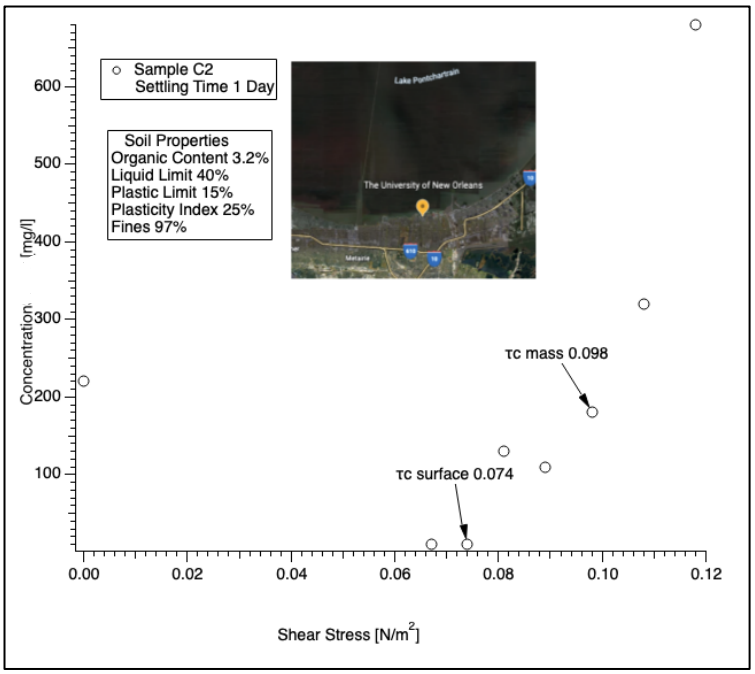

Figure 12-36 Concentrations inside the Shaker as a function of bottom shear stress. For sample C2 with one day of settling time τc shows the erosion critical shear stress for surface and mass erosion.

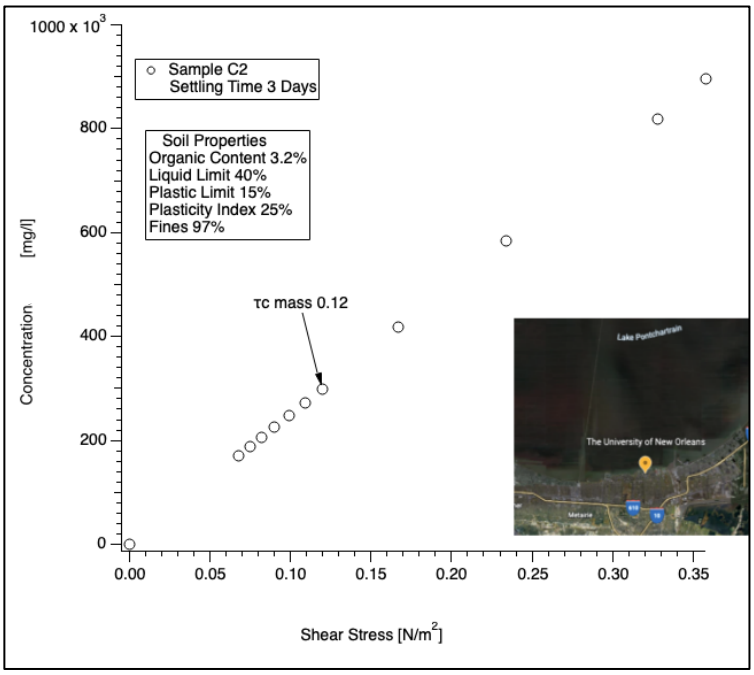

Figure 12-35 Concentrations inside the Shaker as a function of bottom shear stress. For sample C2 with three days of settling time τc shows the erosion critical shear stress for surface and mass erosion.

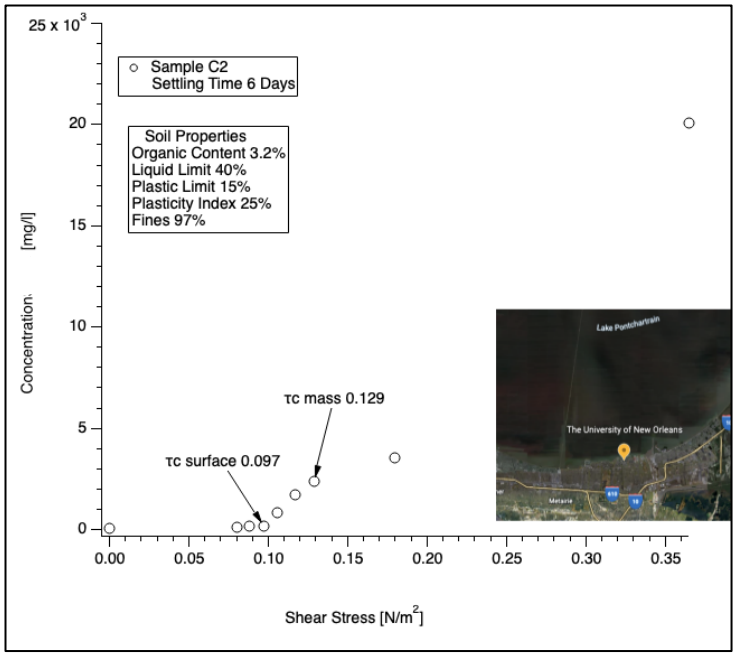

Figure 12-38 Concentrations inside the Shaker as a function of bottom shear stress. For sample C2 with six days of settling time τc shows the erosion critical shear stress for surface and mass erosion.

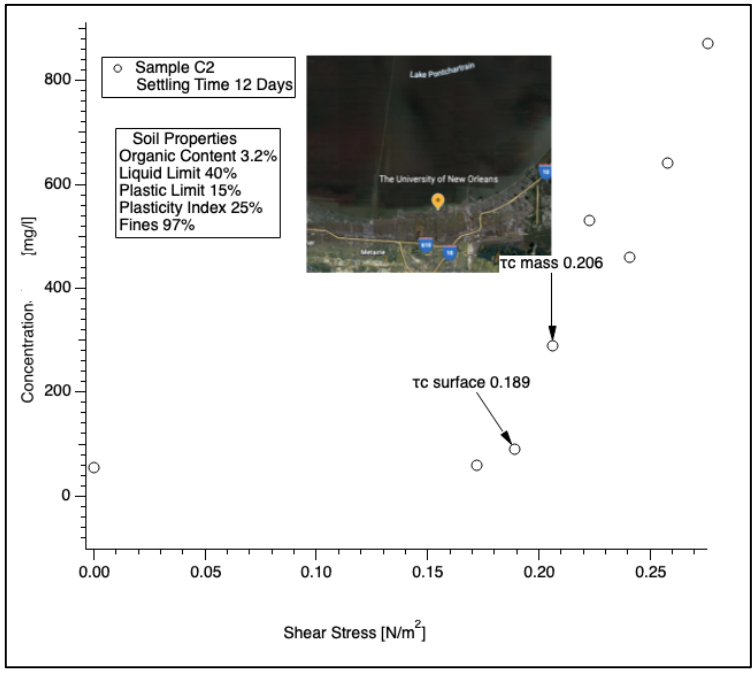

Figure 12-37 Concentrations inside the Shaker as a function of bottom shear stress. For sample C2 with 12 days of settling time τc shows the erosion critical shear stress for surface and mass erosion.

a

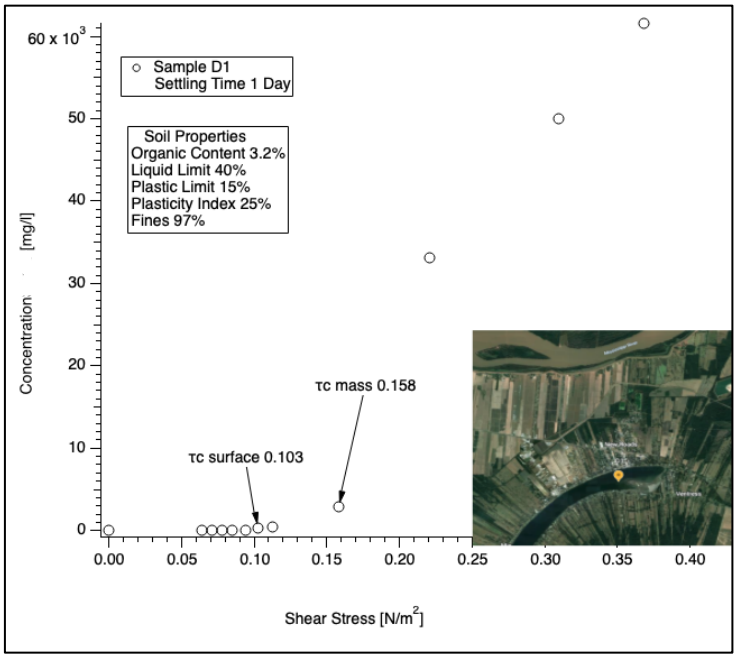

Figure 12-40 Concentrations inside the Shaker as a function of bottom shear stress. For sample D1 with one day of settling time τc shows the erosion critical shear stress for surface and mass erosion.

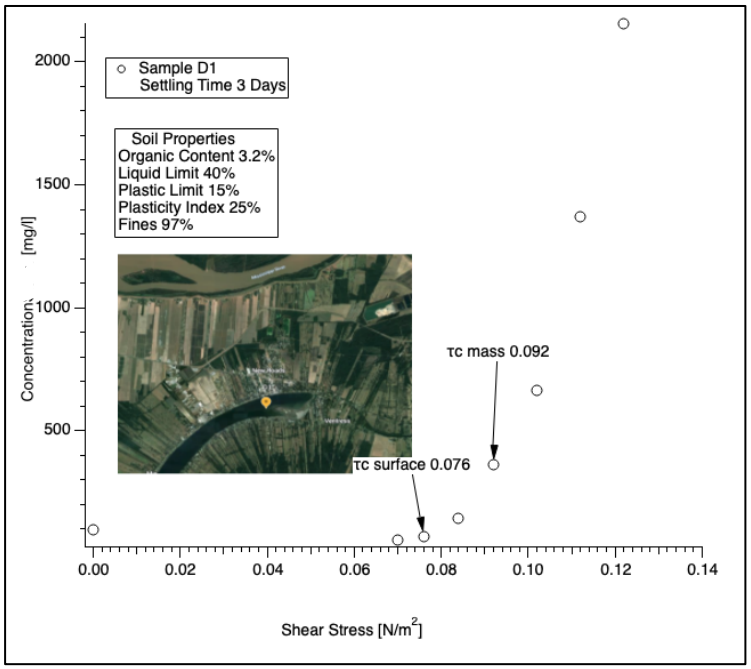

Figure 12-39 Concentrations inside the Shaker as a function of bottom shear stress. For sample D1 with three days of settling time τc shows the erosion critical shear stress for surface and mass erosion.

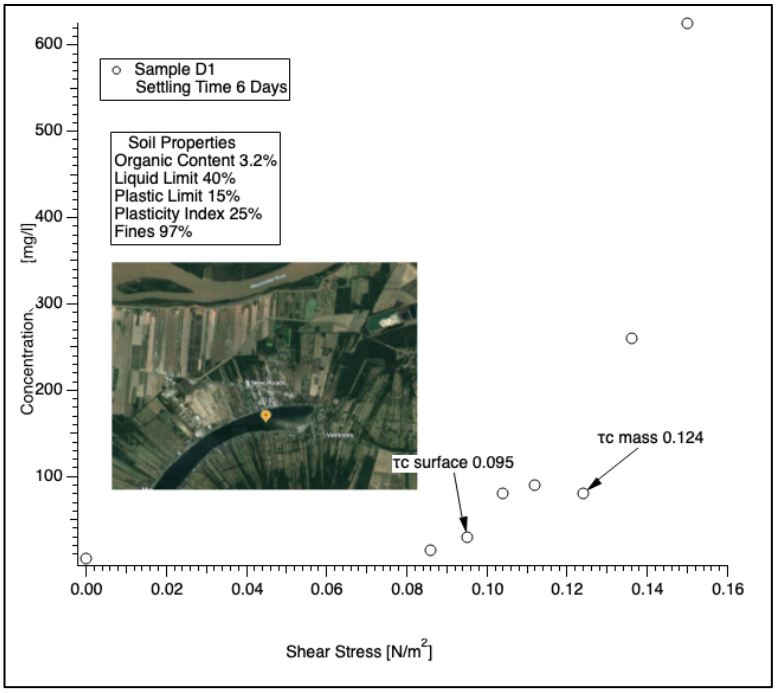

Figure 12-42 Concentrations inside the Shaker as a function of bottom shear stress. For sample D1 with six days of settling time τc shows the erosion critical shear stress for surface and mass erosion.

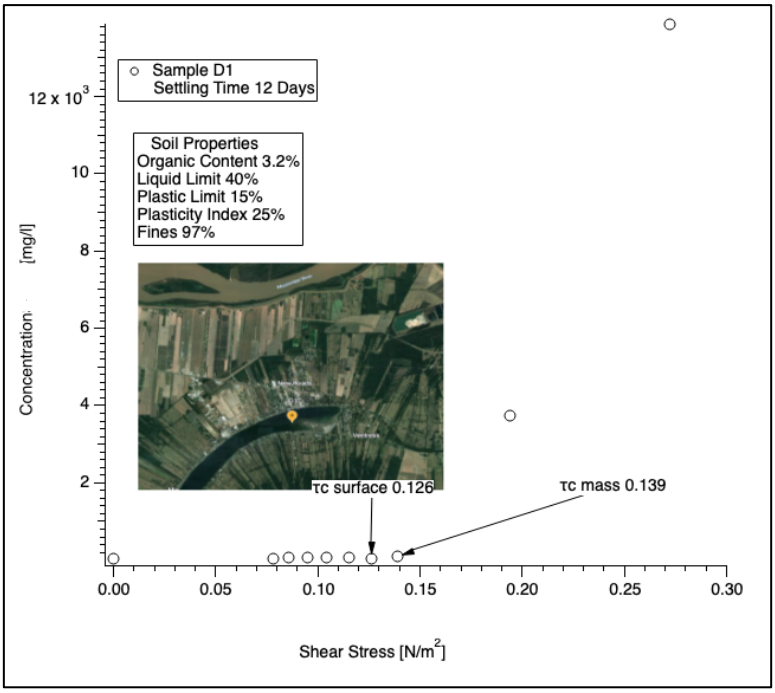

Figure 12-41 Concentrations inside the Shaker as a function of bottom shear stress. For sample D1 with 12 days of settling time τc shows the erosion critical shear stress for surface and mass erosion.

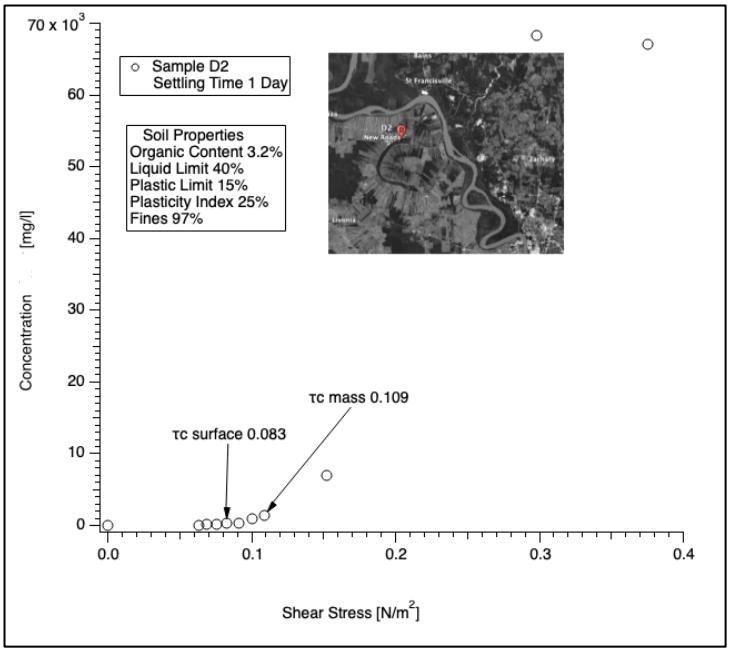

Figure 12-43 Concentrations inside the Shaker as a function of bottom shear stress. For sample D2 with 1 day of settling time τc shows the erosion critical shear stress for surface and mass erosion.

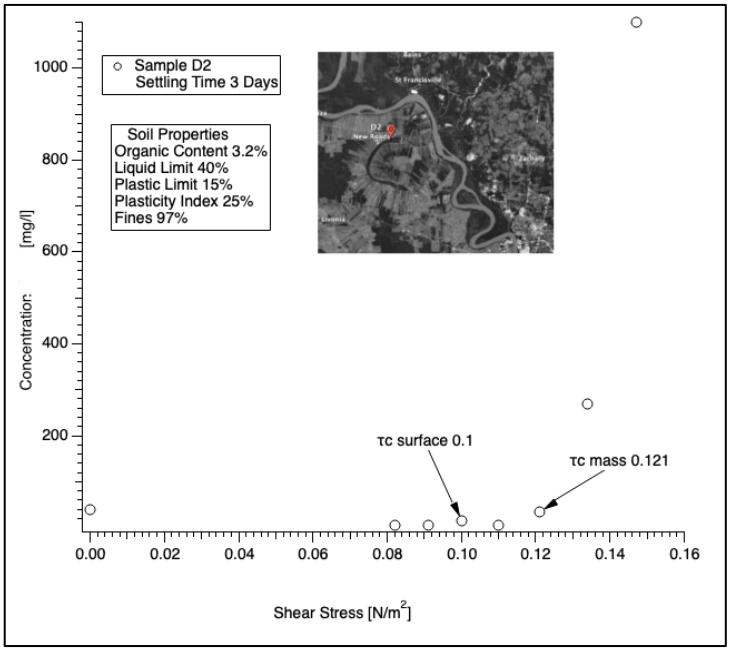

Figure 12-44 Concentrations inside the Shaker as a function of bottom shear stress. For sample D2 with three days of settling time τc shows the erosion critical shear stress for surface and mass erosion.

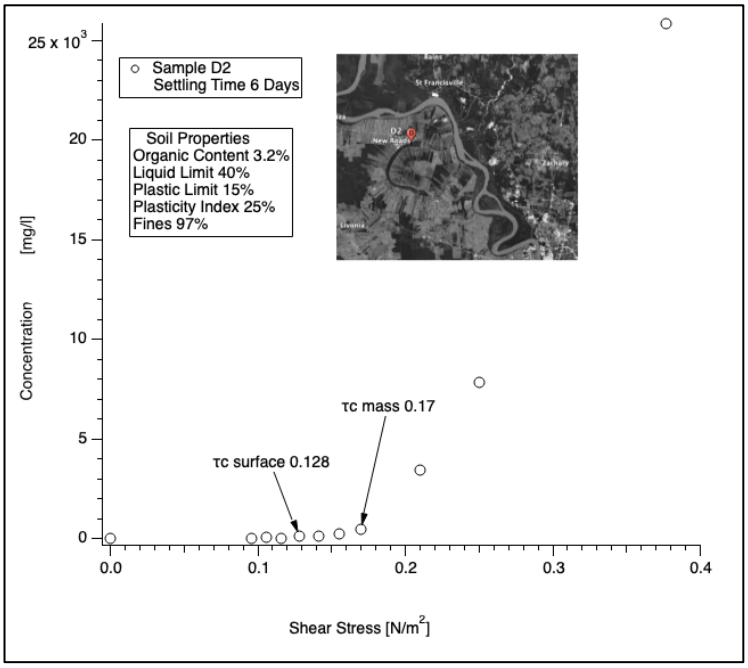

Figure 12-46 Concentrations inside the Shaker as a function of bottom shear stress. For sample D2 with six days of settling time τc shows the erosion critical shear stress for surface and mass erosion.

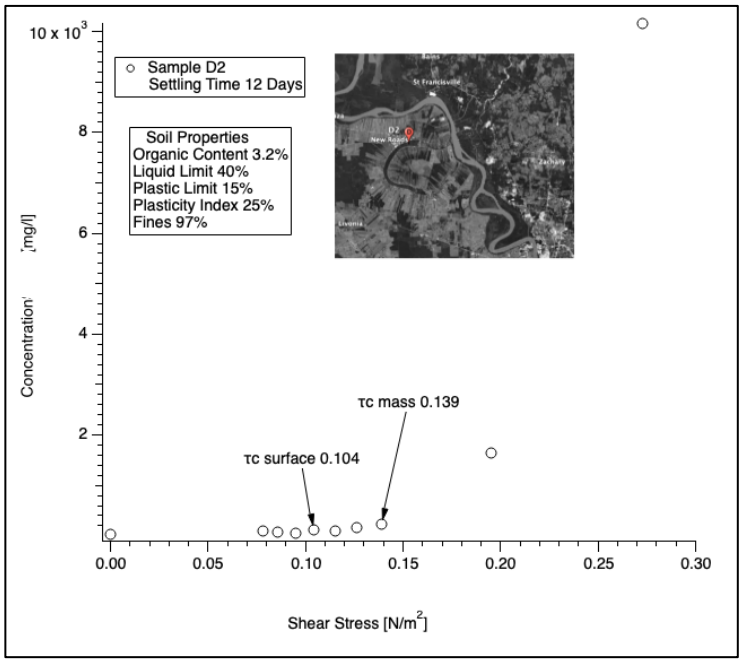

Figure 12-45 Concentrations inside the Shaker as a function of bottom shear stress. For sample D2 with 12 days of settling time τc shows the erosion critical shear stress for surface and mass erosion.

Appendix B

Python Model Open Water:

```
import matplotlib.pyplot as plt
import numpy as np
import pandas as pd

import csv
import math
import os

print('working directory',os.getcwd())
print('/Users/laithalshamaileh/PycharmProjects/resuspen-John-LaithTesting')
boundaryconditions = []
with open('Issac-meteo-canal-station.csv', 'r') as csvFile:
    reader = csv.reader(csvFile)
    for row in reader: #vn,b
        #print(row)
        boundaryconditions.append(row)
    csvFile.close()
#print(boundaryconditions)

bin_degree = []
with open('Bin-DegreeFiles.csv','r') as csvfile:
    reader = csv.reader(csvfile)
    for row in reader:
        bin_degree.append(row)
    csvfile.close()
#print(bin_degree)

def get_fetch_from_degree (degree, range_degrees):
    for range_degree in range_degrees :
        if (range_degree[0] <=degree and range_degree [1] >=degree):
            return range_degree[2]
    return None

def convert_range (bin_degree):
    degree_range = []
    for bin in bin_degree:
        second = bin[1]
        x,y = second.split('-')
        d = (float(x), float(y), float(bin[2]))
        degree_range.append(d)
    return degree_range

range_degrees = convert_range(bin_degree)
#print(range_degrees)

fetch = get_fetch_from_degree(102,range_degrees)
#print(fetch)

def convert_wind_speed (wind_speeds):
```

```
    speeds = []
    for wind_speed in wind_speeds:
        try:
            d = (float(wind_speed[0]), float(wind_speed[1]))
            speeds.append(d)
        except:
            x = wind_speed[0][-3:]
            d = (float(x), float(wind_speed[1]))
            speeds.append(d)

    return speeds

speeds = convert_wind_speed(boundaryconditions)
#print(speeds)

fetches = []
for speed in speeds:
    fetch = get_fetch_from_degree(speed[1],range_degrees)
    fetches.append(fetch)

# print(fetches)

depth = 1

y_CFcon = []
y_silcon = []
y_CPcon = []

def compute_concentrations(i):
    g = 9.81
    row = 1000
    gamma = 9810
    pi = math.pi
    u10 = speeds[i][0]
    F = fetches[i]

    delta = (g * depth) / (u10 * u10)
    print(g, F)
    X = (g * F) / (u10 * u10)
    A1 = .493 * delta ** .75
    A2 = .331 * delta ** 1.01
    B1 = .00313 * X ** .57
    B2 = .0005215 * X ** .73
    sub = B1 / (math.tanh(A1))
    epsi = .00364 * (math.tanh(A1) * math.tanh(sub)) ** 1.74
    nu = .133 * (math.tanh(A2) * math.tanh((B2) / (math.tanh(A2)))) ** -.37
    Energy = (epsi * u10 ** 4) / (g * g)
    freqPK = nu * g / u10
    Period = freqPK ** -1

    SigHt = 3.8 * (Energy ** .5)

    ac = 100
    Tres = 3600
    Tcon = 6
    Days = 1
    tcr = (0.02*Days+0.001)
```

```
    day = i + 1
    tcr = 0.1
    #tcr = 0.008 * day + 0.1562
    #Clip to max of 0.25
    #tcr = np.clip(tcr, 0, 0.25)
    m = 1.
    n = 3.
    Cf = .0025
    ka = .0275
    Uw = u10 * ka
    L0 = (g * Period * Period) / (2 * pi)
    L1 = L0 * math.tanh((2. * pi * depth) / L0)
    L2 = L1 * math.tanh((2. * pi * depth) / L1)
    Uorb = (g * SigHt * Period) / (2. * L2 * math.cosh((2. * pi * depth) /
L2))
    Utide = 0.1 * math.sin(i * 2 * 3.14 / 14.)
    Uinflo = .1
    Ubed = Utide + Uinflo + Uw + Uorb
    taubed = Cf * row * Ubed * Ubed
    Eres = (ac / (Tres * Tcon ** m)) * (taubed / tcr - 1.) ** n  #
Resuspension of silts and clays

    # !Begin computing resuspension using van Rijn
    D50 = .00018
    D90 = .00030
    Ucritw = .24 * ((2.65 - 1) * g) ** .66 * D50 ** .33 * Period ** .33
    Ucritc = .19 * D50 ** .1 * math.log10((12. * depth) / (3. * D90))
    Ucrit = ((Uinflo) / (Uinflo + Uorb)) * Ucritc + ((Uinflo) / (Uinflo +
Uorb) - 1.) * Ucritw

    ygam = .4
    Ue = Uinflo + ygam * Uorb
    Me = (Ue - Ucrit) / (math.sqrt(g * D50 * (2.65 - 1.)))
    alphas = .01
    Dstar = D50 * ((g * (2.65 - 1.)) / (.000001 * .000001)) ** (1. / 3.)
    qs = alphas * 2650. * Uinflo * D50 * Me ** 2.4 * Dstar ** -0.6  #
Resuspension of sand

    CFmas = 0.0
    silmas = 0.0
    CPmas = 0.0
    wsCF = .020334
    CFmas = max(.0001, CFmas + (.7 * Eres - wsCF * (CFmas / depth)) *
(86400.))
    CFcon = CFmas / depth
    wsil = .00097157
    silmas = max(.0001, silmas + (.2 * Eres - wsil * (silmas / depth)) *
(86400.))
    siltcon = silmas / depth
    wsCP = .000035816
    CPmas = max(.0001, CPmas + (.1 * Eres - wsCP * (CPmas / depth)) *
(86400.))
    CPcon = CPmas / depth

    return CFcon, siltcon, CPcon
```

```
    # Use write command to pick what outputs to be displayed

    print(str(i) + " " + str(CFcon) + " " + str(siltcon) + str(CPcon))
    y_CFcon.append(CFcon)
    y_silcon.append(siltcon)
    y_CPcon.append(CPcon)


def plot_chart(concentrations, names):
    legends = []
    for name, conc in zip(names, concentrations):
        plt.plot(conc)
        legends.append(f'y = {name}')

    #plt.title("Concentration")
    plt.xlabel("Days")
    plt.ylabel('Concentration mg/l')
    plt.legend(legends, loc='upper left')
    plt.show()



concentrationsDF = pd.DataFrame(dict(
    yConCF=y_CFcon,
    yConSil=y_silcon,
    yConCP=y_CPcon
))



tss_df = concentrationsDF.sum(axis=1)
tss_df.to_csv('tss.csv', index=False)
tss = tss_df.values
#plot_chart([tss, measured], ['TSS modeled', ' TSS measured'])
plot_chart([tss], ['TSS modeled'])

concentrationsDF.to_csv('concentrations.csv', index=False)
```

Python Model Marsh Accretion:

```
import pandas as pd
import numpy as np
from matplotlib import pyplot as plt

from parameters import *

# Data
marsh_edge_DF = pd.read_csv('WaterLevel_full.csv')
concentrations_DF = pd.read_csv('tss.csv')
```

```
concentration_names = concentrations_DF.columns.tolist()
print(concentration_names)
water_level = marsh_edge_DF.WaterLevel.values
marsh_elevation = marsh_edge_DF.MarshElevation.values

# Computations
def get_new_elevation(concentration):
    open_level = water_level + 1
    q_marsh_mgd = WIDTH * (HEIGHT ** 3) * (open_level - marsh_elevation) /
(WIDTH) * (Conversion_Factor_FIRST)
    sediment_in = q_marsh_mgd * concentration * Conversion_Factor_SECOND
    sediment_in_marsh = np.clip(sediment_in, a_min=0, a_max=None)
    q_marsh = sediment_in_marsh / SOIL_DENSITY   # ft3/day
    accretion = (q_marsh / OPEN_AREA_10_PCT) / Conversion_Factor_THIRD
    new_marsh_elevation = marsh_elevation + accretion
    return new_marsh_elevation

def plot_chart(elevations, elevation_names):
    for elevation in elevations:
        plt.plot(elevation)

    plt.title("Elevations")
    plt.xlabel("Days")
    plt.ylabel('Elevation ft')

    legend_titles = []
    for elevation_name in elevation_names:
        title = f'y = {elevation_name}'
        legend_titles.append(title)

    if len(legend_titles) > 0:
        plt.legend(legend_titles, loc='upper left')

    plt.show()


new_marsh_elevations_list = []
concentration_names = []
for name in concentration_names:
    concentration = pad_concentration(concentrations_DF[name].values)
    new_marsh_elevation = get_new_elevation(concentration)
    new_marsh_elevations_list.append(new_marsh_elevation)

#elevation_names = [s.replace('Con', 'Ele') for s in concentration_names]
#plot_chart(new_marsh_elevations_list, elevation_names)

# Aggregate
concentrations_agg_DF = concentrations_DF.sum(axis=1)
concentration = pad_concentration(concentrations_agg_DF.values)
new_marsh_elevation = get_new_elevation(concentration)
plot_chart([new_marsh_elevation],[])

elevation_df = pd.DataFrame(dict(new_marsh_elevation=new_marsh_elevation))
elevation_df.to_csv('elevation.csv', index=False, header=False)
# Parameters
WIDTH = 112992.13                   # ft
LENGTH = WIDTH                      # ft
```

```
OPEN_AREA = 764200000                  # ft^2  Open water area
HEIGHT = 0.5                          # ft
OPEN_AREA_10_PCT = 0.10 * OPEN_AREA     # 10% of Open water area
SOIL_DENSITY = 0.1800                 # g/cm3 Soil density
SOIL_DENSITY *= 62.4                  # lb/ft3 same as SoilDensity =
SoilDensity * 62.4
CONVERSION_FACTOR_FIRST = 0.538
CONVERSION_FACTOR_SECOND = 8.34
CONVERSION_FACTOR_THIRD = (24*2)
```

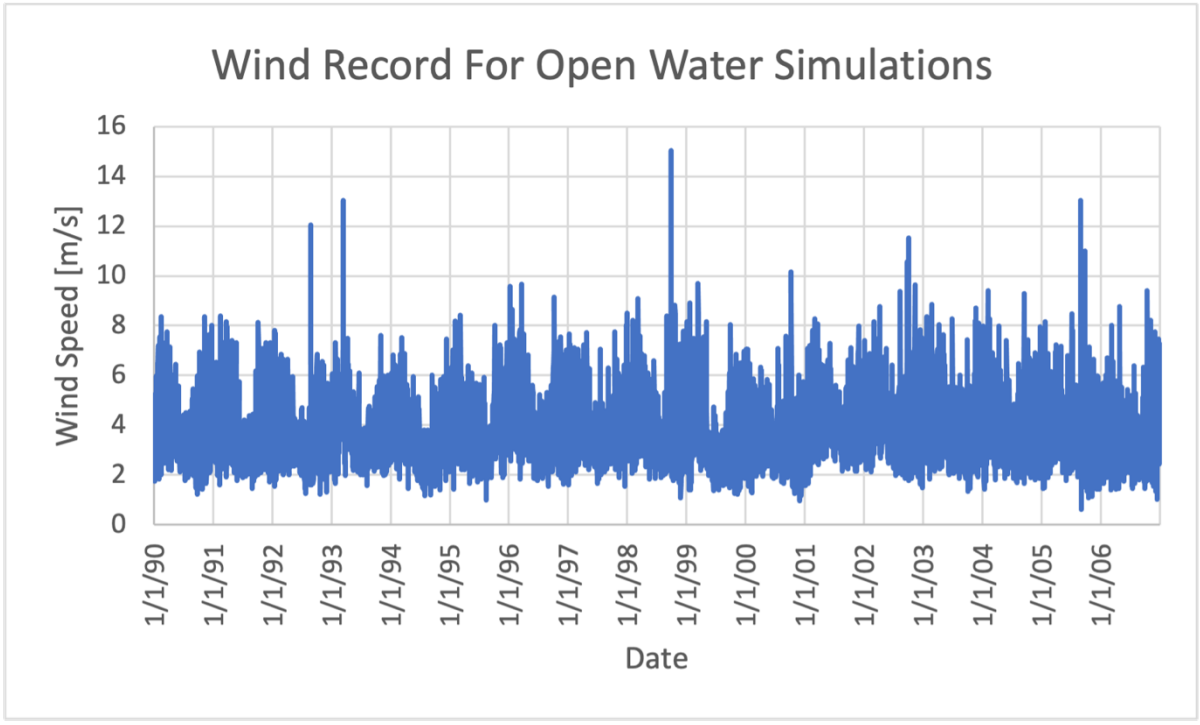

Figure 13-1 Wind Record used in open water simulations

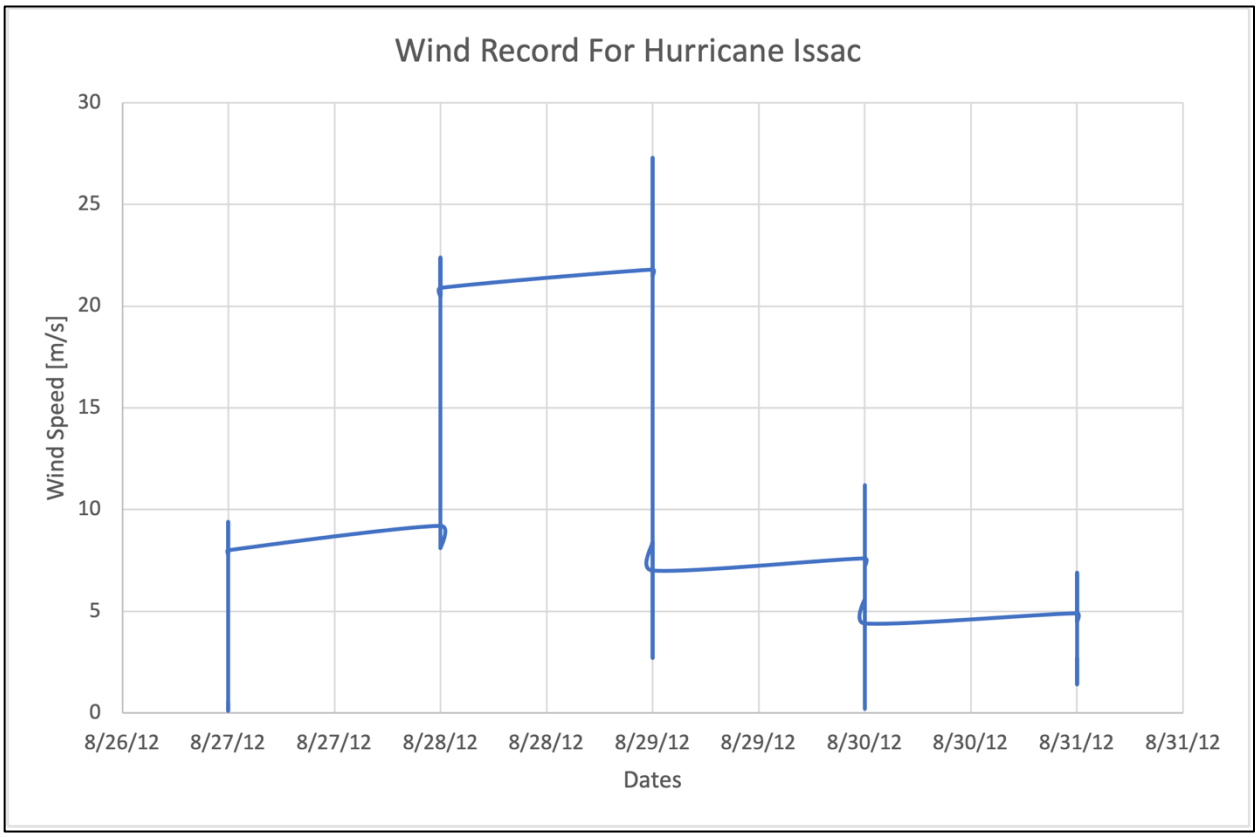

Figure 13-2 Wind record used for hurricane Isaac simulations

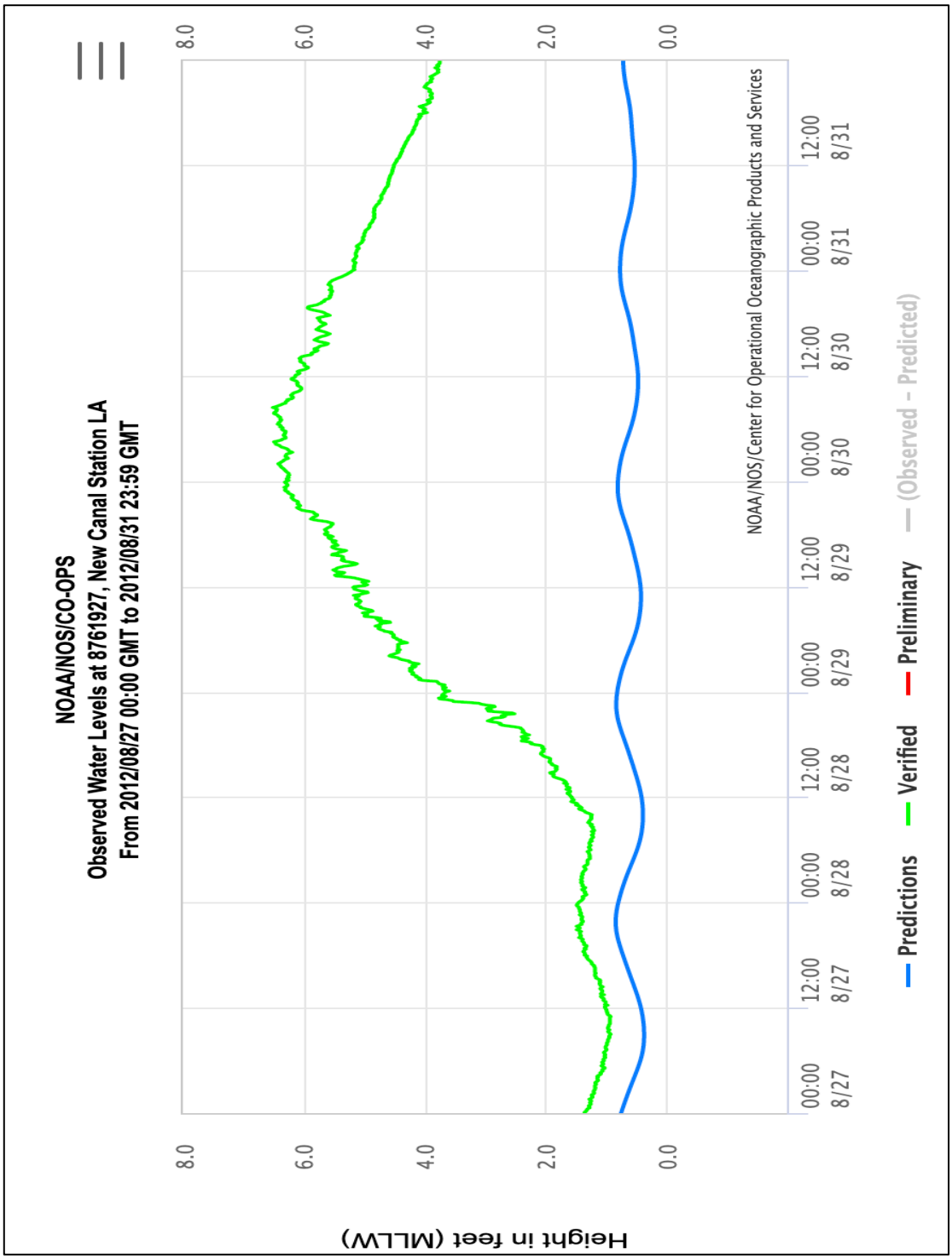

Figure 13-3 Tide and water elevations during the Isaac simulation period

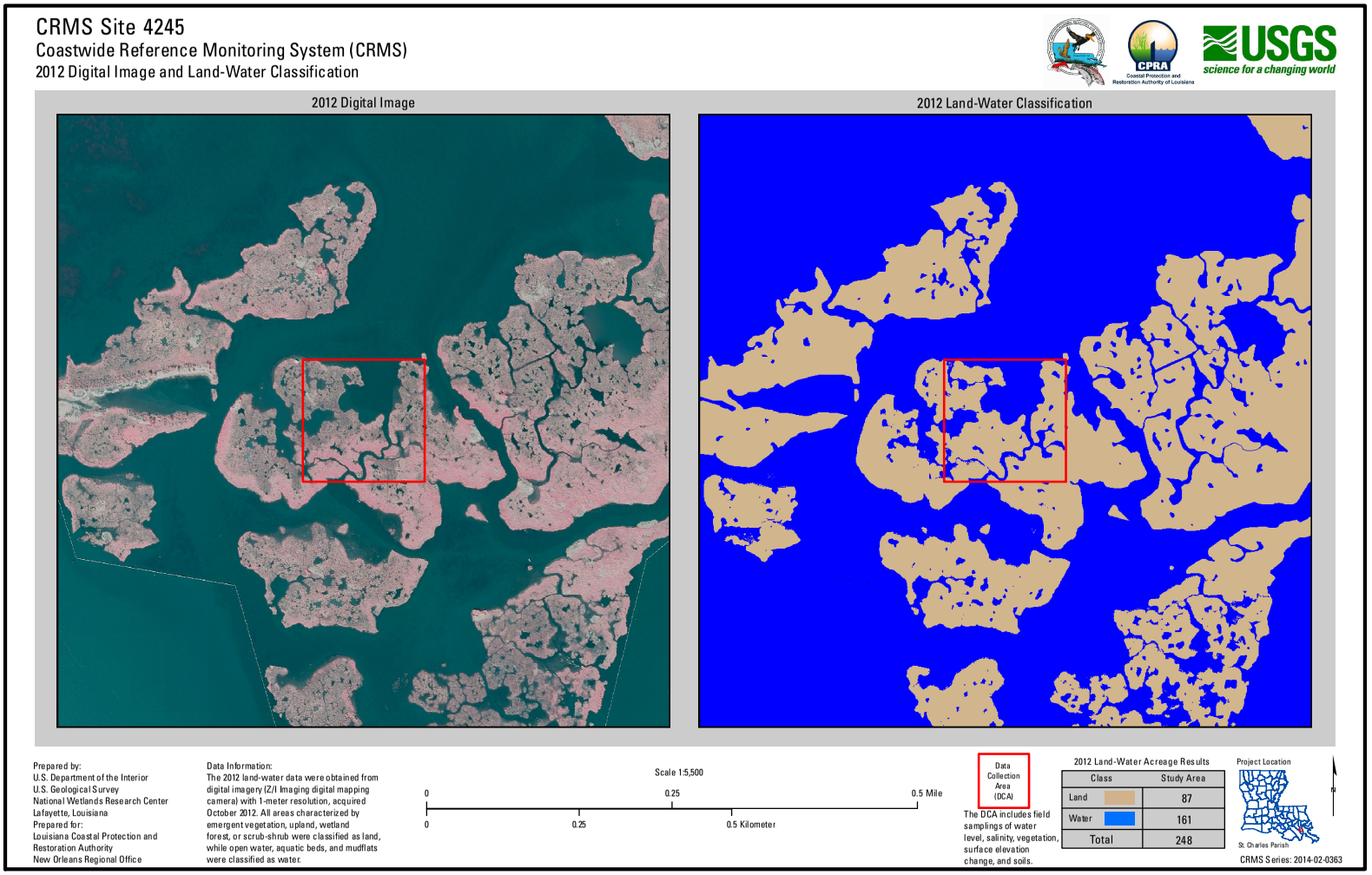

Figure 13-4 CRMS station Location Map

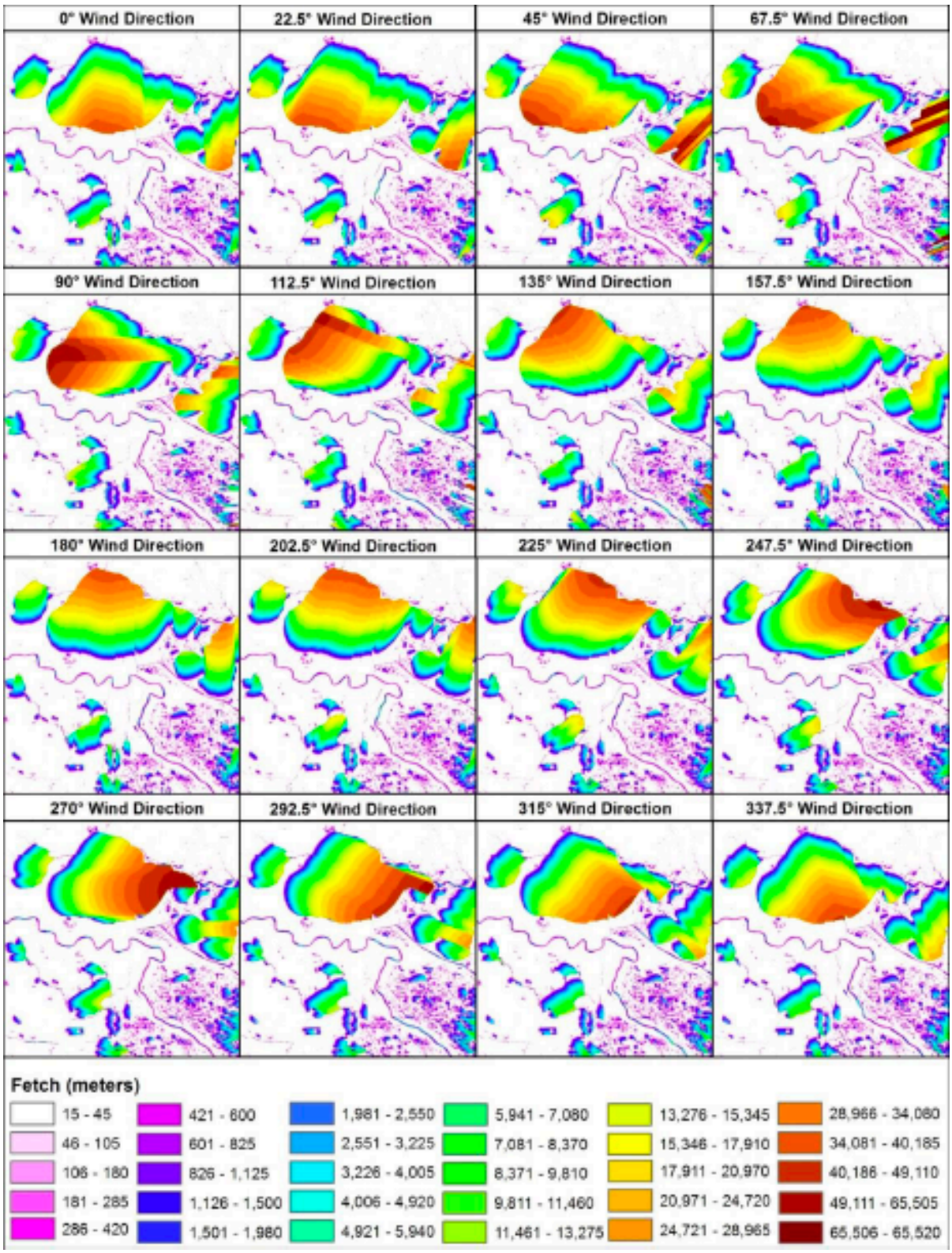

Figure 13-5 Calculated fetch for 16 wind directions for a portion of coastal Louisiana including Lake Pontchartrain (CPRA, 2017)

Summary Using Tc = 0.008 * day + 0.1562 [Pa]			
Depth [m]	Mean Concentration Clay Floc [mg/l]	Mean Concentration Silt [mg/l]	Mean Concentration Clay Particulate [mg/l]
1	5.52	1.577	0.788
2	1.588	0.454	0.227
3	0.504	0.144	0.0721

Summary Using Tc = 0.1 [Pa]			
Depth [m]	Mean Concentration Clay Floc [mg/l]	Mean Concentration Silt [mg/l]	Mean Concentration Clay Particulate [mg/l]
1	232.9	66.55	33.27
2	74.58	21.31	10.6
3	28.33	8.09	4.04

Figure 13-6 Summary of simulation for the open water cell for Fixed and for varying shear strength [Pa]. Cfcon, is the clay floc concentration [mg/l], Siltcon is the silt concentration in [mg/l], and CPcon is clay particulate concentration [mg/l].

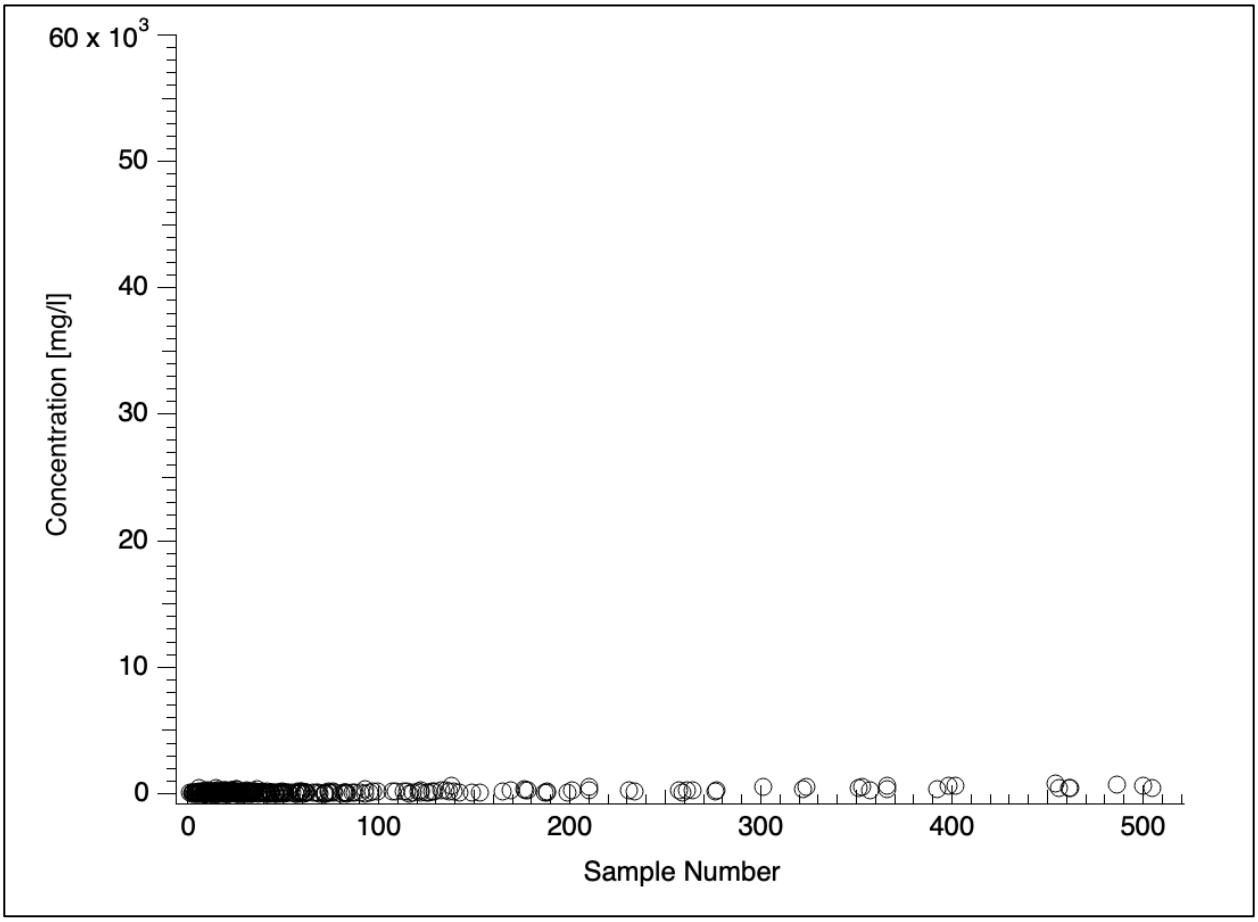

Figure 13-7 Total Suspended Solids (TSS) [mg/l] concentration measured in all Shaker experiments.

Vita

Laith Qasem Shamaileh

Born in 1992 in Amman, Jordan. Graduated in 2014 and 2017 from the University of New Orleans with a Bachelor and Master of Science in Civil Engineering. He has been working in Civil Engineering Design and Construction since 2015. He enrolled in Spring of 2017 in The Ph.D. program of Engineering and Applied science. He became a licensed professional Engineer in 2022 in the State of Louisiana and currently practicing the Engineering profession.